Planetologie

Scaling Laws for Internally Heated Mantle Convection

Inaugural-Dissertation zur Erlangung des Doktorgrades der Naturwissenschaften im Fachbereich Geowissenschaften der Mathematisch-Naturwissenschaftlichen Fakultät der Westfälischen Wilhelms-Universität Münster

vorgelegt von
Christian Hüttig
aus Gera
- 2009 -

Dekan:	Prof. Dr. H. Kerp
Erstgutachter:	Prof. Dr. T. Spohn
Zweitgutachter:	Prof. Dr. U. Hansen

Tag der mündlichen Prüfung: 10.07.2009

Tag der Promotion:

Publications

The following two publications have resulted from this thesis:

Hüttig, C. & Stemmer, K., 2008. The spiral grid: A new approach to discretize the sphere and its application to mantle convection, *Geochemistry Geophysics Geosystems,* 9**,** 13.

Hüttig, C. & Stemmer, K., 2008. Finite volume discretization for dynamic viscosities on Voronoi grids, *Physics of the Earth and Planetary Interiors,* 171**,** 137-146.

Dedication

Dedicated to my late friend and colleague Dr. Kai Stemmer

Abstract

This work presents a new method to simulate mantle convection in a spherical shell with fully spatially varying viscosities. The formulation of the governing equations is based on the finite-volume (FV) method. This has the advantage that fully irregular grids in three and two dimensions can be used and efficiently parallelized for up to 396 CPUs. While being capable of using common regular grids like the projected icosahedra and the cubed sphere grid, an irregular grid with varying lateral resolution, the spiral grid, was investigated. Basically, after a Voronoi tessellation that forms the necessary cells for the FV formulation, any set of nodal positions can be used as a base for the discretization. The model is based on the Cartesian reference frame and utilizes co-located variables. To ensure a divergence free velocity field and mass conservation, a pressure correction method called SIMPLE was applied. The discretization method is second-order accurate in space and time and time discretization is treated fully implicitly. This implies that steady-state solutions can be computed with large time-steps while strongly time-dependent convection is solved using small time-steps. The Krylov-subspace solver BiCGS with a Jacobi preconditioner is employed to solve the resulting system of equations. The discretization of the stress tensor can handle viscosity variations of up to 8 orders of magnitude from cell-to-cell and up to 45 orders of magnitude system wide. The model was validated by a comparison to analytical solutions and published results. A comparison with a commercial product also yielded satisfying results. A convergence test with successively refined grids proved the convergence towards a fixed solution.

As an application to purely internally heated mantle convection in a spherical shell, a parameter study of 88 cases is carried out to derive scaling laws for heat transport, stagnant-lid thickness and structural complexity. The aspect ratio is fixed to 0.55, similar to the value for the Earth. The applied rheology law is based on a linearized Arrhenius law, commonly known as the Frank-Kamenetskii approximation. Three convection regimes that were explored with bottom-heated convection in previous studies are also identified using purely internally heated convection. In addition, a low-degree regime is identified. This new regime exhibits long wavelength flow in the same parametric range as the sluggish regime. Furthermore, the surface is completely mobile and the transition to the stagnant-lid regime is found to be rather abrupt. To distinguish between the regimes, present and newly developed indicators are applied and validated and the transition from the mobile to the stagnant-lid regime is followed for the first time using purely internally heated convection in a spherical shell. Structural scaling laws yielding the dominant wavelength of convection based on the internal Rayleigh number are derived for the stagnant-lid regime that. Furthermore, a method capable of reconstructing the heat-flow and temperature depth-profile for this type of convection is developed.

Table of Contents

1 Introduction

Today's image of the interior dynamics of planets consists of convecting currents in their silicate mantles. The subject of the presented thesis is a better understanding of the convecting currents, i.e., the mantle convection, and the associated heat and mass transport. This phenomenon is caused by the ability to remove the internal heat efficiently by convection, which transports hot silicate material to cooler regions and vice-versa. Not only is mantle convection responsible for the thermal structure of the mantle and the thermal evolution of a planet but also for topographic features like tectonic structures and volcanoes visible on planetary surfaces. An understanding of the mantle dynamics requires among others knowledge of the inner structure and composition of the planets, for instance the ratio between the core and planetary radius. Figure 1.1 shows a sketch of the inner structure of the present Earth.

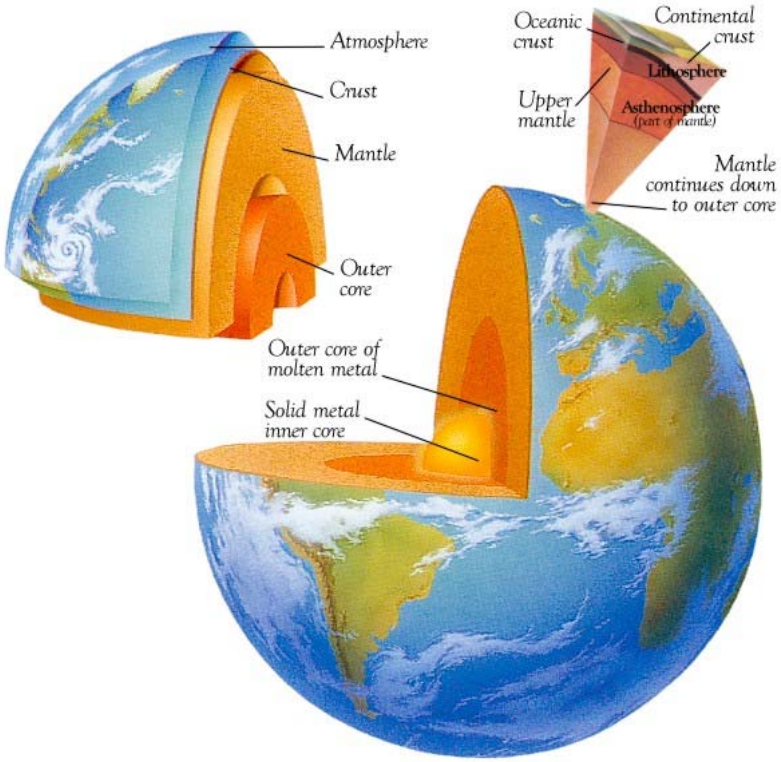

Figure 1.1: Model of the inner structure of the Earth, after Colin Rose © Dorling Kindersley

The thermal and chemical evolution of terrestrial planets is studied by many research areas such as geophysics, geology, mineralogy as well as chemistry and biology. In contrast to the Earth our understanding of other terrestrial bodies comes mostly from remote sensing and in some cases also from in situ measurements, surface samples and meteorites. Especially the surface samples from the Moon and meteorites from Mars are of immense value as they provide a wealth of information about their composition and processes on these planets like core- and crustal formation. The latter can be used to constrain models on the interior structure (e.g., Sohl and Spohn, 1997) and the thermal evolution (e.g., Schubert and Spohn, 1990, Breuer *et al.*, 1993, Spohn *et al.*, 1997, Hauck and Phillips, 2002). The thermal evolution of a planet's interior depends mostly on the dynamics of the planetary mantle through which heat is mainly transported by thermal convection. The principal mechanisms of thermal convection in the mantle have been studied since the beginning of the twentieth century (Bénard, 1900, Rayleigh, 1916, Babcock, 1930).

Convection in a silicate mantle is fundamentally different to convecting currents in the Earth's atmosphere or ocean. The silicate material of the mantle has an extremely high viscosity such that the mechanical inertia forces do not play a role anymore. A consequence of this is the immediate absence of any large-scale geological processes once the driving forces would disappear. Another distinctive behavior of mantle convection is the central influence of the complex rheology[1], the flow properties of matter. Mantle material cannot be characterized by a single value of viscosity at a fixed temperature; instead the viscosity changes due to a number of different factors. The viscosity of the mantle material varies between several orders of magnitude and depends on temperature, pressure, stress and water content (Weertman, 1970, Karato and Wu, 1993). Many studies show that the rheology has a great influence on the temporal and spatial evolution of mantle convection (e.g., Christensen, 1983, Christensen, 1984a, Christensen and Harder, 1991, Giannandrea and Christensen, 1993, Zebib, 1993, Hansen and Yuen, 1993, Ratcliff *et al.*, 1995, Weinstein, 1995, Zhu and Feng, 2005, Roberts and Zhong, 2006). The rheology for instance determines among others the different regimes of convection, i.e., plate tectonics or stagnant-lid convection.

The analysis of rheology laws is therefore unarguably of great importance and, indeed, revealed over thirty years ago that the viscosity of the silicate material in planetary mantles is mainly temperature-dependent (Tozer, 1972). Although the exact dependence on the various different influences such as e.g. pressure and composition is not well known, it is indisputable that the temperature dependence is most dominant.

The mantle of a planet is heated by various sources and mechanisms. Heat is provided by the decay of radiogenic nuclides, energy released due to the growth of an

[1] A more detailed introduction to rheology can be found at http://www.aip.org/tip/INPHFA/vol-10/iss-2/p29.html (11.02.2009)

inner core, but also by primary energy due to accretion and core formation. Temperature variations in the interior then cause density variations that further cause gravitational instabilities; thermal convection can occur as colder and denser material descends into the lower mantle and hotter and lighter material rises towards the surface. This material circulation transports heat more efficiently than by pure conduction. The interior is cooled by that process while heat sources, the decay of radioactive elements and heat from the core, tend to warm it (e.g., Schubert and Spohn, 1981, Peltier and Jarvis, 1982, Vacquier, 1998). The convective heat transport is responsible for surface stresses that can cause tectonic features like faults and compressions observed on terrestrial bodies today. An understanding of the thermal convection and evolution is therefore critical for interpreting these surface features in terms of interior processes including the dynamics of the mantle.

1.1 Fluid Dynamical Simulation of Mantle Convection

Studies on mantle dynamics are often done numerically where the convecting system is described using principle laws of hydro and fluid dynamics. The application of linear stability analysis (Chandrasekhar, 1961, Zebib *et al.*, 1980, Zebib *et al.*, 1983) revealed that in fact the interior of the Earth is convecting. The system of partial differential equations, which describe mantle convection, consists of three conservative equations, namely the conservation of energy, mass and momentum (Schubert, 1992). The numerical study of mantle convection is difficult because realistic parameters often lead to a high non-linearity that would further require computer resources that are beyond our current capability. Nevertheless, many effects of mantle convection can be explained through numerical analysis by the extraction of simple processes, leading to simplified equations through approximations and geometries. Only special cases of extremely simplified conservation equations can be described analytically, which leads to an increased interest in this topic by scientists in the field of non-linear dynamics to describe basic phenomena of turbulence (e.g., Hansen and Yuen, 1990, Grossmann and Lohse, 2000, Ahlers and Xu, 2001, Breuer *et al.*, 2004). In addition, laboratory experiments reach their limitations quickly due to extreme material properties. In spite of this, they are helpful to verify the models generated with computers (e.g., Nataf and Richter, 1982, Davaille and Jaupart, 1993, Futterer *et al.*, 2008). The main difficulty in reproducing realistic mantle flow in laboratory experiments is the complexity of the rheology that includes the effects such as pressure, stress and temperature dependencies, but also the effects of radiogenic heat sources are easier to include in a computer simulation than a laboratory experiment. Since simulations can reproduce more realistic effects, they are the main tool in understanding current mantle dynamics. Due to the ever increasing computational power in recent years, the door remains open for more complex scenarios and realistic parameters. Despite the possibility of more realistic setups, we are far from simulating all the effects of a planetary mantle. This is due not only to deficient computing power, but also to a gap in our understanding of fundamental parameters. While it is important to understand the fundamentals of the non-linear

dynamics behind the conservation equations that can lead to a completely different outcome with an extremely small change in the initial conditions, another field is currently establishing itself to simulate atoms with the help of quantum physics and supercomputers. Through this, they aim to understand the behavior of simple elements under extreme conditions that occur in the interior of planets (e.g., Belashchenko *et al.*, 2008). With simulations of this kind, rheology laws can be refined and greatly improved in accuracy.

A further important parameter apart from the rheology is the geometry. The development of three-dimensional simulations in a spherical shell completes the unknown influence of the spherical geometry on the fluid flow. The extreme increase of computing power required by the third dimension and the global representation lead first to the exploration of symmetrical states of a steady-state flow with an isoviscous fluid (Schubert and Zebib, 1980, Baumgardner, 1985). A unique property of isoviscous flow in a spherical shell is the shape of the up- and downwellings. The upwelling is shaped like a mushroom and is called a plume, while the downwelling forms sheet-like structures on the sides. Compared to flow structures in the Cartesian box, steady-state spherical geometry convection exhibits three classes of patterns. Machetel *et al.* (1986) distinguished rolls, bimodal and polygonal patterns. First physical and geophysical interpretation was done by Bercovici et al. (1989). The results led to the understanding that steady-state isoviscous flow does not maximize the heat-flow as it tends to be larger preceding a steady-state mode.

The mantle has a more complex rheology than assumed in earliest convection models in the 1980's. Numerical studies of mantle convection show that the properties of heat transport are dramatically influenced by a temperature-dependent viscosity (e.g., Christensen, 1983, Christensen, 1984a, Christensen and Harder, 1991, Tackley, 1993, Tackley, 1996a, Solomatov and Moresi, 1997). Another achievement was the first self-consistent generation of plate-tectonics driven by the mantle flow beneath (e.g., Trompert and Hansen, 1998a, Tackley, 1998, Stein *et al.*, 2004).

The lateral variation of viscosity also poses an additional difficulty regarding the numerical implication. Lateral variations are mainly due to the temperature dependency but also through the effects of a non-Newtonian rheology. The mathematical model behind the simulation is specialized to solve this kind of problem but still quickly reaches limitations. These limitations can be encountered by a refined geometry for the discretization, yielding finer discrete points to evaluate the system of equations. Another way of avoiding false results or breakdowns is to investigate numerical issues based on the limitations of a finite binary number representation on a computer. Many problems can be encountered by recognizing not only the existence of a finite discretization but also a finite accuracy of a number represented by a computer.

The inclusion of lateral variable viscosity variations also poses also a limitation to the discretization method. Usually spectral approaches are ideally suited to solve a convection simulation in a spherical environment with constant or depth dependent viscosities because there is no coupling of modes through the viscous term (e.g., Glatzmaier, 1988, Glatzmaier, 1993, Tackley *et al.*, 1993, Harder, 1998, Buske, 2006). This approach limits the viscosity variation in radial direction, but also alternative methods like finite differences, finite elements or finite volumes have difficulties encountering spherical coordinates. These usually pose a singularity at the poles; also grid spacing becomes difficult close to the poles (Ratcliff *et al.*, 1996b, Iwase, 1996). Even with different grid setups the problem remains that the representation of a number within a computer is not following the non-Euclidian spacing of spherical coordinates, so numerical differences will always yield to different numerical errors at the poles, posing the question of triggered effects even when using almost equally spaced grids based on triangulated icosahedra, which was one of the first works dealing with this problem (Baumgardner, 1985). Although other works followed (e.g., Bunge *et al.*, 1996, Yoshida *et al.*, 1999, Reese *et al.*, 1999a, Reese *et al.*, 2005), the restriction on the lateral variations were large and the overall viscosity contrast was relatively small and restricted to steady-state solutions (Tabata and Suzuki, 2001).

A first systematic analysis of weak temperature-dependent viscosity fluids in a spherical shell with a Cartesian discretization was done by Ratcliff et al. (1996b, 1996a). The mobility towards the surface decreased with an increased temperature-dependent viscosity contrast, as expected from two-dimensional Cartesian models. A fundamental outcome of this work is the rapid change of flow structure and heat-flow properties with even small viscosity variations.

Local methods in Cartesian geometry for spherical environments are therefore the preferred choice when compared to spectral approaches (e.g., Zhong, 2001, Yoshida, 2004, McNamara and Zhong, 2005b, Choblet, 2005, Yoshida and Kageyama, 2006, Roberts and Zhong, 2006, Stemmer *et al.*, 2006). Another advantage of discrete methods is the possibility of dividing the grid to efficiently distribute the problem among several computers. This combination of resources is important to counter local effects on the global scale of spherical shells. With the utilization of supercomputers, first close-to-realistic parameters can be studied.

1.2 Parameterized Convection Models

The calculation of the thermal evolution with 2-D or 3-D convection models is not only time consuming, it also requires appropriate initial conditions. Although there is ongoing research about reversing the effects of thermal convection to constrain possible initial setups (Ismail-Zadeh *et al.*, 2007), the conditions after the accretion phase of a planet are beyond our knowledge and first estimates exceed the capabilities of current day supercomputers. To be able to estimate the heat transport mechanisms under

these extreme conditions, it is of fundamental importance to obtain scaling laws. These laws stem from the behavior of a convecting fluid under conditions that we are able to study (empirical approach). After applying a well defined parametric range to the model, it is possible to find not only suitable laws that are able to describe the result, but also to extrapolate the effects to arbitrary ranges. Another advantage of these scaling laws is the immediate answer to a problem in contrast to a relative expensive and time consuming setup of numerical simulations.

This way it is possible to obtain heat transfer laws as a function of known quantities. The improved understanding of heat transport mechanisms in the planetary mantle leads to repeated changes in the preferred scaling law used to model the thermal evolution of planets. The earliest thermal evolution models for terrestrial planets used a simple parameterized law which described thermal convection for a constant viscosity fluid (Sharpe and Peltier, 1979, Schubert, 1979, Turcotte, 1979, Davies, 1980, Schubert *et al.*, 1980, McKenzie and Richter, 1981). Other attempts include the effects of a growing lithosphere in parameterized models based on constant-viscosity scaling laws (e.g., Schubert *et al.*, 1990). To characterize the stagnant, non-convecting lithosphere with isoviscous parameterization models, an isotherm describes the transition from viscous deformation to rigid response to loads applied over geologic timescales (e.g., Schubert, 1992). Such a model represents the heat transport in a planet with a single plate on top of a convecting mantle, but assumes that the lid coincides with the rheological lithosphere; the region of the planet's crust and mantle over which the flow properties of rock are insufficient to relieve stress. The weaker upper part of the mantle is assumed to be constantly recycled.

Improved scaling laws have been derived from convection models with strongly temperature-dependent viscosities with experimental and numerical studies (e.g., Richter, 1978, Richter *et al.*, 1982, Morris and Canright, 1984, Christensen, 1984a, Giannandrea and Christensen, 1993, Davaille and Jaupart, 1993, Moresi and Solomatov, 1995, Solomatov, 1995, Honda, 1996, Grasset and Parmentier, 1998, Reese *et al.*, 1999a, Reese *et al.*, 2005) . From these studies, a new convection regime could be identified using simulations with strongly temperature-dependent viscosity, i.e. the stagnant-lid regime. This regime predominantly cools the outer layers through stagnant-lid growth while the deep interior is cooled rather inefficiently. The earlier studies have mostly considered heating from below or were done in two-dimensional boxed models (e.g., Grasset and Parmentier, 1998, Sotin and Labrosse, 1999). The only studies for three-dimensional spherical shells were done for instance by Reese *et al.* (1999a, 2005), which cover only a narrow parameter range within the stagnant-lid regime and do not study the transition between the regimes or structural aspects. Since radiogenic heat sources are incorporated in the mantles of terrestrial planets, it is also necessary to study thermal convection for volumetrically heated fluid. Volumetric heating also approximates secular cooling as demonstrated by Davaille and Jaupart (1993).

1.3 Outline of this Thesis

This thesis presents an insight into the development and application of a simulation that approximates the governing equations for the viscous flow of mantle materials to finite locations in time and space. While chapter two focuses on the mathematical background, it also presents the rheology laws required to constrain the fluid flow. The generic conservation equations are presented in a non-dimensional fashion with a section describing the appropriate factors to reconstruct physical values.

The numerical techniques to discretize the equations in space and time are approached in chapter three. A new method based on the finite-volume method will be presented along with a new gridding technique. The discretization method is applicable on all Voronoi grids and is able to handle fully spatially varying viscosities with high orders of magnitude. Special attention is drawn to the discretization of the viscous element as it plays a vital role in properly describing mantle convection. The common applicability of this method is made visible by the application to various grid types, as well as to two-dimensional grids.

Chapter four concentrates on the introduction of diagnostic values to validate the model. The validation is based on analytical solutions as well as extensive comparisons with published results in this field. This is done by reproducing certain scenarios of isoviscous as well as temperature-dependent viscosity flow. Besides the comparison to published results and an analytic solution, another comparison was made by reconstructing the problem in two dimensions with commercial software, namely COMSOL.

A first application to derive scaling laws is presented in chapter five with a focus on purely internally heated convection. The derived scaling laws consist not only of heat-flow properties of convection in spherical shells, but also on structural developments that describe the complexity and time-dependency. In addition to the temperature dependence of viscosity, the influence of pressure dependency is studied as well. This is done by a parameter study of 88 cases with varied parameters such as the Rayleigh number and the above mentioned influences of temperature and pressure on viscosity. Several convection regimes have been identified and among these the stagnant-lid regime is of particular interest for terrestrial planets, i.e., the heat transport in that regime, the thickness of the lid and the mode of convection. Chapter 6 concludes this thesis.

2 Mathematical Formulations

The physical laws for mantle convection originate from the field of fluid dynamics. On geological timescales rigid rocks can properly be described as a fluid. The principle laws of conserving energy, momentum and mass are expressed with differential equations whose solutions require the definition of pressure, temperature and velocity. These elementary properties describe the dynamics of the entire system and depend on the strength of buoyancy forces, rheological parameters, internal heat sources and boundary conditions. The governing equations are described in a continuum and follow the thermo-dynamic rules (Schroeder, 2000) with approximations further explained in section 2.3.

2.1 The Rayleigh-Bénard Setup

Rayleigh-Bénard convection is the instability of a fluid layer which is restricted between two thermally conducting boundary layers, and is originally heated from below to produce a fixed temperature variation. Since liquids or rocks typically have positive thermal expansion coefficients, the hot liquid at the bottom expands and produces an unstable density gradient in the fluid layer. If the density gradient is sufficiently strong, the hot fluid will rise, causing a convective flow which results in enhanced transport of heat between the two boundaries (Bénard, 1900, Rayleigh, 1916). An extension to the original Rayleigh-Bénard configuration is a volumetric heat source or even the complete removal of the lower boundary heat source.

The state of the fluid is described for a discrete space $\vec{r}$ and time t by a velocity field $\vec{v} = \vec{v}(\vec{r}, t)$, a scalar temperature field $T = T(\vec{r}, t)$ and a scalar pressure field $p = p(\vec{r}, t)$. The density of the fluid is coupled with temperature through the thermodynamic equation of state, as explained in section 2.3. For a two-dimensional (2D) version the velocity vector contains two elements whereas in three dimensions (3D) three elements are required, totaling 5 (4 in 2D) unknowns per discrete point in space and time. The following section presents the mathematical background to derive these quantities through differential conservation equations.

2.2 The Conservation Equations

The basic set of equations that describe the fluid-mechanical properties are based on the continuity equation that, in form of a differential equation, describes the conservative transport of some quantity ϕ:

$$\frac{\partial \phi}{\partial t} + \nabla \cdot f = s, \tag{2.1}$$

where f is a function describing the flux of ϕ and s represents arbitrary sources or sinks to ϕ.

The convection of physical quantities like energy, momentum and mass are described through some form of this equation. The continuity equation has two different representations; one is the differential form as presented above, and another is the integral from. The two forms are linked together through the divergence theorem (or Gauss' theorem).

The rigid silicate rock within the mantle is subject to high mechanical stresses that lead to lattice defects within the crystalline structure. These dislocations and crystalline pollutions lead to deformations and finally to creeping motions, describable as a highly viscous fluid in a continuum. It is thus possible to describe the fluid using the Navier-Stokes equations. The following equations result from the conservation conditions for mass, momentum and energy (Schubert *et al.*, 2001, chap. 6):

$$\frac{\partial \rho}{\partial t} + \nabla \cdot (\rho\, \vec{v}) = 0 \tag{2.2}$$

$$\rho\, \mathrm{D}\, \vec{v} = -\nabla p + \nabla \cdot \underline{\tau} + \vec{f} \tag{2.3}$$

$$\rho c_P \left(\mathrm{D}\, T - \frac{\alpha T}{\rho c_P} \mathrm{D}\, p \right) = \underline{\tau} \cdot \underline{\dot{\epsilon}} + \nabla \cdot (\lambda\, \nabla T) + Q \tag{2.4}$$

Where ρ describes the density, $\vec{v}$ is the velocity vector, t time, p hydrostatic pressure , $\underline{\tau}$ the deviatoric stress tensor, $\underline{\dot{\epsilon}} = \frac{1}{2}(\nabla \vec{v} + \{\nabla \vec{v}\}^T)$ the strain rate tensor (^{T} stands for vector transpose), α the thermal expansivity, Q the volumetric heat production rate, c_P the specific heat capacity at constant pressure and λ the proportionality factor for the ratio between the heat-flow $\vec{q}$ and the temperature gradient $\nabla T = \vec{q}/-\lambda$. The energy equation (2.4) already includes the entropy relation from the second law of thermodynamics that describes the relation between entropy and temperature. The introduced material derivate D combines the derivation in time and space and is defined as

$$D = \frac{\partial}{\partial t} + \vec{v} \cdot \nabla \tag{2.5}$$

For an isotropic medium with the influence of a shear viscosity η, the following relation can be established:

$$\underline{\tau} = 2\eta \underline{\dot{\epsilon}} \tag{2.6}$$

The volumetric viscosity that represents the resistance of the body to volumetric changes is already neglected in equation (2.6).

2.3 Approximations for Mantle Convection

In order to describe geophysical fluid flow, equation (2.2)-(2.4) can be considerably simplified. Certain terms are not required because they do not influence the dynamics of the fluid at all and others are well described by a linear approximation. A main indicator for the terms that can be neglected is the Mach number (Ferziger and Perić, 1999). Other simplifications arise from the nature of the problem, e.g. the Boussinesq approximation, or the treatment of physical properties as constant, e.g. neglecting compressibility.

The Boussinesq approximation (e.g., Spiegel and Veronis, 1960, Tritton, 1988, Furbish, 1997) reduces density variations to the body forces in the momentum equation; in all other respects density is treated as a constant. The so-called standard Boussinesq approximation limits density variations to thermal expansion alone and only in gravitational direction. An extended version includes viscous heating, latent heat sources and an adiabatic temperature increase per depth that becomes of particular interest if phase changes are included in the model (e.g., Normand *et al.*, 1977). The pressure dependence of density is neglected in both versions of the approximation and the equation of state for the standard version becomes:

$$\rho = -\alpha\rho_0(T - T_0) \tag{2.7}$$

Further simplifications of the conservation equations stem from the assumption of an incompressible fluid and the negligence of inertia forces (e.g., Turcotte and Schubert, 1982). This is possible because the inertia forces are negligible small compared to the viscous friction forces. In fluid dynamics, this is also called low-Mach number flow or Stokes-flow (Ferziger and Perić, 1999), whereas the Mach number is $\ll 1$ and the Prandtl number $Pr = (c_P\mu)/k$ is assumed infinite. Nevertheless, the strong viscosity variations in a planetary mantle do not entitle to neglect shear-stress influences in the momentum equation as it is otherwise common practice for isoviscous simulations:

$$\nabla \cdot [\eta(\nabla\vec{v} + \{\nabla\vec{v}\}^T)] \not\approx \eta\,\nabla^2\vec{v} \tag{2.8}$$

With these approximations, the conservation equations for a convecting planetary mantle reduce to

$$\nabla \cdot \vec{v} = 0 \tag{2.9}$$

$$-\nabla\tilde{p} + \nabla \cdot [\eta\,(\nabla\vec{v} + \{\nabla\vec{v}\}^T)] - \rho_0\alpha(T - T_0)\vec{g} = 0 \tag{2.10}$$

$$\rho_0 c_P\,\mathrm{D}\,T = k\nabla^2 T + \rho_0 H \tag{2.11}$$

The pressure $\tilde{p} = p - \rho_0\vec{g}$ is the portion without the hydrostatic component. The gravitational field that yields the acceleration vector $\vec{g}$ within a planet stems mainly from below the mantle and can be safely approximated with the radial unity vector as

$\vec{g} = -g\overrightarrow{e_r}$. The internal heating rate H is treated as a constant and represents radiogenic heat sources.

2.4 The Dimensionless Equations

In the reduced set of conservation equations (2.9-2.11) the only remaining varying material properties are the density ρ and dynamic viscosity η. The remaining properties that influence the strength of the density variation can be combined into the dimensionless Rayleigh number Ra. With the introduction of the Rayleigh number the equations can be non-dimensionalized with reference values that simplify the equations and concentrate the physical constants into a 'driving' factor. This number is a ratio of convection supporting to convection hindering physical properties. For bottom heated convection with an inner/outer temperature difference $\Delta T = T_1 - T_0$ and a shell thickness of d it is defined as

$$Ra = \frac{\rho_0 \alpha g \Delta T d^3}{\kappa \eta_{ref}} \tag{2.12}$$

A similar expression exists for the case of internally heated convection with a volumetric heating rate H, defined as energy per time and volume:

$$Ra_H = \frac{\rho_0^2 \alpha g H d^5}{\kappa k \eta_{ref}} \tag{2.13}$$

The conservation equations change with these constants and the previous approximations to

$$\nabla' \cdot \overrightarrow{v'} = 0 \tag{2.14}$$

$$-\nabla' p' + \nabla' \cdot \left[\eta' \left(\nabla' \overrightarrow{v'} + \left\{\nabla' \overrightarrow{v'}\right\}^T\right)\right] + Ra\, T'\, \vec{e}_r = 0 \tag{2.15}$$

$$\frac{\partial T'}{\partial t'} + \vec{v}' \nabla' T' = \nabla'^2 T' + \frac{Ra_H}{Ra} \tag{2.16}$$

where all parameters with an apostrophe are non-dimensionalized scaled parameters with the following relationships to physical properties (Christensen, 1984a) and according to figure 2.1:

Space:	$\vec{x} = d \cdot \vec{x}'$	(2.17)
Time:	$t = {}^{d^2}/_{\kappa} \cdot t'$	(2.18)
Velocity:	$\vec{v} = {}^{\kappa}/_{d} \cdot \overrightarrow{v'}$	(2.19)
Pressure:	$\tilde{p} = {}^{\eta_{\mathrm{ref}}\kappa}/_{d^2} \cdot p'$	(2.20)
Temperature:	$T = \Delta T \cdot T' + T_{surface}$	(2.21)
Internal Heating rate:	$H = {}^{\lambda \Delta T}/_{d^2} \cdot H'$	(2.22)
Viscosity:	$\eta = \eta_{ref} \cdot \eta'$	(2.23)

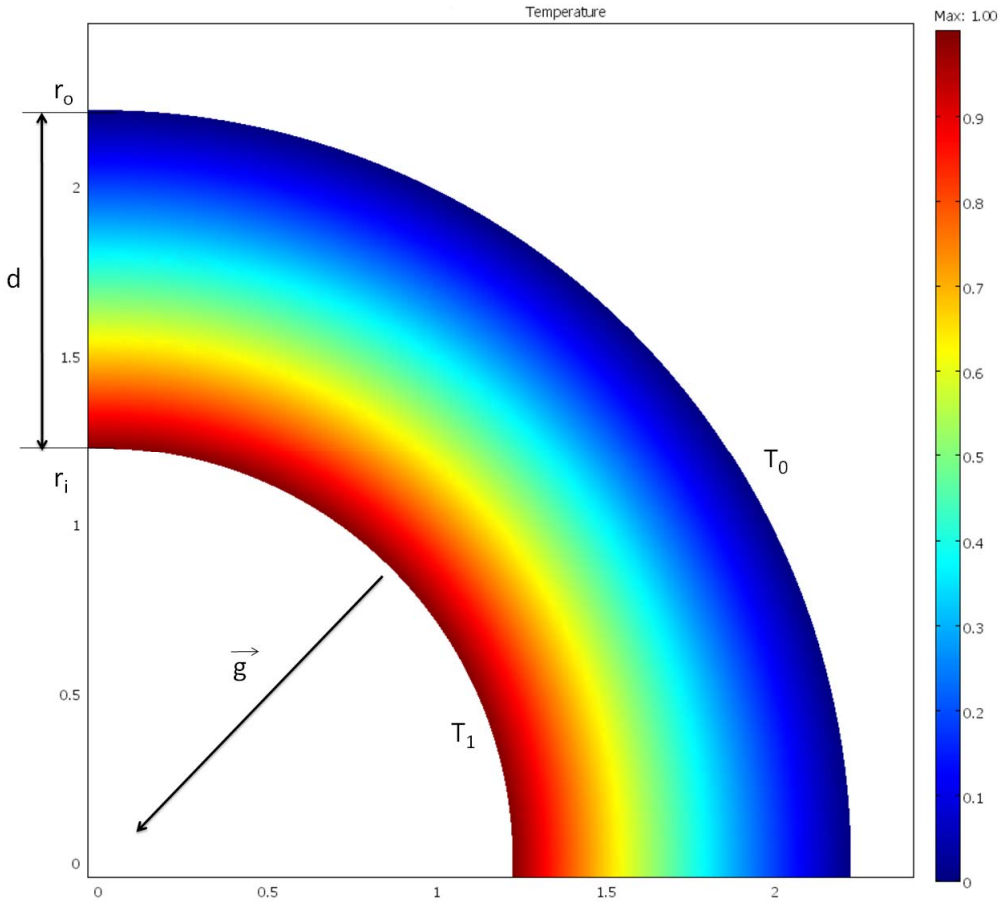

Figure 2.1. Important geometrical and boundary properties for the simulation setup. For convenience a conductive non-dimensionalized temperature gradient is shown in a 2D slice.

The thermal diffusivity is defined as $\kappa = \lambda / c_v \rho_0$. The two definitions of the Rayleigh number rely on a reference viscosity of arbitrary value, which is further discussed in the next section. The scaling parameters for temperature lead to variations between zero and one for bottom-heated convection. Note that starting from chapter 3, the ´ is neglected and all properties are non-dimensionalized for convenience. To avoid complications in back-scaling, the thickness of the spherical shell is always one, leading to the only geometry parameter, the ratio of the inner to the outer radius:

$$r_r = \frac{r_i}{r_o} \tag{2.24}$$

2.5 Rheology

Even below the melting temperature it is possible that rigid crystalline rocks in the mantle start to flow because they are exposed to high mechanical stresses and start to deform. The lattice defects of the crystalline structure of silicates start to move through the material; this is called creeping motion. In general there are two creeping mechanisms, diffusion creep and dislocation creep. The effectiveness of these mechan-

isms depends on pressure and temperature as well as on the composition of the rock itself. An active diffusion creep mechanism deforms the crystal by wandering gaps on neighboring lattice elements that, in a countermovement, is filled by an atom of another neighboring element. The probability of creating gaps depends on the stresses that act on the crystal structure. If these stresses are not equal on all sides, the concentration of gaps starts to vary, which is compensated with lattice diffusion. This diffusion creep is thermally activated and can be described by an Arrhenius term with a diffusion coefficient $\widetilde{D}$:

$$\widetilde{D} = D_0 \exp\left(-\frac{E^* + pV^*}{RT}\right) \tag{2.25}$$

In the above equation, E^* acts as the activation energy per Mol, which contains the required energy to create gaps as well as the necessary potential barrier between a gap and the occupied lattice element. The activation volume per Mol V^* considers an increased energy barrier to neighbor elements due to pressure. The exponential form follows directly from the Boltzmann distribution that determines the fraction of atoms with a distinct energy at temperature T. D_0 contains the jump frequency and R is the gas constant.

Dislocation creep is in some cases more efficient than diffusion creep if instead of point-defects dislocation defects (line defects) start to move through the crystal. Dislocations can glide under the influence of shear stresses through various lattice levels that require only minimal energy to reorder the atoms within a crystal. This is possible with lattice defects that diffuse to the dislocation - a controlling process for the rate of the dislocation creep. It is described with the above Arrhenius law (Karato, 1981, Karato and Wu, 1993). The deformability of the material and therefore its viscosity depends on the diffusion coefficient $\widetilde{D}$. Experiments and theory yield a common relation between stresses and rate of deformation, for which both creeping mechanisms are valid (Karato and Wu, 1993, Schubert *et al.*, 2001):

$$\underline{\dot{\epsilon}} = \frac{1}{2\eta}\underline{\tau} = A\left(\frac{\tau_{II}}{\mu}\right)^{n-1}\left(\frac{b}{\tilde{d}}\right)^{m}\exp\left(-\frac{E^* + pV^*}{RT}\right)\underline{\tau} \tag{2.26}$$

Here, A represents a normalization factor, τ_{II} the square root of the second invariant of the stress tensor, μ is the shear modulus, $\tilde{d}$ is the grain size and b the absolute value of the Burges vector that describes the relative atom motion for a defect through the crystal. The non-dimensional values of $\tilde{n}$ and $\widetilde{m}$ determine the active creeping mechanism. Typical values are $\tilde{n} = 1$ with $\widetilde{m} = 2.5$ for diffusion creep and $\tilde{n} = 3$ with $\widetilde{m} = 0$ for dislocation creep. In case of active diffusion creep the viscosity is therefore independent of stress.

For this study, only diffusion creep (Newtonian viscosity) is considered which can be expressed in a normalized form as

$$\eta = \exp\left(\frac{E' + V'(r_o' - r')}{T' + T_s'} - \frac{E' + V'(r_o' - r_i')}{T_{ref} + T_s'}\right) \tag{2.27}$$

using the following normalizations (Roberts and Zhong, 2006):

$$E' = \frac{E^*}{R\Delta T} \tag{2.28}$$

$$V' = \frac{\rho_0 g R_o V^*}{R\Delta T} \tag{2.29}$$

$$T_S' = \frac{T_{surface}}{\Delta T} \tag{2.30}$$

The reference temperature T_{ref} determines the reference viscosity for the Rayleigh number $\eta_{ref} = \eta(T_{ref})$. The pressure-dependent term is approximated by a depth dependent term following the normalized radius. Because the viscosity can also be depth dependent, a term for the reference depth is for simplicity fixed to the inner radius ($r_{ref}' = r_i'$). The reference temperature therefore determines about which values the Rayleigh number, i.e. the driving term varies.

3 Numerical and Technical Realization

Over the last three decades, local discretization methods like finite-element (FE), finite-volume (FV) and finite-difference (FD) methods have firmly established themselves as the approach for computational fluid-flow problems in geophysics, especially with regard to thermal convection problems involving spatially varying viscosities in two (e.g., Parmentier, 1978, Christensen, 1984a, Hansen and Yuen, 1993, Solomatov and Moresi, 2000a) and three dimensions (e.g., Ogawa *et al.*, 1991, Christensen and Harder, 1991, Ogawa, 1995, Trompert and Hansen, 1998a, Tackley, 1998, Stein *et al.*, 2004) as well as in spherical shells (e.g., Tabata and Suzuki, 2000, Zhong *et al.*, 2000b, Yoshida and Kageyama, 2004, McNamara and Zhong, 2005a, Choblet, 2005, Stemmer *et al.*, 2006). The advantages of irregular grids like arbitrary refinements and resolution choices were left outside because of more complicated discretization techniques and computational requirements. Nevertheless, these advantages become especially interesting in cases with complex geometries like spheres in three dimensions (3D) or disks in two dimensions (2D), which occur regularly in geophysics. This section demonstrates a technique to utilize the FV method on irregular grids in 3D with a focus on the spatial derivate of the stress tensor, required for the implementation of dynamic viscosities, which is of primary interest in the field of mantle convection modeling (e.g., Stemmer *et al.*, 2006).

Another focus lies on a new technique to generate a spherical grid with unique properties, the spiral grid. Because no grid is orthogonal all over the spherical surface and at the same time free of coordinate singularities and grid convergence, the spherical surface is usually split up into sub-regions. To distribute points uniformly on a sphere, most grids are based on triangulated platonic solids, which radially project from the center. Complex grids based on subdivisions of platonic solids like the icosahedra grid (Baumgardner, 1985), the rhomboid grid (Zhong *et al.*, 2000b), the Yin-Yang grid (Kageyama and Sato, 2004, Yoshida and Kageyama, 2004), the cubed-sphere grid (Choblet, 2005) and the smoothed cubed-sphere grid (Stemmer *et al.*, 2006) prevail for modeling mantle convection in a spherical shell. These grids have axisymmetric alignments that simplify the discretization schemes in the form of algebraic descriptions and make possible the use of multigrid methods, but also cause some restrictions. Firstly, the user can only choose between fixed resolution step sizes that increase the total number of grid points in preset steps. For example, increasing the resolution by the next possible step in an icosahedral refinement results in about eight times more grid points (Baumgardner, 1985). Secondly the volume and neighbor distance of a cell depends on its radius, i.e. on the inner surface of the spherical shell the grid points are arranged more densely than on the outer surface.

The approach presented in this chapter is based on the proposed dual-grid approach in (Ferziger and Perić, 1999, chap. 8). It utilizes a Voronoi grid as cellular discrete basis for the domain and its dual, the Delaunay triangulation to setup shape functions for an arbitrary linear interpolation mechanism (Agouzal *et al.*, 1995, Baranger *et al.*, 1996). The triangulation in combination with a Voronoi discretization is able to fulfill all requirements for irregular grids in a FV scheme. In recent years, computational and storage improvements have opened the door to embrace the use of complex grids with their advantages and increased computational requirements.

3.1 Voronoi-Based Grids on the Sphere

The term Voronoi-grid refers to grids that have so-called Voronoi properties, named after the Russian scientist Georgy Voronoy. In general, a grid for computational aspects refers to discrete positions in space where the variables of interest are solved for; the space between those locations is approximated by a certain order that reflects the mathematical description on how to calculate these points. The grid can either be fixed in space ("Eularian") or moving along the velocity field ("Lagrangian"). Both definitions have their advantages and disadvantages (e.g., Ferziger and Perić, 1999, chap. 1) that are not further discussed here. It is always possible to construct the Voronoi diagram of a certain set of points / locations to divide the domain of interest into cell-like structures, sometimes called Thiessen-polygons. The in this way generated Voronoi cells have the unique property that any location within a certain cell is closest to its generator point, which is the grid point (see 3.1.1.3).

3.1.1 The Spiral Grid

The spiral grid can avoid these disadvantages using an almost uniform distribution of grid points from the Archimedean spiral equation, which is modified to create a spherical shell. These Cartesian functions lead to extremely dense points at the poles in comparison to the equator of the sphere when advancing them over an angular variable. Obtaining an equidistant distribution over a constant arc length requires the inversion of elliptic integrals. The distribution of the spherical spiral over increasing radii results in a shell-based point cloud with an average distance between neighbors of a desired resolution.

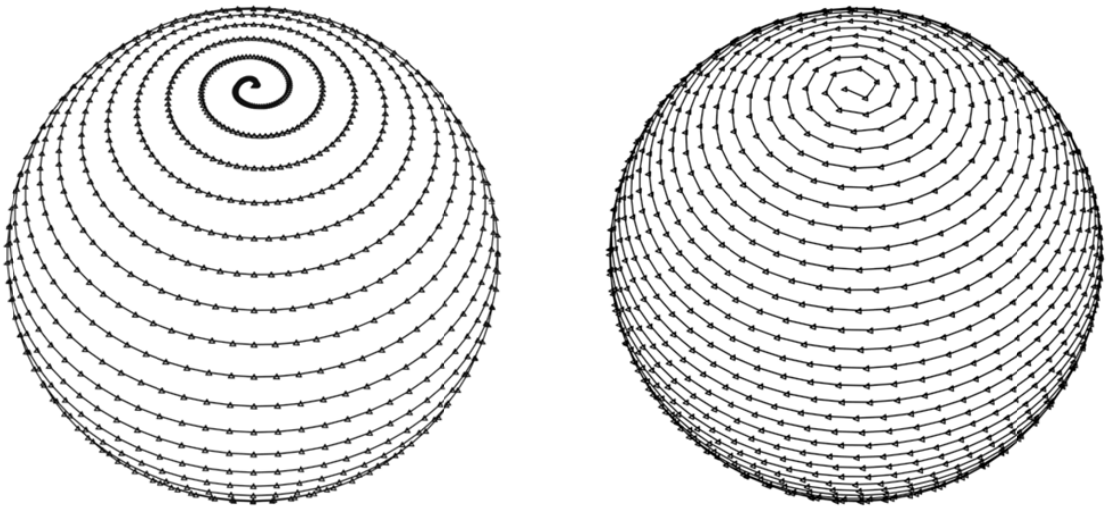

Figure 3.1. The spherical spiral with a constant angular increase (left) and its equidistant version (right) from a preset point distance.

An advantage of this method is that the user may freely select a resolution or amount of grid points. In comparison to projected grids, this method results in less grid points at equal outer shell resolution and therefore lower computational costs, as explained in section 2. After assembling the Voronoi diagram of all points (further explained in 3.1.1.3), convex natural-neighbor polyhedra occur around each point. These cells offer certain beneficial properties, for instance, the almost constant volume of the grid cells compared to the increase in volume of cells with increasing radius within a projected grid.

The geometrical properties of a Voronoi grid favor a finite-volume discretization of the required equations and in combination with the spiral grid provide among the previously discussed properties a single array alignment for one shell along the spiral path. This housekeeping method makes it easy to identify adjacent cells. Varying depth-dependent resolutions gives the user the choice to refine certain areas of interest, as well as the chance to have a very small inner radius to outer radius ratio while maintaining a laterally balanced resolution for optimal parallelization as explained in section (3.6).

3.1.1.1 Generator Point Equations

Layers of spirals with a constantly or variably increasing radius form a three-dimensional spherical shell from a desired inner to outer radius. These spirals are discretized to point shells, which act as generator points for the Voronoi diagram (VD). An equidistant discretization along the Archimedean spiral guarantees a nearly uniform distribution. The VD provides cells as arbitrary convex polyhedra that through its unique properties suit a finite-volume (FV) method.

The basic equation for the two-dimensional Archimedean spiral in polar coordinates is given by

$$r = f(\varphi) = \tilde{a} \cdot \varphi \tag{3.1}$$

where r is the radius and a the increment multiplier of the angle φ. For a two-dimensional Cartesian representation, the two parametric equations for each coordinate evolving over an angular variable, $\tilde{\alpha}$, are given by

$$\begin{aligned} x &= f(\tilde{\alpha}) = \tilde{\alpha} \cdot \sin\tilde{\alpha} \\ y &= f(\tilde{\alpha}) = \tilde{\alpha} \cdot \cos\tilde{\alpha} \end{aligned} \tag{3.2}$$

Finally, the spiral mapped over a sphere in three-dimensional Cartesian coordinates, evolving from zero to $\tilde{\alpha}_{max}$, which is from the north pole to the south pole, is provided by

$$\begin{aligned} x &= f(\tilde{\alpha}) = r \cdot \cos(\tilde{\alpha}) \cdot \cos\left(-\frac{\pi}{2} + \frac{\tilde{\alpha}}{\tilde{\alpha}_{max}} \cdot \pi\right) \\ y &= f(\tilde{\alpha}) = r \cdot \sin(\tilde{\alpha}) \cdot \cos\left(-\frac{\pi}{2} + \frac{\tilde{\alpha}}{\tilde{\alpha}_{max}} \cdot \pi\right) \\ z &= f(\tilde{\alpha}) = -r \cdot \sin\left(-\frac{\pi}{2} + \frac{\tilde{\alpha}}{\tilde{\alpha}_{max}} \cdot \pi\right) \end{aligned} \tag{3.3}$$

where $2\,\tilde{\alpha}_{max} / \pi$ determines the amount of complete revolutions of the spiral on the sphere with a radius of r.

The intention behind this discretization method is to distribute points along the spiral path with a constant user-chosen distance, which results in a uniform cell resolution on the spherical shell. The equation for the arc length from (3.1) and (3.2) is

$$s = \frac{1}{2}\tilde{a}\left(\varphi\sqrt{1+\varphi^2} + \log\left[\varphi\sqrt{1+\varphi^2}\right]\right) \tag{3.4}$$

which cannot be solved for φ analytically. The general equation for the arc length in three-dimensional Cartesian coordinates is given as:

$$s = \int \sqrt{\partial_x\tilde{\alpha}^2 + \partial_y\tilde{\alpha}^2 + \partial_z\tilde{\alpha}^2}\, d\tilde{\alpha} \tag{3.5}$$

The following equation evolves by using (3.3) with (3.5):

$$s = r\,\mathrm{E}\left[\frac{\pi\tilde{\alpha}}{\tilde{\alpha}_{max}}, -\frac{\tilde{\alpha}_{max}^2}{\pi^2}\right] \tag{3.6}$$

This equation includes the second incomplete elliptic integral $\mathrm{E}[\tilde{\alpha}, \acute{m}]$, which is defined as

$$\mathrm{E}[\tilde{\alpha}, \acute{m}] = \int_0^{\tilde{\alpha}} \sqrt{1 - \acute{m} \sin^2 \tilde{\theta}}\ d\tilde{\theta}\,, \tag{3.7}$$

where $\acute{m}$ is the elliptic modulus. By increasing $\tilde{\alpha}$ with a constant value, the points become very dense around the poles and sparse on the equator, as illustrated in figure 3.1 left. To have a constant predefined distance along the spiral path, an inversion of the arc distance equation (3.6) for $\tilde{\alpha}$ is necessary. This inversion computes the location of the points for an equidistant distribution.

By applying equation (3.6) to find the angular values of $\tilde{\alpha}$ for the original three-dimensional Cartesian equation (3.3) of the spiral, an equidistant distribution of points along the spiral path appears on the sphere as shown in figure 3.1 right. A numerical method proposed by Carlson (2002) reduces the computational costs to inverse the second incomplete elliptic integral used in (3.6).

Since $\tilde{\alpha}_{max}$ determines the revolutions of the spiral from the top to the bottom, it must be chosen properly to guarantee an equidistant distribution that fits the requested resolution. With a defined resolution R and layer radius r_l, $\tilde{\alpha}_{max}$ is given by

$$\tilde{\alpha}_{max} = \left(\frac{3\pi^2 r_l}{2\ R}\right) \tag{3.8}$$

3.1.1.2 Radial Extension

To create the generator points necessary for triangulation or Voronoi tessellation, the method described in the previous section is repeated for several radii between a user-chosen inner and outer radius. This results in the layering of concentric spiral spheres. The equation to return the number of layers i_l required for a certain global resolution is

$$i_l = \frac{3(r_o - r_i)}{4R} + 2 \tag{3.9}$$

The number of generator points that result between two given radii and a resolution R is given by

$$n_{total} = \sum_{i=0}^{i_l} \frac{1}{R} \mathrm{E}\left[\pi, \frac{6\pi\ r_i}{4R} + 2\pi\ i\right] \tag{3.10}$$

The spherical shell consists of two additional boundary shells within the inner and outside the outer radius. To produce smooth inner and outer walls these points are exactly above (below) the last outer (inner) shell points. Those two boundary layers produce open polyhedra on the outside and core-connecting polyhedra on the inside. The boundary walls can be turned into spherical triangles for increased precision on

low-resolution grids to improve accuracy and therefore will remain as the only cells with partial curved elements.

By "overturning" the spiral equations on every second layer, where $\tilde{\alpha}$ evolves from $\tilde{\alpha}_{max}$ to $2\tilde{\alpha}_{max}$, the standard deviation of the neighbor point distances can be reduced. The spiral would evolve from the south-pole to the north-pole in the opposite revolution. Starting $\tilde{\alpha}$ in equation (3.3) at $R/2$ instead of zero, leads further to a reduction of the cell volume fluctuations at the poles (see statistics section 3.1.1.5, closeup of figure 3.4).

3.1.1.3 Cell Properties

The point distribution from these equations now allows a triangulation and Voronoi tessellation. After applying fast Voronoi algorithms like after (Barber *et al.*, 1996), cells as in figure 3.2 emerge with typical Voronoi properties such as:

- every wall distinguishes two generator points as natural neighbors
- every wall lies perpendicular to a line between two natural neighbors
- every wall is placed exactly between two natural neighbors
- every cell is convex
- the cell is the region in which its generator point is closest

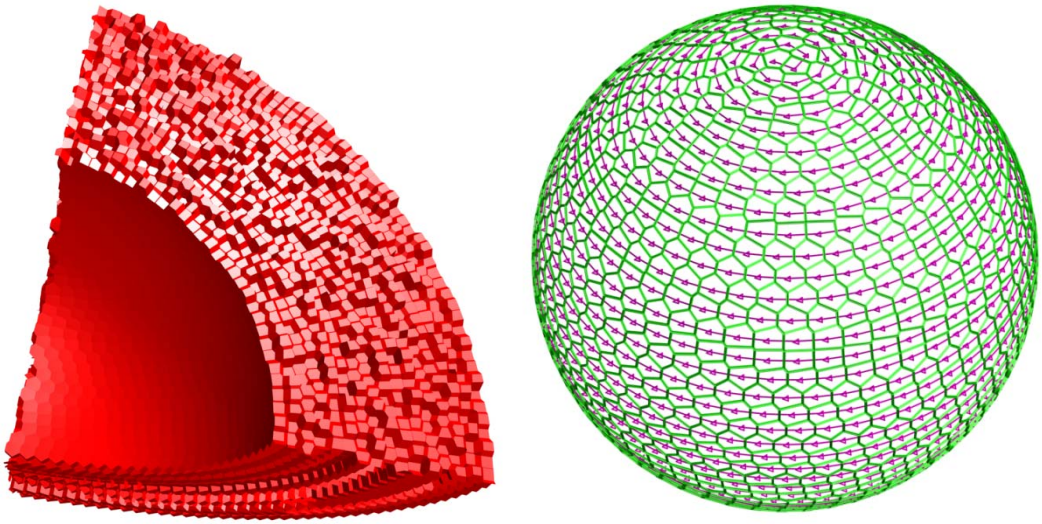

Figure 3.2. Left: a cut through the positive Cartesian domain of the spiral grid with an inner radius of one, an outer radius of two and a resolution of 0.1, excluding the boundary shells; the complete grid consists of 62,529 cells. Right: a spherical Voronoi Diagram for one shell of spiral generator points.

The process to calculate the spiral generator points takes approx. 0.05 % of the time to compute the whole grid; the major time takes the Voronoi tessellation.

To obtain some important properties such as the center of mass, volume and the surface of the cell walls, which appear in the discretization of differential equations and definition of the operators, some care was taken to optimize the surface and volume integrals to receive accurate and quick results.

The tetrahedron is the simplest object that can occupy space in three dimensions. Any simplex with n+1 coordinates within n dimensions is capable of this. The special properties of these simplexes remain within arbitrary dimensions: their center of mass is situated within the arithmetic mean of all coordinates and their n-dimensional volume can be computed by

$$V = \frac{1}{n!}\det\begin{bmatrix} x_{1,1} & \cdots & x_{1,n} & 1 \\ \vdots & \ddots & \vdots & \vdots \\ x_{n+1,1} & \cdots & x_{n+1,n} & 1 \end{bmatrix} \tag{3.11}$$

The n+1 coordinates for an n-dimensional tetrahedron lie in the vertical direction of the matrix of equation (3.11). The algorithm to compute the centroid of a convex polyhedron uses these properties. It consists of the following steps:

- computing the arithmetic mean of all vertices, which results in a point guaranteed to be within the polyhedron
- projecting rays from this preliminary center to the faces of the polyhedron, resulting in possible deconstruction into tetrahedra
- computing the center of mass (COM) and volume of each tetrahedron
- weighting all COM by their volume to obtain the true COM of the polyhedron
- adding all tetrahedral volumes to obtain the polyhedron volume

The areas of the cell walls were computed using a method described by Sunday (2002), with an advancement over the textbook equation for the area of an n-vertex two-dimensional polygon, which normally uses 2n+1 multiplications and 2n-1 additions. Sunday (2002) improves the equation so that it takes n+1 multiplications and 2n-1 additions. A similar equation is derived for a three-dimensional planar polygon where, given the unit normal, the textbook equation cost of 6n+4 multiplications and 4n+1 additions is reduced to n+2 multiplications and 2n-1 additions.

3.1.1.4 Centroidal Shift

A centroidal Voronoi diagram (CVD) is a specific Voronoi diagram (VD), where the associated generator points coincide with their centroids. The centroid is the center of mass of the corresponding Voronoi cell. Such tessellations are useful in data compression, optimal quadrature rules, optimal representation and quantization, finite difference schemes, optimal distribution of resources, cellular biology and the territori-

al behavior of animals, among other contexts (e.g., Du *et al.*, 1999, Du and Gunzburger, 2002, Alliez *et al.*, 2005). Ju *et al.* (2002) describes in detail some of these applications and algorithms.

A common way to define finite difference schemes on irregular meshes for the approximate solution of partial differential equations is based on Voronoi tessellation and its dual grid, the Delaunay triangulation. In many cases, using centroidal Voronoi tessellations guarantee a second-order truncation error for the different equations compared to a first-order truncation error for other Voronoi tessellations. Similar results are known for co-volume methods based on the dual Voronoi-Delaunay tessellations. Lloyd's method provides one of two basic algorithms to iterate towards a CVD (MacQueen, 1967, Lloyd, 1982). For an initial set of n points the procedure is as follows:

1. Determine the VD corresponding to the n generator points.
2. Determine the centroids with respect to a given density function of the n Voronoi cells.
3. Set the *n* generator points to their corresponding n centroids.
4. Repeat steps one to three until satisfactory convergence is achieved.

	Gridtype	Minima	Mean	Maxima	σ	Skew
Distance PDF	VD	0.0733	0.0999	0.1435	0.01476	0.104
Distance PDF	CVD	0.0716	0.0977	0.1383	0.01148	0.779
Neighbor PDF	VD	10	14.513	20	0.93145	0.381
Neighbor PDF	CVD	9	14.126	19	0.85666	0.156
Volume PDF	VD	5.0747e-4	5.6241e-4	6.140e-4	6.70e-6	0.111
Volume PDF	CVD	4.4102e-4	5.6271e-4	6.581e-4	1.89e-5	-0.436

Table 3.1. Statistical values of the spiral grid with an inner radius of one, an outer radius of two and a resolution of 0.1 according to the probability density functions (PDF) of Figure 3.6. The complete grid consists of 62,529 cells. Distance describes the Euclidian distance between neighbors, Neighbor refers to the amount of neighbors per cell and volume specifies the cell volume.

This method involves finding the centroids of the polyhedron. The centroid becomes the point where the partial differential equations are calculated. Note that the generator point from the spiral is not necessarily the centroid of the Voronoi cell. The spiral spherical shell shows an advantage over other distribution methods because the centroid is already close to the generator point, which results in lesser iterations with the Lloyd method.

3.1.1.5 Statistical Analysis

Statistical analyses of the original spiral grid and shifted spiral grid with the centroidal Voronoi diagram (CVD) are applied to highlight the advantages of this grid structure. An inner radius of one and outer radius of two were taken to analyze the grid

at a resolution of 0.1. Note that the stop criterion for the Lloyd iterations is a mean distance from the generator points to the true centroid of $5 \cdot 10^{-6}$, which results in approximately twelve iterations (as explained in the previous section).

The centroidal shift demonstrates several advantages and disadvantages in the spiral spherical shell. The shift reduces the amount of Voronoi vertices and faces by about three percent, and yields a better standard deviation of the neighbor distances proven by figure 3.4 and table 3.1. Figure 3.3 illustrates the volume fluctuations within the cells along the spiral path before and after the centroidal shift and shows the effect of the increased standard deviation of the volumes after the shift. The peaks from the original distribution at the poles vanish.

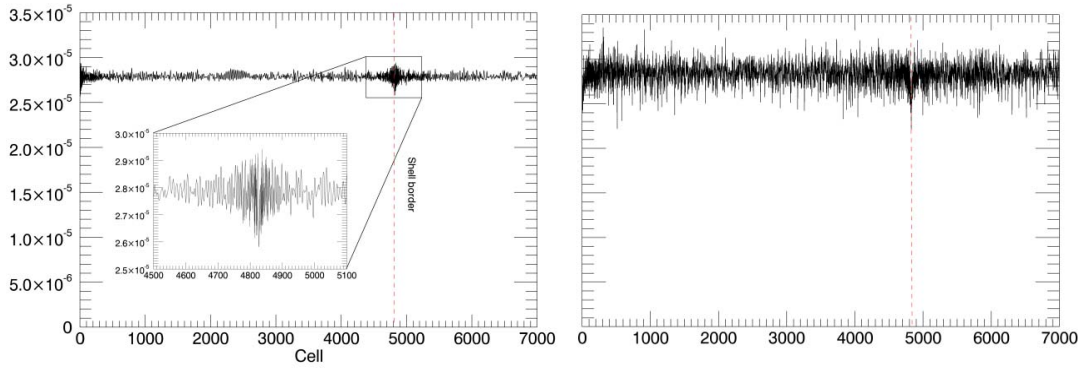

Figure 3.3 Cell volumes along the spiral path from the original VD distribution (left) and from the CVD shifted distribution (right). The straight line marks the transition to the next shell at the pole.

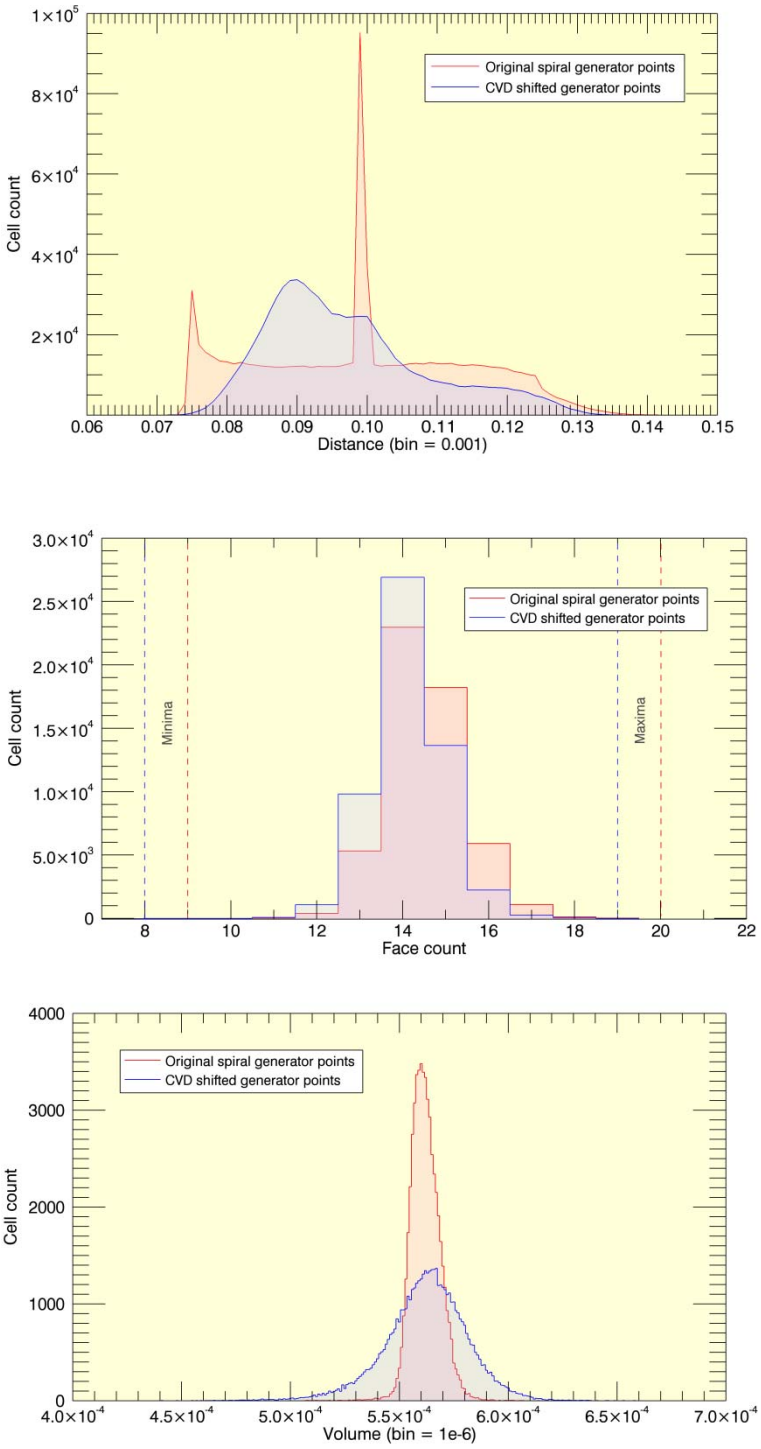

Figure 3.4. Statistical analysis of the original spiral grid (VD, red) and the centroidal Voronoi diagram (CVD, blue) generated by shifting of the original grid points. a) PDF of the natural-neighbor distances. b) PDF of the number of faces per cell. c) PDF of the cell volume.

In figure 3.4a probability density functions (PDF) are plotted for the distances of adjacent cells, cell volumes and number of cell faces for the VD and CVD. With respect to the distance histogram, the peak in the original distribution is caused by the exact

calculated distance along the spiral path. At least two neighbors of every cell have the pre-set resolution as distance to each other since there is one predecessor and one successor on the spiral path. This applies for all cells except the first and the last in one spiral. Note that the peak is slightly off the desired resolution since it is calculated along a curved spiral path, which results in a slightly smaller spatial distance. The CVD version shows a reduced standard deviation but a slight left shift and higher skew. The projected first and last boundary shell causes an irregularity in the distribution and first appears as the mentioned shift during the Lloyd iterations. These shells are projected to create a smooth boundary. Purely projected grids would have a much less pronounced peak because the distances of adjacent cells generally increase with increasing radius.

The face count PDF presented in figure 3.4b displays a major advantage of a CVD. The centroidal shift yields a reduction of Voronoi-faces and therefore vertices. The face count is equal to the amount of neighbors per cell and therefore matrix entries, so it reduces necessary calculations within the numerical discretization as well as resources and housekeeping information.

The peak for the volume histogram in figure 3.4c is less pronounced for the CVD compared to the VD, but the absolute volume differences are relatively small because the CVD grid is shifted to get centroidal characteristics. This is the only disadvantage of a CVD; the centroidal shift does not tend to equalize cells to their volume. Generator points can be positioned so that the resulting VD would be a CVD but with cells of different volume.

3.1.2 Projected Grids

Another grid type that obeys the Voronoi properties naturally are radially projected grids. These grids have the same amount of grid points in each shell, leading to spatially dense structures at the inner radius and coarse and distorted cells at the outer radius. They usually originate from triangulated platonic solids such as the cube (Choblet, 2005, Stemmer *et al.*, 2006) or the icosahedron (Baumgardner, 1985) as illustrated in figure 3.5.

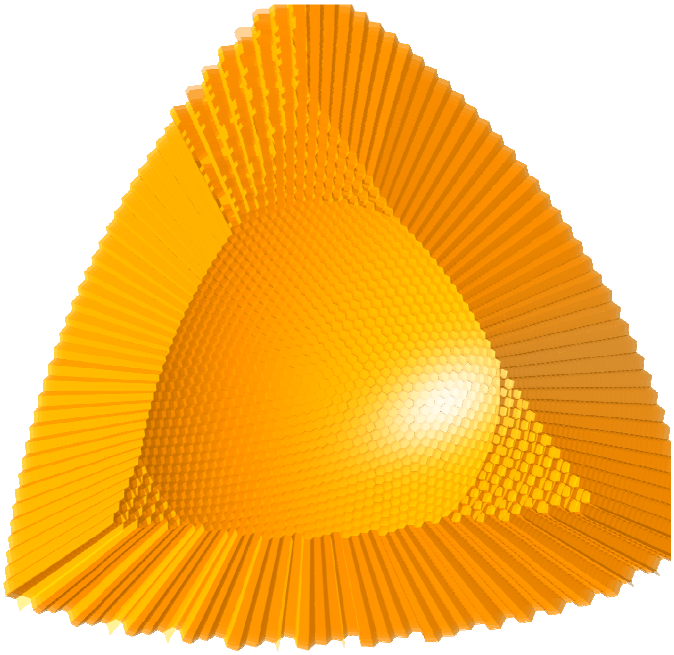

Figure 3.5. A projected icosahedra grid, originating from simple triangular subdivisions (five iterations), projected radially to produce shells with an equal amount of generator points for the final Voronoi tessellation.

A major advantage of these setups is the algebraically describable geometry that allows the discretization scheme to incorporate the geometry and therefore saves memory. Nevertheless the numerical operations involved to solve the governing equations are increased in this setup. Another advantage lies in the previously described radial resolution difference that is advantageous for bottom heated convection because the temperature and therefore the vigor of convection are highest close to the inner boundary. The fact that all points of a single shell lie on a sphere makes it possible to use spherical coordinates to discretize the equations in space, which is not necessarily advantageous.

A further possibility is a mid-way of projected grids that do not incorporate the algebraic descriptiveness into the discretization but store the weights into a sparse matrix. Recent development in this field marks the Yin-Yang grid (Kageyama and Sato, 2004) or a projected spiral grid.

3.2 Discretization

Most of the published models for mantle convection that include locally varying viscosities implement the necessary spatial derivative of the stress tensor with finite-elements (Zhong *et al.*, 2000b) or utilize grid-regularities (e.g., Yoshida and Ogawa, 2004, Yoshida and Kageyama, 2004, Choblet, 2005). Staggered approaches where velocity and scalar fields do not coincide at the same locations were preferred because of their straightforward implementation and elimination of numerical oscillations (e.g.,

Perić *et al.*, 1988). Advantages of the FVM are the direct connection to the underlying physical problem and the conservative nature of its scheme that enables a direct implementation of boundary conditions similar to the finite-difference method. A disadvantage arises in irregular grids. The effort to discretize the desired equations with the FV method increases once the walls between the computational cells become tilted and spatial derivates besides the normal direction are required. Ferziger and Perić (1999) describe in chapter 8 an effective approach to acquire a correct solution for tilted walls. The only remaining problem within an irregular grid was the implementation of a spatial derivative of the relatively complex stress tensor that is required for locally varying viscosities in geophysical flow problems.

3.2.1 Numerical Basis

The domain of interest in FV and FE methods is defined as control volumes, which are integrated over the governing partial differential equations of interest. Moving further to fluid mechanics, the basis of the FVM is therefore the integral form of the conservation equations. The solution domain is divided into a finite number of control volumes (CVs), and the conservation equations are applied to each CV. At the centroid of each CV lies a computational node at which the variables are evaluated. Interpolation is used to express variable values at the CV surface in terms of the nodal (CV-center) values. Surface and volume integrals are approximated using suitable quadrature formulae. As a result, one obtains an algebraic equation for each CV, in which a possible varying number of neighbor nodal values appears (Fletcher, 1991).

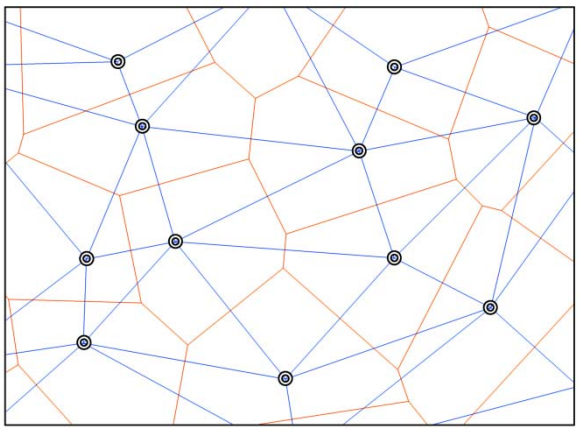

Figure 3.6. The Voronoi diagram in red and the according Delaunay triangulation in blue for a random set of generator points.

The FVM can accommodate any type of grid, so it is suitable for regular and irregular grids. Most regular grids are Voronoi grids by nature, which means that within a CV every point is closer to its associated nodal location than to any other. This nodal position serves as generator point for a Voronoi region and results in a CV, as demonstrated in figure 3.6. The resulting cell structure offers interesting properties: the face dividing two neighboring CVs lies always midway and perpendicular between them, which is one requirement for the FV method. The amount of faces is the direct count of

neighbors for a specific CV and is always minimal (Okabe *et al.*, 2000). This neighbor count is directly associated with the matrix column count per row.

Exploiting the detail that a face lies midway between two neighboring nodes reduces the difficulties of interpolating scalar values to the face centers, which is essential for the FV method. To determine the face value ϕ_f between the nodes $N1$ and $N2$ of a scalar ϕ, a central difference scheme (CDS) results in

$$\phi_f = \frac{1}{2}(\phi_{N1} + \phi_{N2}) \tag{3.12}$$

The CDS results in second-order accuracy as long as the interpolated point coincides with the center of the face. On condition that the mid-point stays within the face, the FVM has at least first-order accuracy (Ferziger and Perić, 1999) chapter 4. A complete FVM discretization with CDS interpolation for the Nabla operator, where P specifies a discrete node index, N the neighbor index and PN face quantities for the face between P and N like area A_{PN} and normal vector $\vec{n}$ results in

$$\begin{aligned} \nabla\phi_P = \frac{1}{V_P}\int_{V_P} \nabla\phi_P \, dV_P &= \frac{1}{V_P}\int_S \phi_f \cdot \vec{n} \, dS \\ &= \frac{1}{V_P}\sum_N \phi_f \, A_{PN} \cdot \vec{n}_{PN} \\ &= \frac{1}{V_P}\sum_N \frac{1}{2}(\phi_P + \phi_N) \, A_{PN} \cdot \vec{n}_{PN} \end{aligned} \tag{3.13}$$

If ϕ is a vector, equation (3.13) reduces to the divergence operator div(ϕ), for a scalar field the result is the gradient operator grad(ϕ).

3.2.2 Barycentric Interpolation

A more complex interpolation scenario arises for irregular grids. Faces often undergo a perpendicular shift that moves the face center away from the interpolated midpoint. To hold on to the second-order accuracy, the necessity for a more complex interpolation arises. An obvious choice is linear interpolation from a triangulated domain. Since the Delaunay triangulation is the dual of the Voronoi diagram (Okabe *et al.*, 2000), this can be utilized straightforward. The barycentric coordinates (Shepard, 1968) offer a simple way to interpolate at any point within a triangulated domain. As they are coordinates, they provide position information relative to a simplex (D-dimensional tetrahedral region). As a side effect, these coordinates in a normalized homogeneous form (their sum equals one) provide weight information for the specified location, as figure 3.7 illustrates. In contrast to the natural neighbor interpolation introduced by Sambridge et al. (1995) and Braun and Sambridge (1995), this method

requires always a minimal amount (D+ 1) of nodal values and does not require recursive formulas to obtain the weights.

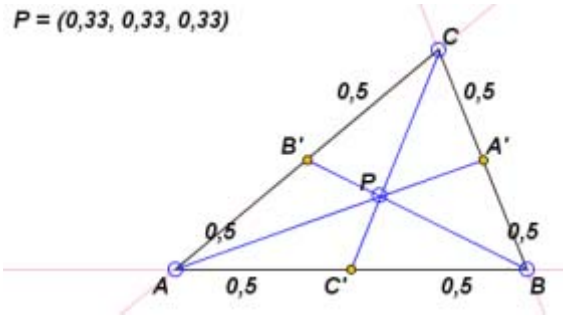

Figure 3.7 The barycentric coordinates for a point P within the triangle ABC.

Correct interpolation to the center of the face PN is now possible and by the use of barycentric interpolation remains of second-order accuracy (Ferziger and Perić, 1999, chapter 8.6.) equation (3.12) changes with the help of barycentric weights λ to

$$\phi^{fc} = \sum_{d=1}^{D+1} \lambda_d^w \phi_{\lambda_d^i} \ , \tag{3.14}$$

where λ denotes the barycentric coordinates for a D-dimensional space, including the nodal indices λ^i of the according Delaunay simplex edge and the weight (or normalized coordinate) λ^w. Figure 3.8 illustrates all variables for the two-dimensional case within a single cell.

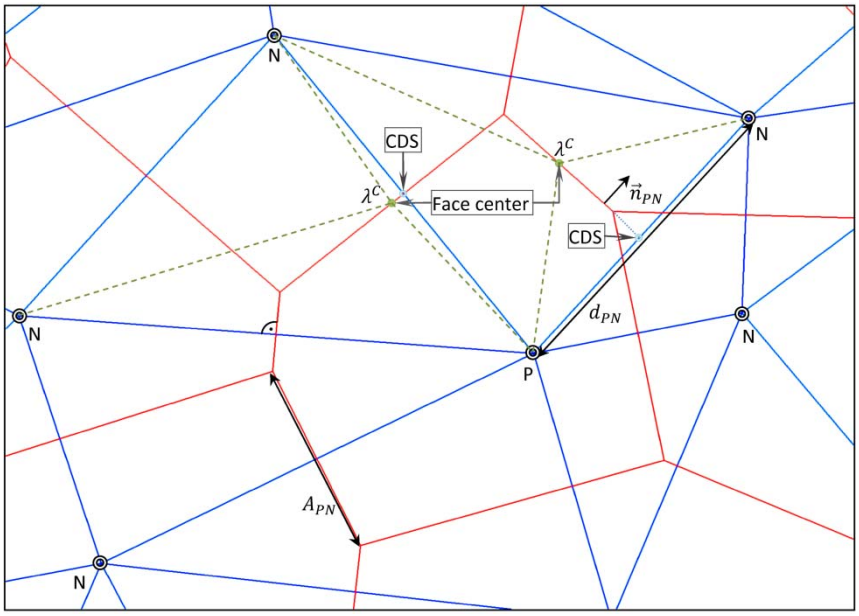

Figure 3.8: A node P surrounded by its neighbors N, with the associated Voronoi diagram in red and the Delaunay triangulation in blue. The difference between the true face center with its barycentric coordinates λ and the central difference scheme (mid-point) is highlighted as well as important components for the FVM such as area A, distance d and normal vector $\vec{n}$.

3.2.3 Deviatoric Stress Tensor

To enable the simulation to handle spatially varying viscosities, the spatial derivative of the stress tensor as part of the Navier–Stokes momentum equation is required. The definition of the deviatoric stress tensor of a velocity $\vec{v}$ and dynamic viscosity η is

$$\tau_{ij} = \eta\left(\frac{\partial v_i}{\partial x_j} + \frac{\partial v_j}{\partial x_i}\right) = \eta(\nabla\vec{v} + (\nabla\vec{v})^T) \tag{3.15}$$

and results therefore in a rank 2 symmetric tensor of D×D dimensions. It can be expressed as components of gradients of velocity components as shown in equation (3.16) for the two-dimensional case, where the diagonal parts represent the normal stresses and the off-diagonal parts shear stresses:

$$\tau_{ij} = \eta\begin{bmatrix} 2(\nabla\vec{v}_x)_{\mathrm{x}} & \left(\nabla\vec{v}_y\right)_{\mathrm{x}} + (\nabla\vec{v}_x)_{\mathrm{y}} \\ (\nabla\vec{v}_x)_{\mathrm{y}} + \left(\nabla\vec{v}_y\right)_{\mathrm{x}} & 2\left(\nabla\vec{v}_y\right)_{\mathrm{y}} \end{bmatrix} \tag{3.16}$$

The spatial derivative of this tensor results in a vector and according to the FV scheme is

$$\nabla\cdot\tau = \frac{1}{V_P}\int_{V_P}\nabla\cdot\tau\, dV_P = \frac{1}{V_P}\int_S \tau\cdot\vec{n}\, dS \tag{3.17}$$

For constant η, $\nabla\cdot\tau$ reduces to $\nabla^2\vec{v}$. The literature describes several ways to approximate the normal component to implement the Laplacian operator ∇^2. An overview is provided by Fletcher (1991) and Ferziger (1999). Usually finite difference schemes express derivatives in the normal direction at the faces. The FV implementation of equation 3.17 requires the gradients of the velocity components at the faces. Stemmer et al. (2006) recently formulated an elegant solution for the regular cubed sphere grid for collocated variable arrangement, utilizing midpoint interpolation of neighboring nodes in several directions. This technique is useful for the cubical grid-setup but fails on irregular grids.

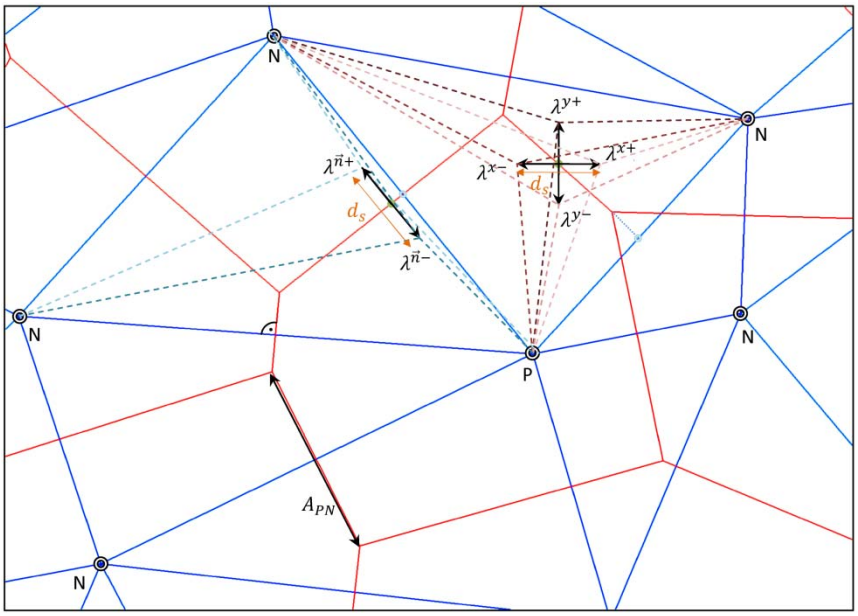

Figure 3.9: An extension to figure 3.8 with the barycentric coordinates of the constructed Cartesian cross around the face center and the two interpolation points along the normal path of a pre-defined size d_S.

Including the neighbors of the node's neighbors would resolve this issue and guarantees second-order accuracy, but also increases the size of the stencil that directly affects the size of the solution matrix and would therefore render this approach impractical. Another choice is a change to the finite-difference approach on the faces. With the help of shape functions from the barycentric coordinates (3.2.2), a Cartesian cross can be constructed from the center of a face. This enables an FD formulation at the faces as presented in figure 3.9. The FV integral for an arbitrary v_i would evolve with the interpolation sources *fi+/−* as in equation 3.12 for the Cartesian interpolation cross and *fc* for the center as

$$\begin{aligned}\int_S \tau \cdot \vec{n}\, dS &= \int_S \eta \left(\frac{\partial v_i}{\partial x_j} + \frac{\partial v_j}{\partial x_i}\right) \cdot \vec{n}\, dS \\ &= \sum_N \sum_{j=1}^{D} \frac{v_i^{fj+} - v_i^{fj-} + v_j^{fi+} - v_j^{fi-}}{d_s} \eta^{fc} A_{PN} \cdot \vec{n}_{PN}\end{aligned} \tag{3.18}$$

where d_S specifies the size of the interpolation cross. This distance can be either fixed for the whole grid or varying for every face, depending on resolution differences. It is difficult to analytically determine the optimal value for d_S, but numerical tests have shown that for a certain face area A_{PN} in a D-dimensional space $d_s = \sqrt[D-1]{A_{PN}}$ leads to a minimum of foreign neighbors (not depending on either one of the original nodes that the face divides) on strongly irregular grids.

A different problem arises with the required viscosity at the cell face (η^{fc}). Assuming the viscosity is correct at the face center, the method guarantees a second-

order truncation error by using second-order interpolants. This might not hold if the viscosity needs to be interpolated. For example, in regular grids it can be shown that the harmonic interpolant of viscosity between adjacent cells preserves continuity of the normal stress component resolved onto the face from cell-to-cell, which is closer to the physical truth of the situation. However, this does not necessarily hold true for continuity of shear stress, and suggests another viscosity interpolant might be used. An implementation of a dual stencil composed of shear and normal components of stress and their associated continuity could ensure a proper viscosity interpolant at the faces.

3.2.4 Laplacian Operator

The energy conservation as well as the momentum conservation equation for constant viscosities are expressed using the Laplacian operator ∇^2. The FV discretization results in

$$\nabla^2\phi = \frac{1}{V}\int_V \nabla^2\phi \, dV = \frac{1}{V}\int_S \nabla\phi \cdot \vec{n} \, dS \ , \tag{3.19}$$

which requires the gradient in normal direction at the cell face. The fact that only the normal direction of the gradient is required can be exploited and replaced by a CDS formulation:

$$\int_S \nabla\phi \cdot \vec{n} \, dS = \sum_N \frac{\phi_N - \phi_P}{d_{PN}} A_{PN} \tag{3.20}$$

This approximation for the face stays second-order accurate even in irregular grids since the derivative between P and N does not change within all simplexes that have both, P and N, as connectors. However, a face center can move out of those simplexes on strongly deformed cells. In this case, it is useful to introduce barycentric weights of the normal direction from the face center *fn+/−*, as illustrated in figure 3.8 as well. equation (3.20) changes to

$$\int_S \nabla\phi \cdot \vec{n} \, dS = \sum_N \frac{\phi^{fn+} - \phi^{fn-}}{d_S} A_{PN} \tag{3.21}$$

and guarantees second-order accuracy for all Voronoi cells.

3.2.5 Computational Aspects

In order to utilize the presented spatial discretization scheme, a pre-calculated Voronoi diagram and Delaunay triangulation for the same discrete set of points should exist with the following information:

- Nodal positions.
- Cell volumes.

- List of faces with their two neighbor indices (the node indices they divide), area and center.
- List of simplex indices.

The interpolation information does not change during the simulation and should be precalculated to ensure computational efficiency. One set of interpolation information consists of a simplex index that in turn holds the D+1 nodal indices λ_d^i and weight information λ_w^i. Each face usually has $2D + 3$ or $2D + 1$ interpolation points consisting of the center, the Cartesian cross and two more depending on the use of the *fn+/−* weights as described earlier.

To find a certain point within a Delaunay triangulation, it is possible to calculate the barycentric coordinates of a desired point relative to every simplex with equation (3.14) until each single coordinate lies between zero and one, as described in Section 3.2.2. The time complexity of this procedure is of order $O(n^2)$. This can be reduced to $O(n \log n)$; it is possible to index the simplex indices within a search tree. These indices correspond to node indices, which can be found in the face neighbor information as well. Since only locations close to a certain face are looked up, the simplexes containing the neighbor nodes of a face can be checked first. For extremely deformed cells, the fallback to a check-for every-simplex should exist as well.

3.2.6 Storage Requirements

Including the *fn+/−* weights, interpolation information for one face in D dimensions requires

$$(1 + D)(3 + 2D)(W + I) \tag{3.22}$$

bytes if a weight is stored with W bytes and an index with I bytes. On an average irregular grid in three dimensions, one node has approximately 14 neighbors, resulting in $7R$ faces, where R denotes the total node count. Assuming further double floating-point precision for the weights ($W = 8$) and standard 32-bit integer for indices ($I = 4$), the total memory requirement for the interpolation information is $3024R$ bytes. To reduce this enormous extra memory requirement one can exploit the fact that a weight is always only in the range between 0 and 1. Utilizing fast integer arithmetic can turn a 16-bit integer into a floating point consisting of 2^{16} steps between 0 and 1, introducing a global error of $(D + 1)/2^{16}$ and a reduction to $W = 2$, resulting in $1512R$ bytes. A reduction to $I = 3$ is only theoretically possible because it leads, if even possible, practically to misaligned memory that dramatically reduces performance.

3.2.7 Time

As space is discretized by a fixed grid, time must be discretized as well. As the energy equation is the only equation containing a time derivative, temperature is the only variable that is time-dependent by definition. The governing equations of unstea-

dy flow are furthermore parabolic in time; therefore a time-stepping method is required to advance the solution in time. In contrast to spatial discretization, the temporal discretization is flexible and can adapt with a varying time step Δt to the situation. Time is advanced over the time-step Δt as $t^{n+1} = t^n + \Delta t$. This can be summarized to the following ordinary differential equation for an unknown scalar ϕ:

$$\frac{\partial \phi(t)}{\partial t} = f\big(t, \phi(t)\big) \tag{3.23}$$

After integrating over one time-step this leads to

$$\int_{t^n}^{t^{n+1}} \frac{\partial \phi}{\partial t} dt = \phi^{n+1} - \phi^n = \int_{t^n}^{t^{n+1}} f\big(t, \phi(t)\big)\, dt \tag{3.24}$$

Applying this scheme to the energy equation (2.16) results in

$$T^{n+1} - T^n = \int_{t^n}^{t^{n+1}} \nabla^2 T - \vec{v}\, \nabla T + Q\, dt \tag{3.25}$$

This integral may be solved in many ways and many first-order approximations include the explicit forward Euler method, the implicit (or backward) Euler method or the popular Crank-Nicolson (or trapezoid) method (Crank and Nicolson, 1947):

$$\begin{aligned} \phi^{n+1} &= \phi^n + f(t_n, \phi^n)\, \Delta t \\ \phi^{n+1} &= \phi^n + f(t_{n+1}, \phi^{n+1})\, \Delta t \\ \phi^{n+1} &= \phi^n + \frac{1}{2}[f(t_n, \phi^n) + f(t_{n+1}, \phi^{n+1})\,]\, \Delta t \end{aligned} \tag{3.26}$$

These different methods have different advantages and disadvantages. While both, the forward and backward Euler method are only of first-order, the trapezoid method is second-order accurate and a mixture of implicit and explicit treatment. Explicit methods have the advantage that they are easy to implement and to parallelize but have at the same time a restriction to the time-step size (conditionally stable) and require the following stability criterion to hold:

$$\left| \Delta t \frac{\partial f(t, \phi)}{\partial \phi} \right| < 2 \tag{3.27}$$

For the application of convection-diffusion dominated problems, this criterion for the explicit forward method is restricted by a diffusive and advective area of influence from a nodal point of view. Applied to the non-dimensional form of equation (3.24), these two criteria c_1 and c_2 can be written as:

$$\begin{aligned} c_1 &= \frac{\Delta t}{\Delta x_{min}^2} \Big| c_1 < \frac{1}{2} \\ c_2 &= \frac{|\vec{v}_{max}|\Delta t}{\Delta x_{min}^2} \Big| c_2 < 2\, c_1 \end{aligned} \tag{3.28}$$

These are known as Courant criteria and can be used to calculate the adaptive time-step for explicit methods. Although the trapezoid rule is unconditionally stable, large time-steps can result in oscillatory solutions and even produce instability. To guarantee stability for the trapezoid method, the time-step taken should not be larger than twice the Δt for purely explicit methods (Ferziger and Perić, 1999, chap. 6.3).

Implicit methods have the advantage of being unconditionally stable but require the rather complex solution of a system of equations. Despite of their stable nature, it is crucial to take care of eventual time-dependent, turbulent solutions as implicit methods tend to smooth or flatten these systems into steady-state solutions. To ensure the capturing of these events, it is useful to restrict the time-step with $c_2 = 1$, which implies that the transport of mass is restricted to pass only one grid-cell for the highest velocity in the next time step. The diffusive criterion c_1 on the other hand does not require restriction as its accuracy is only limited by the first-order error.

In this work, a fully implicit second-order method, also called an implicit three-level scheme, is the method of choice. The time derivate at time t_{n+1} can be approximated by differentiating a parabola through the solutions at three time levels:

$$\left(\frac{\partial \phi}{\partial t}\right)_{n+1} \approx \frac{3\,\phi^{n+1} - 4\,\phi^{n} + \phi^{n-1}}{2\,\Delta t} \tag{3.29}$$

This leads to the following method:

$$\phi^{n+1} = \frac{4}{3}\phi^{n} - \frac{1}{3}\phi^{n-1} + \frac{2}{3} f(t_{n+1}, \phi^{n+1})\,\Delta t \tag{3.30}$$

This scheme is fully implicit since f is evaluated only at the new time level. It has the advantage that it is easy to implement (compared to the Crank Nicolson method) but requires more memory for the storage of ϕ^{n-1}. To adapt this scheme to flexible time steps, the following discretization after Harder and Hansen (2005) is employed:

$$\left(\frac{\partial \phi}{\partial t}\right)_{n+1} \approx \alpha\, \phi^{n+1} - \beta\, \phi^{n} + \gamma\, \phi^{n-1}$$

With

$$\begin{aligned} \alpha &= \Delta t_1^{-1} + (\Delta t_1 + \Delta t_0)^{-1} \\ \beta &= -\Delta t_1 + \Delta t_0 / \Delta t_1 \Delta t_0 \\ \gamma &= \Delta t_1 / \Delta t_0\, (\Delta t_1 + \Delta t_0) \\ \Delta t_1 &= t^{n+1} - t^{n} \\ \Delta t_0 &= t^{n} - t^{n-1} \end{aligned} \tag{3.31}$$

For the initial time step this scheme is reduced to the backward Euler scheme by setting $\alpha = \Delta t_1^{-1}, \beta = -\alpha,\ \gamma = 0$.

3.3 Pressure Correction

The conservation equations for mantle convection (2.14-2.16) do not include an equation for the pressure, which is required in the momentum equation. The continuity equation states that the velocity field should be divergence free to conserve mass and no other variable than velocity is present because of the incompressible treatment. The only coupling of the continuity equation with the momentum equation is therefore the pressure. An alternative approach is to solve for velocity and pressure together, but this would lead to a large matrix and make the solution impractical for larger grids. To encounter this problem, a segregated approach divides the solution for one time-step into three groups; the three components of the velocity field, the pressure and the temperature are solved for individually and consequently checked for convergence.

The equation for pressure must be set up such that a divergence free velocity field is ensured while providing a solution to the momentum equation. A method proposed by Caretto et al. (1972) and Patankar (1980) called SIMPLE was adopted to solve this coupling. It uses a process to correct the pressure with a portion of the Laplacian of the divergence field that originates from the velocities calculated by the momentum equation. The absence of inertia forces makes this coupling very weak (velocity correction is not possible) and requires an under-relaxation scheme, which is similar to introduce artificial compressibility to increase the coupling. Here, the proposed $\tilde{\alpha}$ under-relaxation method after Ferziger and Perić (1999, section 5.4.3) was applied, but many other methods like artificial incompressibility are possible. These work basically alike and yield similar convergence rates if properly employed. The pressure is split into a correction term δp and the pressure field of the previous nth inner iteration p^n, where only a portion $(1 - \acute{\alpha})$ of δp is added:

$$p^{n+1} = p^{n} + (1 - \acute{\alpha})\delta p \tag{3.32}$$

$$-\nabla \cdot \vec{v} = \nabla \cdot \left(\frac{1}{-\bar{A}_{P,mm}} \nabla \delta p\right) \tag{3.33}$$

The mean central weight (averaged from the x, y and z component) from the momentum equation $\bar{A}_{P,mm}$ acts as a pre-factor for the Poisson equation (3.13) that

solves for the correction term from the divergence of the velocity field ($\nabla \cdot \vec{v}$) originating from the momentum equation. It is important to note that $\bar{A}_{P,mm}$ must not contain the factor $\acute{\alpha}$ in contrast to the weights used to solve for the velocity field within the momentum equation. The corrected pressure is applied to the momentum equation and solved consequently in turn until δp is sufficiently small or the difference of the norm of the divergence reaches a certain limit.

The iterative process for one time-step can be summarized as follows:

1. Solve energy equation; take velocities from previous time-step as a first guess for the first loop.
2. Solve for the velocity using the momentum equation for the present temperature and viscosity field while taking the previous pressure field or some initial value field. This results in a divergent velocity field in the first loop.
3. Solve the Poisson equation (3.33) to acquire the correction term for the pressure field and apply the correction (3.32).
4. Repeat from step two until $\|\delta p\|$ is sufficiently small (inner loop).
5. Repeat from step one until temperature residuum to previous iteration is sufficiently small (outer loop)

The under-relaxation factor $\acute{\alpha}$ controls within the iterations the significance of either the continuity equation or the momentum equation, i.e. what should be emphasized, a divergence free velocity field or a velocity field that is close to the solution of the momentum equation. A factor close to one leads to less outer iterations while the amount of inner iterations increase and vice-versa. The final result is for any choice of $\acute{\alpha}$ similar as long as $0 < \acute{\alpha} < 1$. The preferred value of $\acute{\alpha}$ is around 0.8, as predicted by Ferziger and Perić (1999, section 7.5.2).

3.4 Initial Conditions

At the beginning of the simulation ($t = 0$) all variables involved within the partial differential equations must be defined. The velocities are set to zero as well as the pressure, as the pressure correction quickly establishes a hydrostatic equilibrium. Depending on the type of evolution the temperature field can either be set to a cold start ($T = 0$) or a hot start ($T = 1$). In most cases we are interested in the (quasi-) steady state and the temperature field is set to its conductive profile, which stems from an analytic solution of the heat equation and is only radially dependent (1D). The temperature profile for bottom heated convection as function of radius with $r_r = r_i/r_o$ as the radius ratio is defined as

$$T(r) = \frac{r_r}{1 - r_r}\left(\frac{1}{(1 - r_r)r} - 1\right) \tag{3.34}$$

For purely internally heated convection with an insulating lower boundary condition this equation changes to

$$T(r) = \frac{1}{6}\left(-r^2 + r_i^3 \left(\frac{-2}{r} + \frac{2}{r_o}\right) + r_o^2 \right) \tag{3.35}$$

The above equations are designed for dimension-less variables of r and T.

It is possible to impose a certain lateral pattern of the initial temperature profile to force the convection to establish a certain symmetry. This is often helpful in steady-state convection models to compare certain symmetries under limited conditions, and in particular benchmarking the simulation with other published results. To establish these symmetries, a spherical harmonic perturbation is added to the initial temperature profile

$$T(\theta, \varphi, \mathrm{r}) = T(r) + \iota\, Y_l^m(\theta, \varphi)\, \sin(\pi r - r_o), \tag{3.36}$$

where ι is the amplitude of the perturbation.

The sin term leads to largest distortions at mid-radius. The amplitude ι does not equal the variations at mid-depth and must be adapted to the mode. Compositional modes are possible, as the cubical symmetry requires a combination of $Y_4^4 + Y_4^0$. A tetrahedral symmetry consists of Y_3^2.

3.5 Boundary Conditions

To construct boundary conditions for a spherical shell that is enclosed between the inner radius r_i and the outer radius r_o, two ghost shells are created that lie below r_i and above r_o so that the Voronoi cells naturally create faces exactly at those radii and therefore guarantee correct volumes. It should be emphasized that these additional cells do not lie at the boundary of the system. Rather, they are constructed such that a face is created at the boundary that coincides with the radii. For a system comprised of n shells, the boundary shells r_0 and r_{n+1} are located at

$$\begin{aligned} r_{n+1} &= r_n + 2(r_o - r_n) \\ r_0 &= r_i - 2(r_1 - r_i) \end{aligned} \tag{3.37}$$

Temperature

The non-dimensional form of the energy equation requires a fixed zero-temperature at the top boundary to cool the interior. Therefore the top boundary condition for temperature is of Dirichlet type. In case of bottom heated convection, the bottom boundary condition is similar and given by

$$T|_{r=r_i} = T_1 = 1 \qquad T|_{r=r_o} = T_0 = 0 \tag{3.38}$$

In case of purely internally heated convection, the inner boundary requires thermal insulation, which is accomplished by prescribing a Neumann boundary condition of zero heat-flux:

$$\left.\frac{\partial T}{\partial r}\right|_{r=r_i} = 0 \tag{3.39}$$

The numerical implementation for a scalar Dirichlet boundary condition with the defined ghost cells must be chosen such that the interpolated value at the boundary face equals the desired temperature:

$$\begin{aligned} T_{r_0} &= 2 - T_{r_1} \\ T_{r_{n+1}} &= -T_{r_n} \end{aligned} \tag{3.40}$$

For the Neumann boundary condition the energy exchange with the inner boundary shell is simply ignored by setting the corresponding matrix element to zero.

Velocity

The boundary conditions for the velocity field determine the interface properties between the core and the convecting mantle as well as the surface and the convecting mantle. While the outer core is mostly considered as liquid, a free-slip (stress-free) boundary condition is employed to describe this interface correctly. For the outer boundary this scenario is different. If one wants to simulate the complete mantle up to the surface, mostly done for plate-tectonic related research, a free-slip boundary is appropriate while on the other hand, a thin immobile crust is mostly present that can be seen as sitting on top of the mantle and does not interact with the interior anyway, making a rigid outer boundary condition appropriate.

To describe these two conditions, the velocity vector is decomposed into a lateral part projected onto the boundary and a radial part

$$\begin{aligned} \vec{v}_r &= (\vec{v} \cdot \vec{e}_r)\, \vec{e}_r \\ \vec{v}_{lat} &= \vec{v} - \vec{v}_r \end{aligned} \tag{3.41}$$

where $\vec{e}_r$ is the unity vector in the radial direction.

The impermeability condition is met by presuming

$$\vec{v}_r|_{r=r_i,r_o} = 0, \tag{3.42}$$

while the no-slip condition additionally requires

$$\vec{v}_{lat}|_{r=r_i,r_o} = 0, \tag{3.43}$$

In case of a stress-free boundary condition, all non-diagonal terms of the stress tensor must vanish ($\mathbb{I}$ is the identity tensor):

$$\vec{v}_{lat} \cdot [-p\mathbb{I} + \eta\,(\nabla\vec{v} + (\nabla\vec{v})^T)]\vec{e}_r|_{r=r_i,r_o} = 0 \tag{3.44}$$

The implementation of these boundary conditions on the boundary shells is straight forward. The radial component is generally inverted while for the no-slip condition together with an inverted lateral component results in $\vec{v} = 0$ at the interface:

$$\begin{aligned} \vec{v}_{r=0} &= -\vec{v}_{r,r=1} - \vec{v}_{lat,r=1} \\ \vec{v}_{r=n+1} &= -\vec{v}_{r,r=n} - \vec{v}_{lat,r=n} \end{aligned} \tag{3.45}$$

For the stress-free (free-slip) condition, the above equation changes to

$$\begin{aligned} \vec{v}_{r=0} &= -\vec{v}_{r,r=1} + \frac{r_0}{r_1}\vec{v}_{lat,r=1} \\ \vec{v}_{r=n+1} &= -\vec{v}_{r,r=n} + \frac{r_{n+1}}{r_n}\vec{v}_{lat,r=n} \end{aligned} \tag{3.46}$$

While the lateral part stays unchanged (stress-free), the radial part is eliminated to remove unphysical material flux within the energy equation originating from remaining divergence close to the boundary.

Pressure

The pressure gradient within the momentum equation has no boundary condition because otherwise the problem would be over-determined. Because pressure is a primitive variable and is used to ensure minimal divergence, it is necessary to ensure a continuous pressure field. A simple extrapolation method ensures this condition, requiring three interior pressure values that lie below / above the boundary shells for second-order accuracy.

$$\begin{aligned} p_{r=0} &= \frac{1}{2}(5\,p_{r=1} - 4\,p_{r=2} + p_{r=3}) \\ p_{r=n+1} &= \frac{1}{2}(5\,p_{r=n} - 4\,p_{r=n-1} + p_{r=n-2}) \end{aligned} \tag{3.47}$$

The above equation is applied to grids with constant shell spacing Δr. For grids with varying shell spacing, a similar scheme as described in the time-discretization section (3.2.7) can be employed. For irregular grids, the pressure values required must be interpolated with barycentric weights. It is useful to create a cache at the beginning of the simulation for these weights since finding the simplex corresponding to an arbitrary position and the evaluation of the weights are time-consuming operations.

A final boundary condition is required for the pressure correction (section 3.3). The Laplacian of the correction term δp requires Neumann boundary conditions to be employed. Therefore the boundary condition for equation (3.33) is

$$\left.\frac{\partial\, \delta p}{\partial r}\right|_{r=r_i,r_o} = 0 \tag{3.48}$$

3.6 Parallelization – Domain Decomposition

To run a simulation with high resolution, the code must work with more than one CPU in parallel. Typically, a domain decomposition of the grid is applied, which results in an optimal breakdown of the grid into $\tilde{p}$ equal volumes where each of the domains is assumed to a single processor. An efficient domain decomposition minimizes the area between these sections, leading to a minimized overhead of data exchange between the processors.

Halo-cells, sometimes called ghost-cells, arise in domain decomposition as additional cells in each domain, which form an overlapping zone where data is exchanged. These cells border each domain and are on the same position as their active cells on the neighboring domain. The ratio between halo-cells and grid cells is a first measure of efficiency for parallelization. This ratio is vital to determine the amount of data exchanged between the domains.

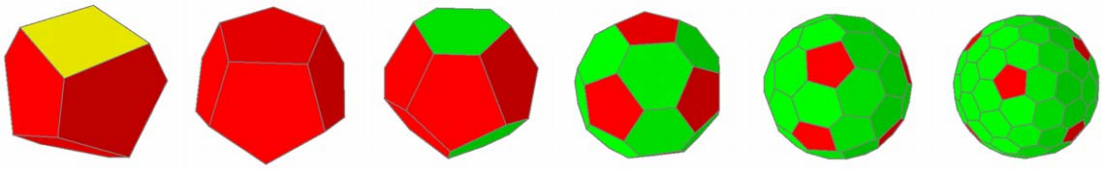

Figure 3.10. Voronoi diagrams of certain Thomson configurations; namely for $\tilde{p}$=10, 12, 16, 32, 64, 128 and 256 electrons. Green areas mark hexagons, red pentagons and yellow tetragons.

One approach to laterally decompose a sphere is to distribute $\tilde{p}$ points on the surface of a unit-sphere, assume all with equivalent potential energy and minimize the global potential field energy. Figure 3.10 displays some configurations, where the patches on the surface would mark the region of one domain. This approach is known as the Thomsom Problem[2] (Thomson, 1904). After this step, its closest "Thomson" point derives the domain affiliation for every cell. The resulting decomposition as shown in figure 3.11 leads to equal domain volumes, which is important to balance the computational efforts for each CPU. Some p reproduce platonic solids; $p = 4$ creates a tetrahedron, $p = 6$ a cube and $p = 12$ a dodecahedron. However, all p>1 show a certain symmetry (Wales and Ulker, 2006).

[2] For an interactive demonstration please see
http://physics.syr.edu/thomson/thomsonapplet.htm (11.02.2009)

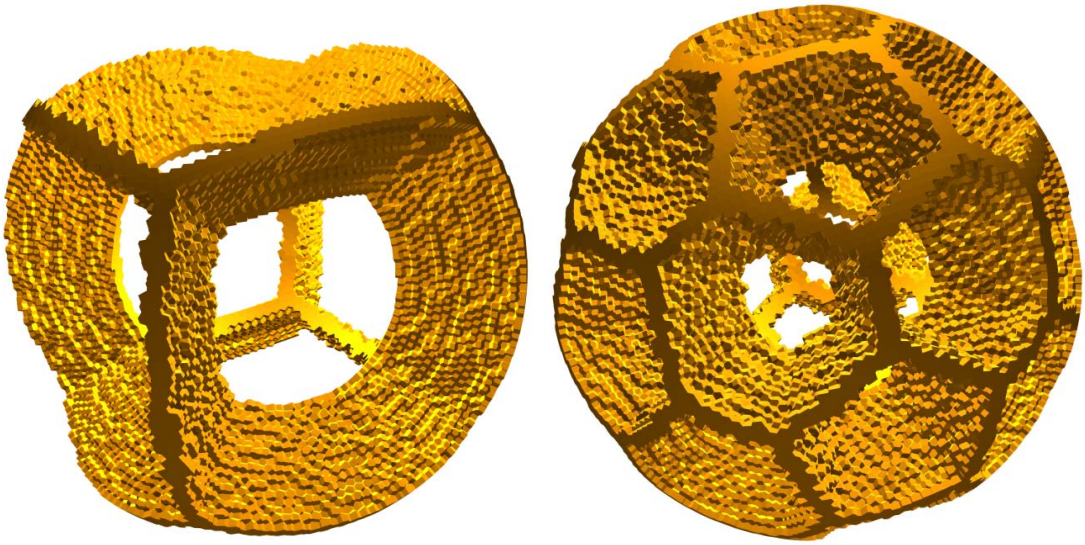

Figure 3.11 shows the resulting halo-cells after a domain decomposition of the spiral grid with a radius ratio of 0.55 and 16 shells. Left: Domain decomposition for six CPUs (equal to the cube); Right: 32 CPUs.

The correct calculation of the Thomson locations on the unit sphere requires itself supercomputers for larger ($\tilde{p} > 16$) quantities, so publicly available pre-computed positions from the Cambridge University serve as input for up to $\tilde{p} = 400$ for the closest-distance association. With an additional choice of one radial slice of the spherical shell, the limit on usable CPU cores doubles to $\tilde{p} = 800$.

The performance of this decomposition method was tested on two supercomputing centers and two local shared memory machines. To evaluate the performance, the same initial setup was taken and run on several node counts. The ratio of the execution time determines the speedup. This speedup shows for some architecture an almost ideal linear correlation for up to 256 tested CPUs, suggesting an efficient minimization of ghost-points. Figure 3.12 shows the speedup factor that determines the acceleration of the code for the same problem size on various CPU counts. The IBM JUMP cluster consists of 41 nodes, each containing 32 p690 CPUs. The CLX system at the CINECA supercomputing center in Bologna, Italy, consists of 1024 Intel XEON CPUs with 3GHz.

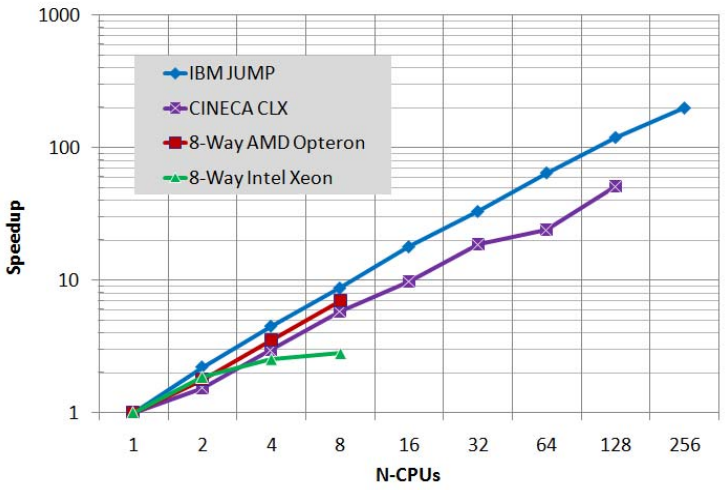

Figure 3.12 shows a performance test with an applied Thomson domain decomposition for various supercomputer clusters and local shared memory machines. A generally better scaling can be observed with recent AMD clusters (Opteron K10) compared to current Intel technology (Xeon 5355).

3.7 Wavelength Analysis

The power-spectra or wavelength analysis provides a powerful tool to quantify structural complexities within a convecting system. For a three-dimensional spherical shell, the lateral variations of a certain scalar field are decomposed into a series of wavelengths and their powers, much like a Fourier transformation of a function in two dimensions. While in 2D this decomposition consists of a certain frequency and its associated power (or amplitude), on the surface of a sphere one more structural indicator exists, i.e. the degree ℓ (≥ 0), the order m ($|m| \leq l$) and their associated power. Figure 3.13 illustrates the first three degrees and orders of the spherical harmonic function $Y_l^m(\theta, \varphi)$. In signal processing literature, the total power of a function or scalar field is defined as the integral of the function squared divided by the area it spans (Buttkus, 2000). To calculate the spherical harmonic functions, the common orthonormalization was used to create the angular power spectrum $S_{ff}(\ell) = \lambda_\ell$. This quantity specifies the power of a certain signal, combining all possible orders of degree ℓ.

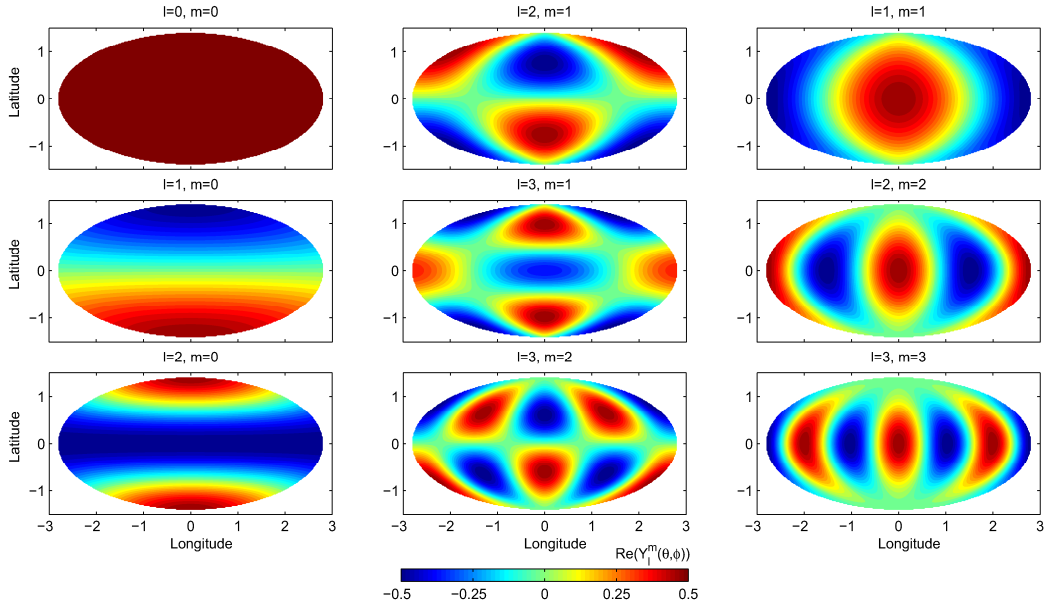

Figure 3.13 shows the equal-area map projection of the first three degrees and orders, which is equivalent to the normalized real part of the spherical harmonic function.

The spherical shell consists of radial layers that were individually analyzed for modes up to a degree and order of 30. The zero-mode was eliminated before the analysis by subtracting the mean value of the field. Radially summing these power spectra provides a one-dimensional spectrum of modes that reflects the structural complexity of the whole shell:

$$\lambda_\ell = \sum_r \lambda_{r,\ell} \tag{3.49}$$

The power spectrum of the temperature field is of prime interest because it is directly associated with the amount of uprising mantle plumes; a dominant degree-one for example refers to one upwelling and one downwelling, yielding major implications on the appearance of topography and the geoid. The depth of the maximum power yields implications for the location of the thermal boundary layer, as they exhibit the largest lateral temperature variations.

To obtain a single parameter to describe the structural complexity of the convecting system other than the dominant mode, which is the mode with the maximum power, a weighted mode is computed to account for multiple occurrences of strong modes. This method is similar to the robust-localization method (Kertz, 1973, Buttkus, 2000). A spectrum is not necessarily centered on the dominant mode, as figure 3.14 demonstrates. A weighting function that weights the power of a mode with its own degree yields a center-of-mode, similar to the definition of a one-dimensional center-of-mass, or weighted average:

$$\omega = \frac{\sum \ell \, \lambda_\ell}{\sum \lambda_\ell} \tag{3.50}$$

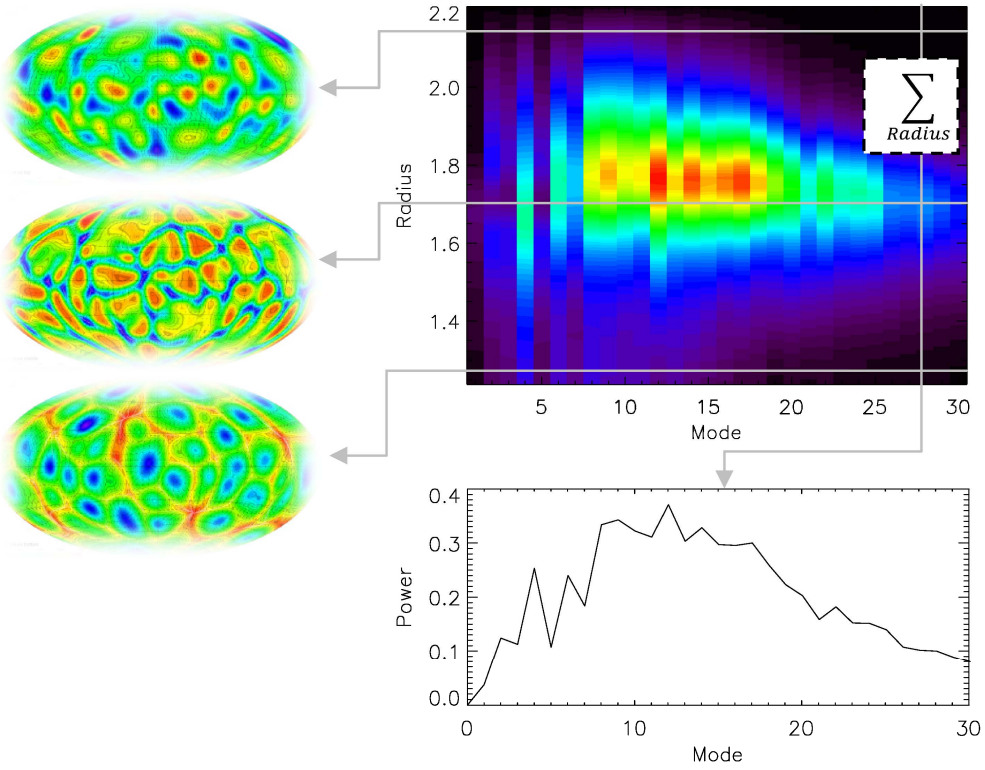

Figure 3.14 shows the result of a spectrum analysis of case 3 (see Appendix A), where the left side shows normalized temperature field projections of the top, middle and bottom shell and the resulting spectral map. The boundary layer, which is in this case right above the middle shell, has the largest temperature variations, which is why it appears brighter. As there are different sized shapes in the projection, there are different modes that have high powers. The sum over the radius leads to the bottom plot that shows the summed power of each mode within the convecting system.

4 Validation

The output data of the simulation is stored at pre-defined times, usually time-step intervals, that include the variables of interest at all nodal locations. These data-sets can be utilized to study, visualize and validate the precision of the numerical method or grid. Global diagnostic values, as further specified in section 4.1 help to quantify certain aspects of the data-set. With these globally averaged values, together with local minima / maxima, it is possible to compare individual parameter sets with published results as presented in section 4.3. In addition, the heat conduction equation is used as a locally verifiable, analytically known solution in section 4.2.

4.1 Diagnostic Values

Local quantities

The velocities of up- and downwellings vary strongly for different Rayleigh numbers and rheologies and especially for temperature- and pressure-dependent viscosities. To measure those quantities in a uniform way, the radial min/max velocities at mid-depth $r_m = r_i + \frac{1}{2}(r_o - r_i)$ are determined according to

$$v_r' = \mathrm{sgn}(\vec{v}_r \cdot \vec{e}_r)\ |\vec{v}_r| \tag{4.1}$$

$$\begin{aligned} v_{r,mid,max} &= \max(v_r')|_{r=r_m} \\ v_{r,mid,min} &= \min(v_r')|_{r=r_m} \end{aligned} \tag{4.2}$$

Additionally the local min/max temperatures at mid-depth are quantified for comparison with published results:

$$\begin{aligned} T_{mid,max} &= \max(T)|_{r=r_m} \\ T_{mid,min} &= \min(T)|_{r=r_m} \end{aligned} \tag{4.3}$$

Temporal fluctuations of these local quantities are neglected for simplicity and only the last snapshot is evaluated.

Global quantities

Many global quantities originate from a reduced one-dimensional depth profile for which the quantity of interest is laterally averaged and therefore only a function of radius $\langle\cdot\rangle_{lat}(r)$. An important global quantity is the internal temperature, which is defined as the laterally averaged temperature in the convecting interior. Its importance is evident from the definition of the internal Rayleigh number which is based on the vis-

cosity at the internal temperature and plays a vital role in many scaling laws. It is best described by the laterally averaged temperature at the depth of the maximal radial velocity $\vec{v}_r$:

$$\begin{gathered} T_i = \langle T \rangle_{lat}(r') \\ r' = \left\{ r \in [r_i, r_o] \colon \langle |\vec{v}_r| \rangle_{lat}(r') = \max\left(\langle |\vec{v}_r| \rangle_{lat}(r) \right) \right\} \end{gathered} \tag{4.4}$$

Another important parameter to quantify thermal-convection models is the Nusselt number Nu. It represents the ratio of total heat-flux to the purely conductive heat-flux and therefore quantifies the strength of convection (e.g., Turcotte and Schubert, 1982). A Nusselt number of one specifies no active convection; heat is transported entirely by conduction. If the Rayleigh number exceeds a critical value, convection sets in and the Nusselt number increases, thus implying a strong relation between these two parameters as both determine the strength of convection.

The heat-flux is observed in radial direction by using the depth profile of temperature and is composed of a convecting part

$$q_{conv}(r) = \langle \vec{v}_r \, T \rangle_{lat}(r) \tag{4.5}$$

and a conductive part, that can be defined for bottom-heated convection with the geometry parameter $r_r = r_i / r_o$ as

$$q_{cond}(r) = -\frac{\kappa}{r_r} \frac{\partial \langle T \rangle_{lat}}{\partial r}, \tag{4.6}$$

together with the internally generated heat-flux for mixed-mode heating scenarios

$$q_H(r) = \langle Q \rangle_{lat} r \tag{4.7}$$

the Nusselt number is defined as

$$Nu(r) = \frac{q_{conv}(r) + q_{cond}(r) + q_H(r)}{q_{cond}(r) + q_H(r)} \tag{4.8}$$

For mixed-mode heating or purely bottom heating scenarios, the conductive heat-flux is radially independent and can be expressed as

$$q_{cond} = \frac{\kappa \Delta T}{d} + q_H \tag{4.9}$$

This equation changes the Nusselt number definition to $Nu(r) = q_{total}(r)/q_{cond}$ and further simplifies at the inner and outer boundaries of the convecting system because only conductive heat-flux is present there due to the impermeable wall boundary condition. For the non-dimensionalized case these upper and lower Nusselt numbers can be expressed as

$$Nu_{top} = -\frac{1}{a}\left.\frac{\partial \langle T \rangle_{lat}}{\partial r}\right|_{r=r_o}$$
$$Nu_{bottom} = -a\left.\frac{\partial \langle T \rangle_{lat}}{\partial r}\right|_{r=r_i} \tag{4.10}$$

For purely internally heated convection, the internal temperature T_i as defined in equation 4.4 is directly related with the heat-flux and Nusselt number because the temperature scale is different for this type of convection, as later explained in section 5.1. In this case, T_i is best defined as the maximum horizontally averaged temperature within the convecting system as no hot inner boundary exists. The maximum non-dimensional temperature T_C in such systems is reached only in a non-convecting scenario and is defined as

$$T_C = \frac{1}{6} r_o^2 \left(1 - \frac{3r_i^2}{r_o^2} + \frac{2r_i^3}{r_o^3}\right) \tag{4.11}$$

The Nusselt number is then defined as (Reese 98):

$$Nu_H = \frac{T_C}{T_i} \tag{4.12}$$

Other global quantities of interest are the volume averaged temperature $\langle T \rangle$ and the root-mean-square velocity v_{rms}, which is given by

$$v_{rms} = \left(\frac{1}{V}\int_x \int_y \int_z (v_u^2 + v_v^2 + v_w^2) dx\, dy\, dz\right)^{\frac{1}{2}} \tag{4.13}$$

The implementation of this equation in a discretized finite-volume scheme with n cells and their volume V can be expressed as

$$v_{rms} = \left(\frac{1}{\sum_{i=1}^{n} V_i} \sum_{i=1}^{n} V_i (v_{i,u}^2 + v_{i,v}^2 + v_{i,w}^2)\right)^{\frac{1}{2}} \tag{4.14}$$

4.2 Comparison with Analytical Solutions

To test the applicability of the spiral grid and the numerical approach presented in section 3 for fluid dynamic calculations, a simple heat diffusion scenario in the spherical shell with fixed boundary conditions at the inner and outer radius is set up. This enables a comparison of the numerical solution based on the spiral grid with the analytical solution of the boundary value problem of the Laplace-equation.

The following Laplace equation illustrates the problem and is applied to the spiral discretization and compared to analytic results, where ψ represents a scalar value within a discretized spherical shell.

$$\nabla^2\psi = 0 \tag{4.15}$$

The boundary conditions for this problem were prescribed on both boundaries, with a value of one at the inner and a value of zero at the outer radius. This setup is equivalent to a time-independent solution of heat transfer through a spherical shell, heated from below without internal heat sources or sinks.

The analytical solution to (4.15) for any discrete ψ within a spherical shell is given by

$$\psi = \psi_i + \frac{r_o(r_\psi - r_i)(\psi_o - \psi_i)}{r_\psi(r_o - r_i)} \tag{4.16}$$

where ψ_o and ψ_i represent the outer / inner boundary value of ψ, r_o and r_i the outer / inner radius of the spherical shell and r_ψ the radius of ψ. With respect to heat diffusion, equations (4.15) and (4.16) describe a conductive temperature profile in a spherical shell.

Resolution	Nodes	Grid-type	$\overline{\lvert S-s \rvert}$	σ	$\lVert \overline{S-s} \rVert_\infty$	CPU time in sec.	Iterations
0.04	106677	VD	1.072E-3	1.513E-3	1.0745E-2	3.9	25
0.03	266725	VD	7.995E-4	1.112E-3	8.7012E-3	13.5	34
0.02	815302	VD	6.270E-4	8.539E-4	6.2967E-3	57.3	47
0.04	106677	CVD	7.502E-4	1.042E-3	1.0284E-2	3.8	25
0.03	266725	CVD	5.296E-4	7.356E-4	7.3207E-3	13.1	33
0.02	815302	CVD	4.412E-4	6.019E-4	5.9523E-3	57.0	45

Table 4.1 Comparison of the numerical and analytical solution of a boundary value problem describing a conductive temperature profile. Resolution denotes the grid spacing of the spiral grid with the respective number of nodes of the Voronoi diagram (VD) and the centroidal Voronoi Diagram (CVD). The mean absolute deviation, the standard deviation σ, the max absolute error are given each with the required computing time in seconds and the number of iterations, where S stands for the analytical and s for the numerical solution.

To solve equation (4.15) on various grids, an implicit method using the freely available PETSc solver (Balay *et al.*, 2004) was used on a single 64 bit Opteron with 2.2GHz. The solver uses a block-Jacobian pre-conditioner with a Krylov-subspace CGstab method. Table 4.1 summarizes results for three grid resolutions for the Voronoi diagram (VD) and the centroidal Voronoi Diagram (CVD). The results show an excellent agreement with even low resolution grids and an expected first-order reduction of the error (resulting from a one-dimensional problem) to the grid resolution. The CVD version shows generally lower errors and confirms the advantage compared to the VD version. The inclusion of PETSc as a third-party black box solver was discarded in later

studies in exchange for an independent implementation of a matrix class and BiCGS solver, mainly for speed reasons regarding parallel performance.

4.3 Comparison to Published Results

Mantle convection is modeled by thermal convection of a Boussinesq fluid at infinite Prandtl-number heated from the bottom of the spherical shell. The ratio of the inner to the outer radius of the spherical shell is 0.55, similar to the Earth's mantle. Boundary conditions are given by impermeable and free-slip conditions for the velocities and fixed temperatures T=1 at the inner and T=0 at the outer radius. The non-dimensional forms of the equations of mass, energy and momentum conservation result from scaling the equations with intrinsic parameters like the thickness of the spherical shell d, the thermal diffusion time and the temperature difference ΔT between the boundaries. The conservation equations are therefore equivalent to those of chapter 2.

To solve the conservation equations (2.14-2.16), a second-order finite volume discretization scheme as described in chapter 3 with a co-located velocity / pressure alignment was applied. A Jacobi pre-conditioner with a Krylov-subspace BiCGstab method (Saad, 1996, Meister, 2005) was implemented to solve the pressure correction equation for the SIMPLE algorithm as well as for the energy and momentum equation.

The BiCGStab method is based on the non-symmetric Lanczos algorithm (Lanczos, 1950, Lanczos, 1952). Special attention is required for a possible break-down of this algorithm, whereas the Lanczos recursion terminates without reaching a solution for the system of equations. This property brought the BiCGStab method into discredit but recent research (e.g., Sleijpen *et al.*, 1994, Sleijpen and van der Vorst, 1995, Wang and Sheu, 1997, Fish *et al.*, 1999) sows that this can almost always be circumvented.

Thermal convection in a spherical shell at infinite Prandtl-number has two stable solutions with polyhedral symmetry when the Rayleigh number is low (e.g., Busse, 1975, Schubert *et al.*, 2001). These steady-state flow patterns with tetrahedral and cubic symmetry have been used to compare different published spherical models with various discretization schemes and numerical methods (Stemmer *et al.*, 2006). To initiate these steady state patterns, the initial conductive temperature field is perturbed with a normalized spherical harmonic mode (section 3.4). The mode Y_3^2 yields a tetrahedral flow pattern and $Y_4^0 + Y_4^4$ results in a cubically symmetric flow in a certain range of Rayleigh numbers. The tetrahedral symmetry has four upwellings and the cubic symmetry has six upwellings as the steady-state for a Rayleigh number of 7000 is displayed in figure 4.1.

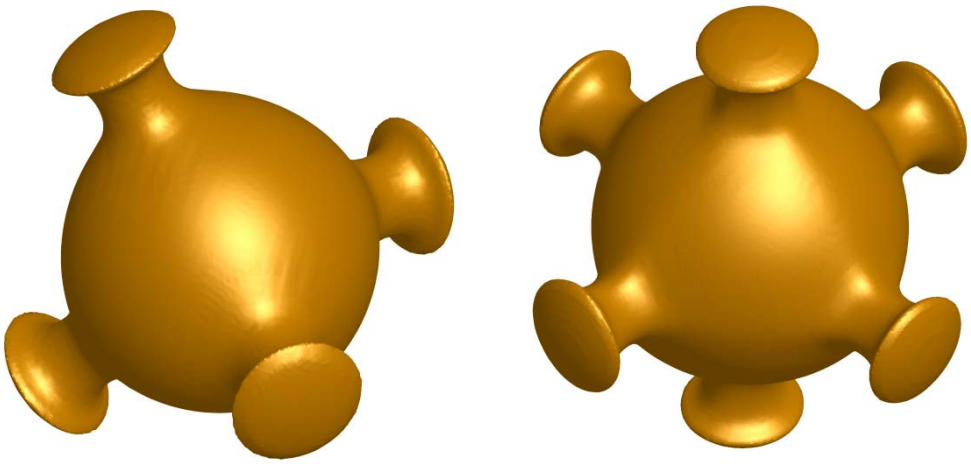

Figure 4.1: The iso-surface of temperature with T=0.5 of a tetrahedral (left) and cubical (right) steady-state. The Rayleigh number is 7000 and the convection is isoviscous.

			tetrahedral (l,m)=(3,2)			cubic (l,m)=(4,0)+(4,4)		
Model	Method	Nodes	Nu_{T0}	Nu_{T1}	v_{rms}	Nu_{T0}	Nu_{T1}	v_{rms}
Be89	SP	2400	3.4657	3.5293	-	-	-	-
Zh00	FE	165888	3.5190	3.4270	-	-	-	-
Iw96	FV	532480	3.4500	-	32.417	-	-	-
TS00	FE	324532	3.6565	-	32.936	-	-	-
Ha98	SP	552960	3.4955	-	32.637	3.6086	-	31.076
Ra96	FV	200000	3.4423	-	32.190	3.5806	-	30.870
YK04	FD	2122416	3.4430	-	32.048	3.5554	-	30.518
St06	FV	663552	3.4864	3.4864	32.589	3.5982	3.5984	31.023
This	FV	133084	3.5142	3.5184	32.783	3.6137	3.6180	31.168

Table 4.2 Comparison of bottom and top Nusselt numbers, NuT0 and NuT1, and volume-averaged rms-velocities, vrms, of tetrahedral and cubic steady-state flow patterns of thermal convection in a spherical shell. 'Be89' indicates results by (Bercovici et al., 1989), 'Zh00' by (Zhong et al., 2000b), 'Iw96' by (Iwase, 1996), 'TS00' by (Tabata and Suzuki, 2000), 'Ha98' by (Harder, 1998), 'Ra96' by (Ratcliff et al., 1996b), 'YK04' by (Yoshida and Kageyama, 2004) and 'St06' by (Stemmer et al., 2006). The respective discretization method is given where 'SP' indicates spectral, 'FE' finite elements, 'FD' finite differences and 'FV' finite volumes. Nodes denote the total number of nodes.

To test for steady-state solutions, the diagnostic values (Nusselt number, root-mean-square velocity) are evaluated and the steady state is assumed to be reached if these values change less than 10^{-6} in one time-step. Table 4.2 illustrates the resulting diagnostic parameters of steady-state convection in a spherical shell for a Rayleigh-number of *Ra=7000* in comparison to other published models for isoviscous convection. The results agree well to within a few percent. The remaining differences are caused by the different numerical grids, grid resolutions and discretization methods applied. A convergence test with equal input parameters for tetrahedral flow with a projected icosahedra grid (see section 3.1.2) results in the bottom Nusselt numbers (3.3105, 3.4514, 3.4848, 3.4897) for an increasing radial/lateral grid resolution of (8/642, 16/2562, 32/10242, 48/10242) nodes.

In order to verify the accuracy of the presented numerical technique for fully spatially variable viscosity, several results from published mantle convection models were reproduced. According to linear stability analysis (e.g., Busse, 1975), two stable solutions for thermal convection in the three-dimensional spherical shell with an inner to outer radius ratio of 0.55 exist if the system is purely bottom heated. The applied rheology law for the viscosity variations with temperature is the widely used Frank-Kamenetskii approximation that limits the viscosity contrast to a fixed value $\Delta\eta_T$ (Frank-Kamenetskii, 1969, Reese *et al.*, 1999a):

$$\eta = \exp\left(\ln \Delta\eta_T \left(T_{ref} - T\right)\right) \tag{4.17}$$

Because the definition of the Rayleigh number includes the viscosity, a reference temperature T_{ref} is introduced at which the viscosity for the Rayleigh number is evaluated. In all benchmark studies with varying viscosities this reference temperature is 0.5. Usually this temperature is denoted as a subscript to the Rayleigh number: $Ra_{0.5} = \cdots$. This temperature can be arbitrarily chosen and does not alter the results if the Rayleigh number is re-evaluated with the applied rheology law (in this case equation 4.17).

Tetrahedral symmetry			$\Delta\eta T = 1$		$\Delta\eta T = 10$		$\Delta\eta T = 20$	
Model	Method	Nodes	Nu_{T0}	v_{rms}	Nu_{T0}	v_{rms}	Nu_{T0}	v_{rms}
Ha98	SP	552960	3.4955	32.6375	-	-	-	-
Ra96	FV	200000	3.4423	32.19	3.2337	26.80	3.1615	25.69
YK04	FD	2122416	3.4430	32.0481	-	-	3.133	26.1064
St06	FV	663552	3.4864	32.5894	3.2398	27.2591	3.1447	25.7300
This	FV	327744	3.4848	32.6535	3.2346	27.2513	3.1444	25.7139
Cubic symmetry			$\Delta\eta T = 1$		$\Delta\eta T = 20$		$\Delta\eta T = 30$	
Ha98	SP	552960	3.6086	31.0765	-	-	-	-
Ra96	FV	200000	3.5806	30.87	3.3663	25.17	3.3285	24.57
YK04	FD	2122416	3.5554	30.5197	3.3280	25.3856	-	-
St06	FV	663552	3.5982	31.0226	3.3423	24.9819	3.2864	24.1959
This	FV	327744	3.5953	31.0704	3.3631	25.1521	3.2747	24.1568

Table 4.3 Comparison of the bottom Nusselt number and the rms-velocity for the tetrahedral and cubic steady-state convection with a viscosity contrast of $\boldsymbol{\Delta\eta T}$=1, $\boldsymbol{\Delta\eta T}$=20 and $\boldsymbol{\Delta\eta T}$=30. The Rayleigh number is 7000 for T=0.5. The abbreviation 'Be89' stands for the results from (Bercovici et al., 1989), 'Ha98' from (Harder, 1998), 'Ra96' from (Ratcliff et al., 1996a), 'St06' from (Stemmer et al., 2006) and 'YK04' from(Yoshida and Kageyama, 2004). The respective discretization method is listed as well, where 'SP' denotes spectral, 'FE' finite elements, 'FD' finite differences and 'FV' finite volumes.

Table 4.3 shows a detailed comparison to other published models of convection with temperature-dependent viscosity contrasts of $\Delta\eta_T = 10$, $\Delta\eta_T = 20$ and $\Delta\eta_T = 30$, respectively, as an extension to the results published by Stemmer et al. (2006). In contrast to table 4.2, the grid was a projected icosahedra grid (see section 3.1.2) with 32 shells. The results agree within one percent to the results by Stemmer et al. (2006).

$Ra_{0.5}$	I.C.	$\Delta\eta_T$	t	n_{iter}	t_{CPU}	Nu_t	Nu_b	<T>	$T_{i,min}$	$T_{i,max}$	<V>	$V_{ri,min}$	$V_{ri,max}$
1e5	Cubic	1	0.688 [0.31]	2110 [35000]	35.85	7.873 [7.850]	7.890 [7.770]	0.1826 [0.1728]	0.0304 [0.0228]	0.8804 [0.9454]	154.64 [154.8]	-265.58 [-261.5]	979.28 [982.6]
1e5	Rand	1	0.748	1660	36.35	7.524 (7.371)	7.514 (7.372)	0.2493 (0.1941)	0.0306 (0.0271)	0.7970 (0.8973)	163.64 (153.13)	-396.70 (-275.65)	764.33 (949.34)
7000	Tetra	100	2.046 [2.0]	113 [30000]	3.33	2.909 [2.935]	2.920 [2.929]	0.2595 [0.2653]	0.0318 [0.0332]	0.9105 [0.9255]	23.13 [23.11]	-10.45 [-10.74]	166.59 [171.3]
7000	Tetra	1e3	1.001 [1.5]	201 [31000]	3.65	2.526 [2.546]	2.532 [2.535]	0.3027 [0.3124]	0.0662 [0.0695]	0.9292 [0.9452]	22.36 [22.90]	-6.40 [-6.97]	215.03 [226.7]

Table 4.4 shows a comparison of global and local quantities as well as compute time measurements for some selected cases. The sole influence on the initial condition (I.C.) in the first two cases demonstrates the volatile nature of these values. All computations took place on an 8 CPU shared memory machine (Opteron 875 w/ 2.2GHz), while t_{CPU} shows the compute time in hours until an adequate steady state was reached. This final time is shown as non-dimensional diffusion time t, combined with n_{Iter} time steps. The grid consisted in all computations of a projected icosahedron with 32 radial levels and 10.242 lateral nodes. Other values consist of volume averaged temperature <T> *and velocity* <V>*, as well as their interior (mid-shell) minima and maxima. The velocity minima and maxima are taken only from the radial component. Values in square brackets are from Zhong et al., 2008 and round brackets from Stemmer et al., 2006.*

A major advantage of the time discretization scheme used (section 3.2.7) is the robustness of the fully implicit treatment: instead of using the Courant-criterion which restricts the time step to the maximum velocity within the system, an approach utilizing the maximum difference of the velocity compared to the previous inner iteration leads to equally good results. Due to this restriction less turbulent convection models require less time steps and therefore computational time. Table 4.4 shows a more detailed comparison of local values such as radial min / max velocities and temperatures at mid-depth as discussed in the previous section. Furthermore, the computational effort for this kind of problems is also indicated. The table shows also the volatile nature of these control values as two different initial conditions are compared to each other (first two cases in table 4.4). An extension to this table can be found in Appendix B.

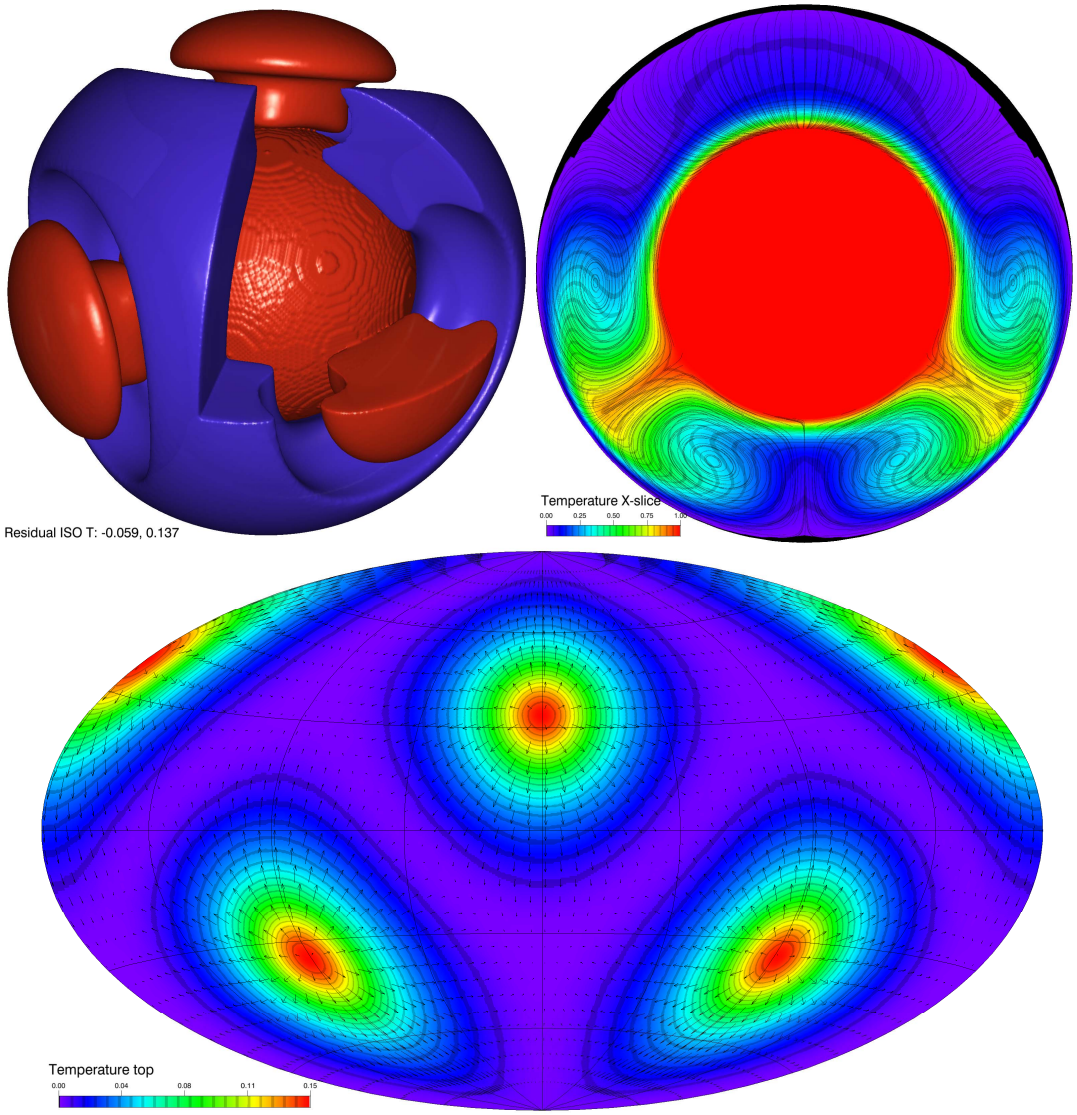

Figure 4.2 a) illustrates the flow pattern for a stimulated tetrahedral pattern with a Rayleigh number of 7000 at a reference temperature of 0.5. The overall viscosity contrast due to temperature is 20.

Figure 4.2a and b show detailed flow patterns and temperature distributions of the tetrahedral and cubical steady state patterns with low temperature-dependent viscosity ($\Delta\eta T$=20). Once $\Delta\eta T$ reaches a certain limit, the convective regime changes to stagnant-lid convection. This transition is smooth and occurs between contrasts of $\Delta\eta T$=10^4 and 5 10^5, as is further examined for three-dimensional spherical geometry by Stemmer et al. (2006) for bottom heated convection and in chapter 5 for purely internally heated convection. The method introduced here shows the same behavior for this viscosity contrast and also develops a stagnant-lid, as illustrated in figure 4.2 c. Figure 4.3 displays the typical plume-thinning phenomena caused by temperature-dependent viscosity (Hansen and Yuen, 1993, Ratcliff *et al.*, 1996b). If the viscosity contrast based on temperature is increased for a tetrahedral or cubical mode with moderate Rayleigh numbers, the plume-tail gets thinner and faster.

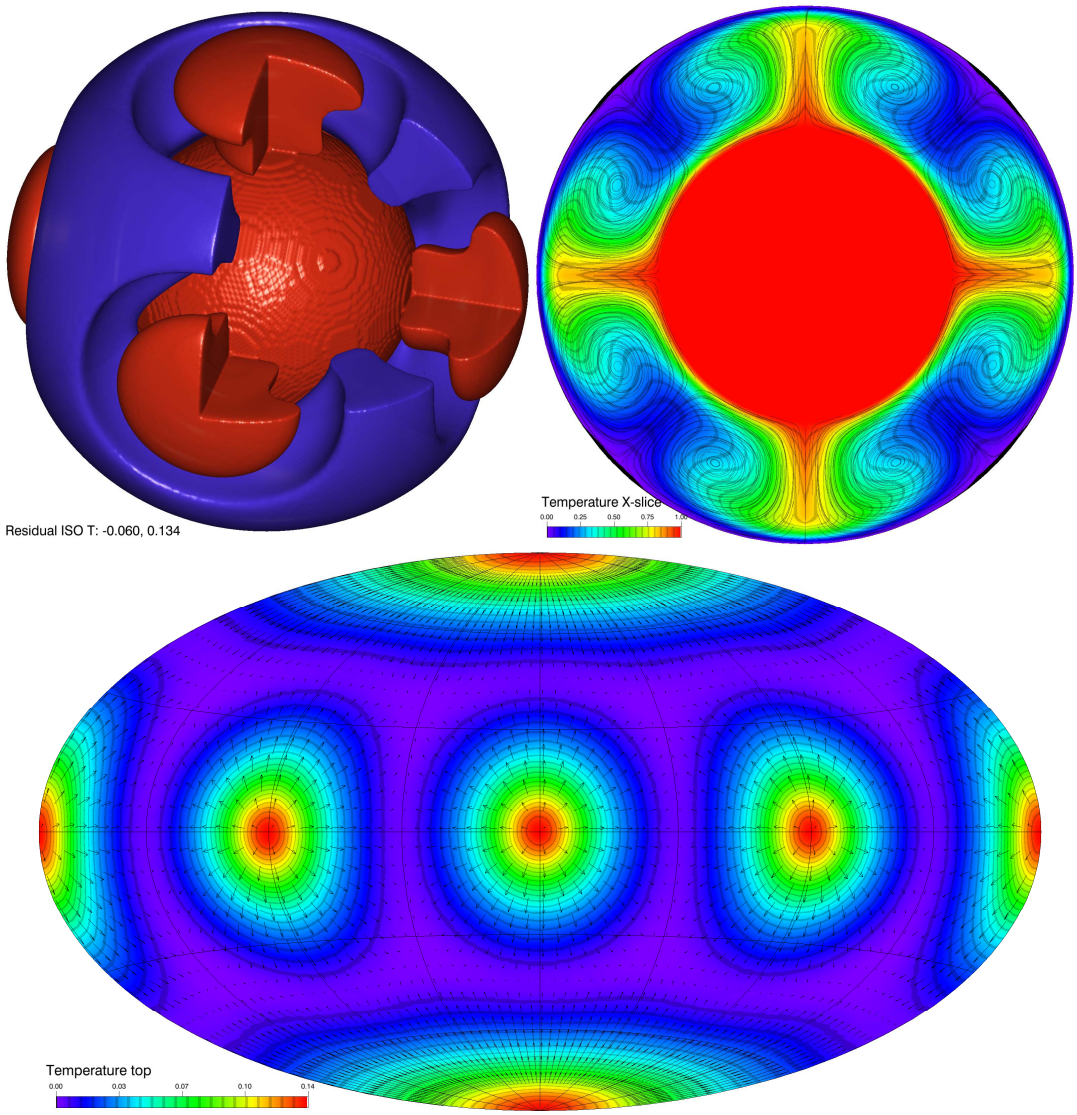

Figure 4.2 b) as a) but with a stimulated cubical pattern.

A final comparison to the commercial product COMSOL Multiphysics© 3.5 concludes this section. The COMSOL suite (Courbebaisse, 2008) solves the equations for mantle convection with spatially varying viscosity using a finite element approach. Because this product has a broad range of applications, the solver is not optimized for this kind of problems. This is the reason why only two-dimensional (2D) cases could be compared. Two simple test cases were constructed in 2D, one bottom-heated isoviscous model with $Ra = 10^5$ and a second model with an intermediate viscosity contrast of $\Delta\eta_T = 100$. The grid constructed for this problem is setup by 325 constantly angular divided nodes projected on 32 linearly distributed radial shells (radius ratio 0.55), while in COMSOL the mesh generated for the finite-element discretization is completely unstructured. The top boundary condition for the momentum equation was changed to a no-slip condition to suppress unrealistic zero-mode velocity patterns from appearing in COMSOL. The initial condition for the conductive temperature profile was slightly

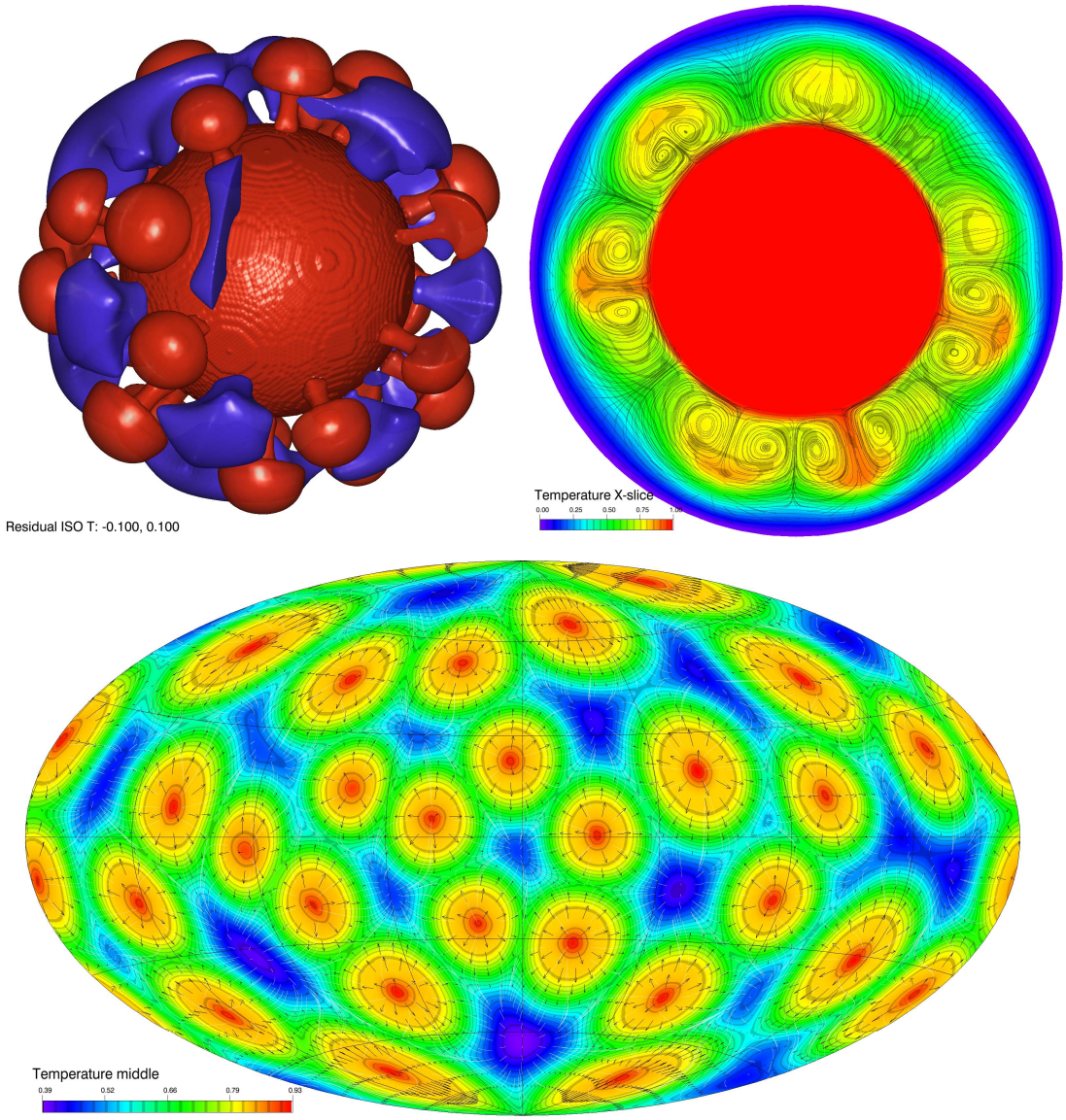

Figure 4.2 c) as a) but with a viscosity contrast of 10^6. *A stagnant-lid formed and the convecting layer exhibits high degrees, independent of the initial perturbation.*

perturbed with a wavelength of $1/4^{th}$ to force four upwellings. The results are shown in table 4.5, together with the steady-state pattern of temperature and velocity in figure 4.4. Global and local values of both cases agree well within two percent.

Setup	Simulation	Resolution	Nu_b	Nu_t	$\langle T \rangle$	v_{rms}	v_{max}
$Ra = 10^5$	COMSOL 3.5	23.500	5.71	5.65	0.535	92.41	255.02
Isoviscous	This	10.400	5.63	5.69	0.531	105.3	256.21
$Ra_1 = 10^5$	COMSOL 3.5	28.400	2.69	2.68	0.581	24.23	73.93
$\Delta\eta_T = 100$	This	10.400	2.65	2.68	0.565	28.68	73.05

Table 4.5 shows a comparison of two cases of purely bottom heated convection in a 2D spherical shell with the commercial product COMSOL 3.5. The top boundary condition for the momentum equation was, in contrast to the previous benchmarks, no-slip. For the weakly temperature-dependent viscosity case, the reference temperature for the Rayleigh number was 1 instead of the previously used 0.5.

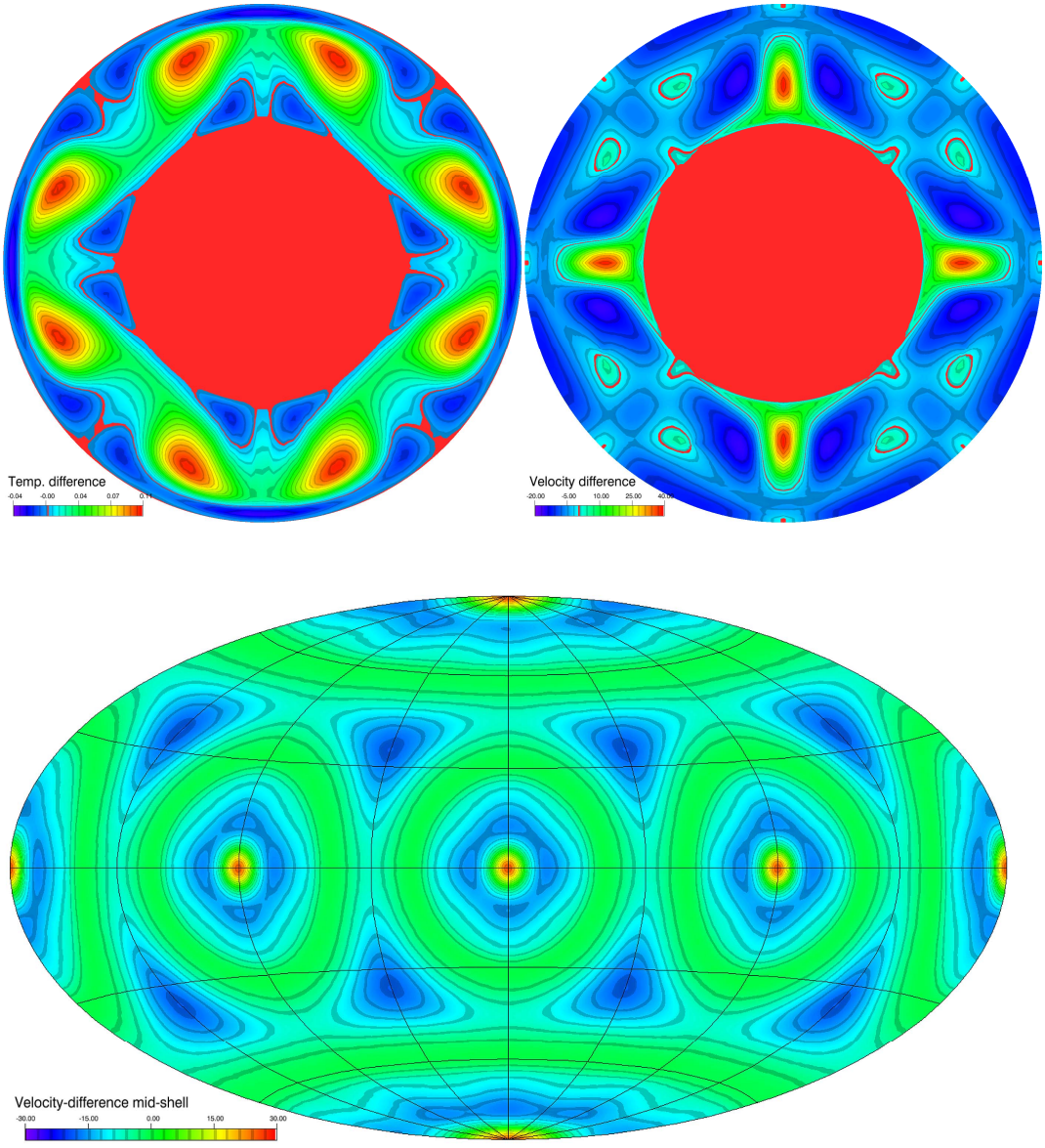

Figure 4.3. The difference between a weakly temperature-dependent case ($\Delta\eta_T = 20$) with $Ra_{0.5}$=7000 and the isoviscous case. Because the upper two slice views are not color-centered around zero, they contain an extra red contour line that indicates zero difference.

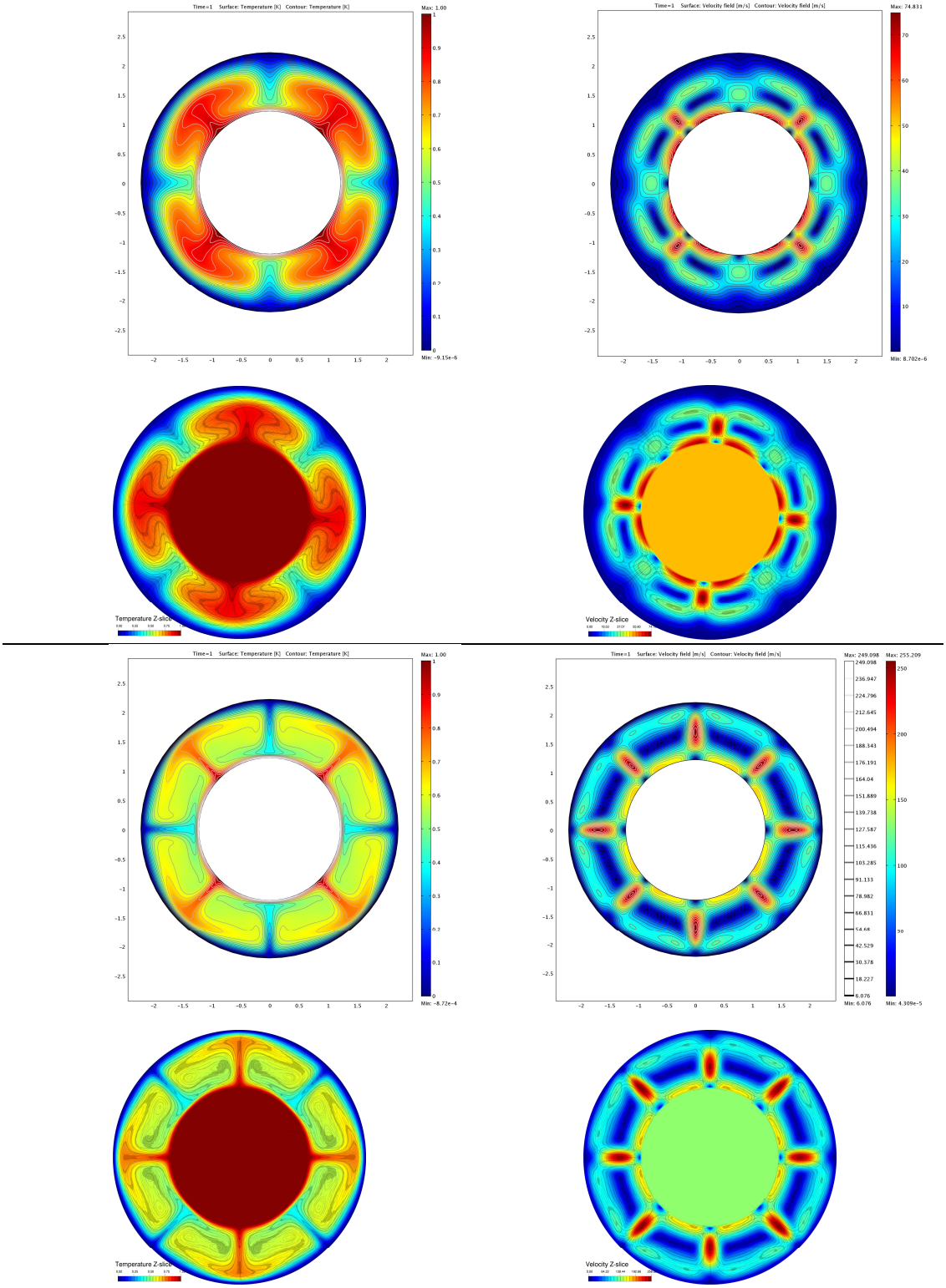

Figure 4.4. The temperature and velocity field of the cases summarized in table 4.5, while the upper four images show the case with temperature-dependent viscosity and the lower four images the isoviscous case. The respective upper two pictures are directly processed with COMSOL 3.5 and the lower cases are the result of the presented simulation method with similar color scale.

5 Influence of Variable Viscosity on Purely Internally Heated Convection

This chapter concludes this thesis with a systematic study of the influence of temperature- and pressure-dependent viscosity on thermal convection in a spherical shell. A total of 88 simulations for volumetrically heated convection were analyzed to study for instance the different convection regimes, the behavior of the transition to the stagnant-lid regime and key variables of stagnant-lid convection itself like lid thickness, boundary layer thickness and structural complexity. The runs are divided into purely temperature-dependent viscosity cases (TC) and temperature and depth dependent viscosity cases (TPC). Roughly 2/3rd of all runs are TC, while the residues include a constant pressure-dependent viscosity contrast of 100. Viscosity contrasts reach values of up to 10^9 and the internal Rayleigh number values of around 10^8, which leads to updated scaling laws for this kind of convection and a newly introduced spectral scaling that might help to constrain interior parameters of convection. The input and output parameters are summarized in appendix A and C. The following list summarizes all symbols used in this chapter:

H	Volumetric heat production rate	α	Fitting parameter, prefactor
M	Mobility criterion after Tackley	β	Fitting parameter, exponent
M_0	Average temporal deviation of v_{max}	γ	Rheological gradient
M_1	Mobility criterion based on boundary layer thickness	δ_0	Depth of the center of the thermal boundary layer (TBL)
S	Mobility criterion after Solomatov	δ_b	Depth of the bottom of the TBL
T	Temperature, non-dimensionalized	δ_l	Depth / thickness of the stagnant-lid
T_i	Interior temperature	δ_{rh}	Thickness of the TBL, $\delta_l - \delta_b$
T_1	Rescaled isoviscous temperature	δ_{rh}^*	Reduced thickness of the TBL, centered around δ_0
T_C	Maximal conductive temperature	ζ	Fitting parameter
T_L	Temperature below the stagnant-lid	η	Non-dimensional viscosity
T_S	Surface Temperature	η_i	Non-dimensional viscosity of the convecting interior
a	Fitting parameter, prefactor	θ	Frank-Kamenetskii-parameter
a_{rh}	Rheology constant	υ	Viscosity in Pa s
d	Depth	υ_S	Surface viscosity in Pa s
g	Gravity	ρ	Density
k	Conductivity	ω	Weighted mode
m	Slope for wavelength scaling	ω_{min}	Minimal mode / degree
q	Heat-flow	ω_{step}	Increase of degree for time-dependent convection
q_a	Convective heat-flow	ϵ	Fitting parameter
q_c	Conductive heat-flow	ΔT_{rh}	Temperature difference from δ_l to δ_b
q_f	Convective heat-flow fraction	$\Delta\eta_P$	Viscosity contrast due to pressure
r_i	Inner radius	Nu	Nusselt number
r_o	Outer radius	Ra_1	Rescaled isoviscous Rayleigh number Ra
r_r	Radius ratio	$Ra_{H,0}$	Surface Ra for internally heated convection
t	Time	$Ra_{H,i}$	Internal Ra number based on the viscosity of T_i
v_{rms}	Volume averaged root-mean-square velocity	Ra_{S-T}	Ra of the transition between steady-state and time-dependent convection
v_{top}	Surface velocity	Ra_δ	Boundary layer Ra

5.1 Model Setup

We consider thermal convection of an internally heated Boussinesq fluid at infinite Prandtl number. The Boussinesq approximation is sufficiently accurate for mantle convection (Spiegel and Veronis, 1960) and due to relatively slow velocities (up to meters per year) all inertia forces can be neglected with an infinite Prandtl number, as further explained in section 2.3. The inner and outer boundaries of the spherical shell are impermeable and shear-stress free. The inner to outer radius ratio $\frac{r_i}{r_o} = r_r = 0.55$, similar to Earth-like studies of mantle convection. The temperature at the top is fixed (cooled from above) and, in contrast to benchmarks and the setup explained in section 2.2, the inner boundary is insulated.

The equations are in a non-dimensional form so that the thickness $d = r_o - r_i$ of the spherical shell acts as a length scale, the thermal diffusion time $t = \frac{d^2}{\kappa}$ as time scale where $\kappa = \frac{k}{\rho c_P}$ is the thermal diffusivity, k the thermal conductivity and c_P the specific heat capacity at constant pressure. The temperature scale for this kind of convection is based on the internal heating rate H instead of a fixed ΔT. The non-dimensional temperature T', with T_S as surface temperature, is given as (Grasset and Parmentier, 1998):

$$T = \frac{\rho H d^2}{k} \cdot T' + T_S \tag{5.1}$$

For convenience, the apostrophe is neglected in the following sections and all temperatures are non-dimensional.

The bottom-isolation is expressed with a Neumann boundary condition for temperature (equation 3.39 in chapter 3.5) and the maximal possible temperature is limited by T_C as explained in chapter 4.1. The energy equation (2.16) changes with the temperature scale of equation 5.1 to:

$$\frac{\partial T'}{\partial t} = \nabla^2 T' - \vec{v} \cdot \nabla T' + 1 \tag{5.2}$$

All available energy of the system comes from a homogeneous heat source, similar to radiogenic heating. Thus, the strength of convection can be expressed by the internally heated Rayleigh number, following the definition of Reese *et al.* (1999a),

$$Ra_{H,0} = \frac{\rho^2 g \alpha H d^5}{\kappa k \upsilon_S}, \tag{5.3}$$

where the volumetric heat production rate H, the density ρ, the acceleration of gravity g, the thermal diffusivity κ, the coefficient of thermal expansion α, the surface viscosity υ_S (the reference temperature equals the surface temperature) and the thermal conductivity k are assumed to be constant.

A different expression exists for the effective Rayleigh number that is best described with the viscosity at the convecting interior $\eta_i = \min(\langle\eta\rangle_{lat})$. Note that η is always the non-dimensionalized viscosity and related to the dynamic viscosity (Pa s) with $\eta = \upsilon/\upsilon_S$, therefore the internal viscosity is defined as $\upsilon_i = \eta_i\,\upsilon_S$ and the effective Rayleigh number is:

$$Ra_{H,i} = \frac{\rho^2 g \alpha H d^5}{\kappa k \upsilon_i} = Ra_{H,0}\eta_i \tag{5.4}$$

Because the interior temperature T_i (see section 4.1 for definition) is not known a-priori, this Rayleigh number is an output parameter, while $Ra_{H,0}$ is suitable as an input parameter for the simulation as a constant. For isoviscous convection the Rayleigh number is therefore constant in space.

While this work focuses on the influence of temperature on viscosity, selected tests were made that study the influence of pressure dependence as well. For simplicity and comparability, Newtonian viscosity is assumed, linearized with the Frank-Kamenetskii approximation (Frank-Kamenetskii, 1969):

$$\eta = \exp\left(-\gamma\, T' + \ln(\Delta\eta_P)\,(r_o - r)\right) \tag{5.5}$$

The γ parameter is assumed constant and represents the rheological gradient $\gamma = -\partial \ln\eta/\partial T$. It is related to the original Arrhenius relation (Karato and Wu, 1993) with $\gamma = E/(R\,T_i^2)$. A pressure-dependent viscosity is approximated with a linear depth dependent gradient and is determined by the parameter $\Delta\eta_P$ that describes the maximal viscosity contrast due to depth, similar to the viscosity definition in section 2.5.

The viscosity contrast in a convecting system is mainly described by the rheological constant γ and the resulting temperature difference in the system. Because of purely internally heated convection, this difference is not known a-priori and therefore the viscosity contrast itself is an output parameter, in contrast to bottom heated convection. Here the temperature difference and γ are input parameters and therefore $\Delta\eta = \exp(\gamma)$. In the present simulations, $\Delta\eta = \exp(\gamma\, T_i)$ is valid for TC only. For TPC, the definition of T_i is not sufficient because the effect of pressure dependency does not reveal the depth of the lowest average viscosity. Therefore, the lowest observed radially averaged viscosity ($\Delta\eta = \min(\langle\eta\rangle_{lat})^{-1}$) is taken for those cases. The viscosity contrast due to pressure $\Delta\eta_P$ is therefore approximated as a depth dependent viscosity (Bunge *et al.*, 1996). In contrast to temperature-dependent viscosity, depth dependent viscosity weakens the overall viscosity contrast because viscosity increases with depth but decreases with temperature.

The projected icosahedra grid with 32 constantly spaced shells, each containing 10,242 nodes (see figure 3.5 in section 3.1.2), acts as a discrete basis for all simulations. This grid type was the preferred choice for this kind of simulations because higher lateral resolution is usually required at the hotter interior.

5.2 Regime Classification

The convection pattern and its temporal evolution changes with increasing Rayleigh number or viscosity contrast. Two different regime categories are distinguished. One classifies the temporal evolution and differentiates between steady-state convection and time-dependent / turbulent convection and is called **temporal regimes**. The central parameter of influence is the Rayleigh number. Another regime category distinguishes the spatial properties of the flow such as structure and surface mobility. The latter is influenced mainly by viscosity contrast and the applied rheology and is called **rheological regimes**.

5.2.1 Rheological Regimes

Classification Criteria

The rheology law significantly influences the convection pattern and heat transport. Especially the viscosity contrast due to temperature $\Delta\eta$ has a great impact on the convection. Depending on the viscosity contrast, the surface mobility changes and is denominated into three different regimes (e.g., Hansen and Yuen, 1993, Solomatov, 1995, Ratcliff *et al.*, 1996a, Trompert and Hansen, 1998a, Tackley, 2000a):

1. The **mobile regime** is typical for isoviscous convection and convection with extremely low viscosity contrasts where the surface is fully mobilized. In case the upper and lower boundaries are free-slip, the velocity is almost equal on the inner and outer boundary. A moderate velocity decrease on the surface is expected due to the geometry of the spherical shell: the inner area is smaller than the outer area.
2.
    a. The **sluggish regime**, sometimes called transitional regime, is typical for convection with moderate viscosity contrasts for dominantly bottom heated or boxed simulations. The surface is almost stagnant due to high viscosities from the cold material close to the surface. The velocity at the surface is significantly smaller than at the inner boundary.
    b. The **low-degree regime** occurs especially with dominant internally heated convection in spherical shells. In different circumstances this regime extends or replaces the sluggish regime. With moderate viscosity contrasts, instead of a reduced surface velocity, the pattern of convection changes to long wavelengths with a fully mobilized surface.
3. The **stagnant-lid regime** occurs with strong temperature-dependent viscosity as the surface completely stagnates and does not participate in convection anymore. The heat transport within this lid is only by conduction.

Different criteria are needed to distinguish these regimes. Typical approaches involve the averaged surface velocity v_{top} (e.g., Hansen and Yuen, 1993, Davaille and Jaupart, 1993, Solomatov, 1995, Trompert and Hansen, 1998b, Tackley, 2000b). However, no definite value of v_{top} can be determined to classify a boundary to the stagnant-lid as shown in figure 5.1, which illustrates the variations of the volume-averaged velocity v_{rms} together with v_{top}.

Although the boundary layer thickness δ_{rh} (as explained in the next section) does not correlate with T_i and therefore the Nusselt number Nu in the stagnant-lid regime, a well defined correlation exist naturally from the definition of the Nusselt number and heat flux for the mobile regime in the form of $\delta_{rh} = Nu^{-1}$ (Solomatov, 1993; section 5.3). This different correlations of the boundary layer thickness in relation to the Nusselt number gave rise to an alternative mobility criterion in the form of $M_1 = \delta_{rh}\, Nu$, as it defines a well working boundary for the stagnant-lid regime with $M_1 < 0.6$. The advantage of this criterion is the absence of any velocity component, which makes it suitable for using it with scaling laws. Figure 5.2 demonstrates three different criteria derived from Solomatov and Moresi (1997) and Tackley (2000b) as well as the just presented M_1 for all cases.

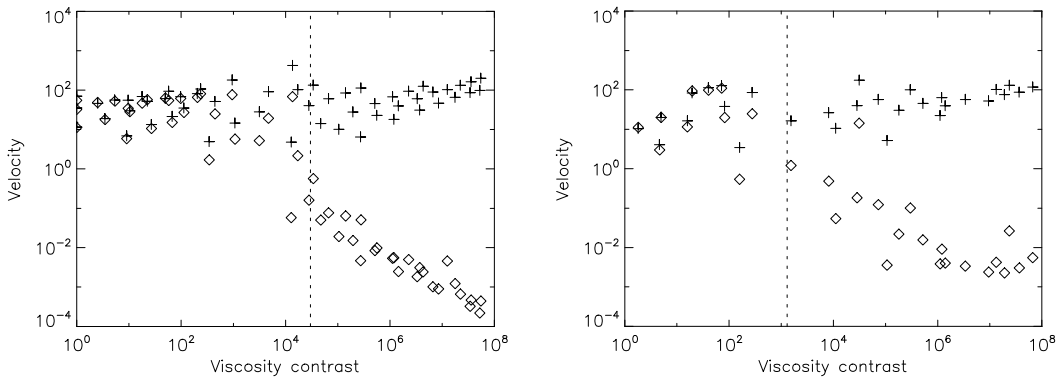

Figure 5.1. The rms velocity as crosses and the surface velocity as diamonds to the respective viscosity contrast of each temperature-dependent case on the left and temperature- and pressure-dependent on the right. The dashed line represents the suggested boundary between the stagnant-lid and mobile regime.

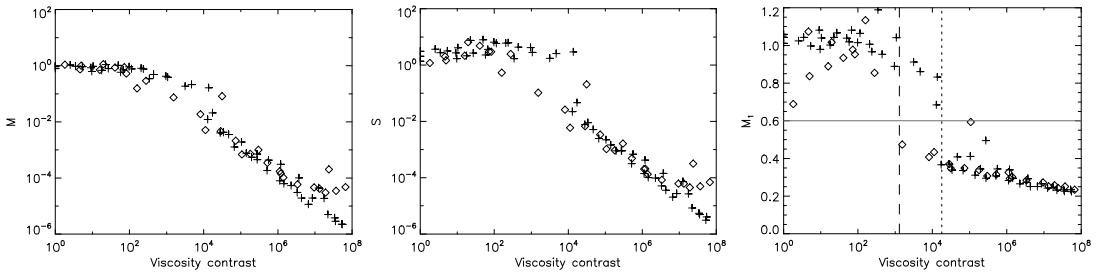

Figure 5.2. Different mobility criterions; Left shows the proposed criterion by Tackley (2000b) with $M = v_{top}/v_{rms}$*; the middle picture shows the criterion by Solomatov and Moresi (1997) with* $S = \left(\delta_{rh}^2\, v_{top}\right)/\kappa d$ *; the right picture shows the criterion used in this work with* $M_1 = \delta_{rh}\, Nu$*. All three pictures show all 88 cases with crosses as purely temperature-dependent viscosity cases (TC) and diamonds with temperature- and pressure-dependent viscosity cases (TPC). The dashed vertical lines in the right picture show the boundary between the stagnant-lid regime (right-hand side for increased viscosity contrast) and non-stagnant-lid, dashed for TPC and dotted for TC.*

The Mobile Regime

This regime is characterized by a fully mobilized surface and, to distinguish it from the low-degree regime, with a minimal dominant degree of three. It thus includes isoviscous convection and convection with low viscosity contrasts up to 10. The absence of degree-one convection in isoviscous cases is due to the chosen radius ratio since an increasing radius ratio leads to higher minimal degrees for convection (Jarvis, 1993, Jarvis, 1994, Jarvis *et al.*, 1995, Travnikov *et al.*, 2000). An increase in the surface Rayleigh number does generally increase the mode, although no tendency could be observed for increased internal Rayleigh numbers with increasing γ, as visible in figure 5.3. The velocity increases and the flow patterns become turbulent while maintaining a relatively low dominant mode.

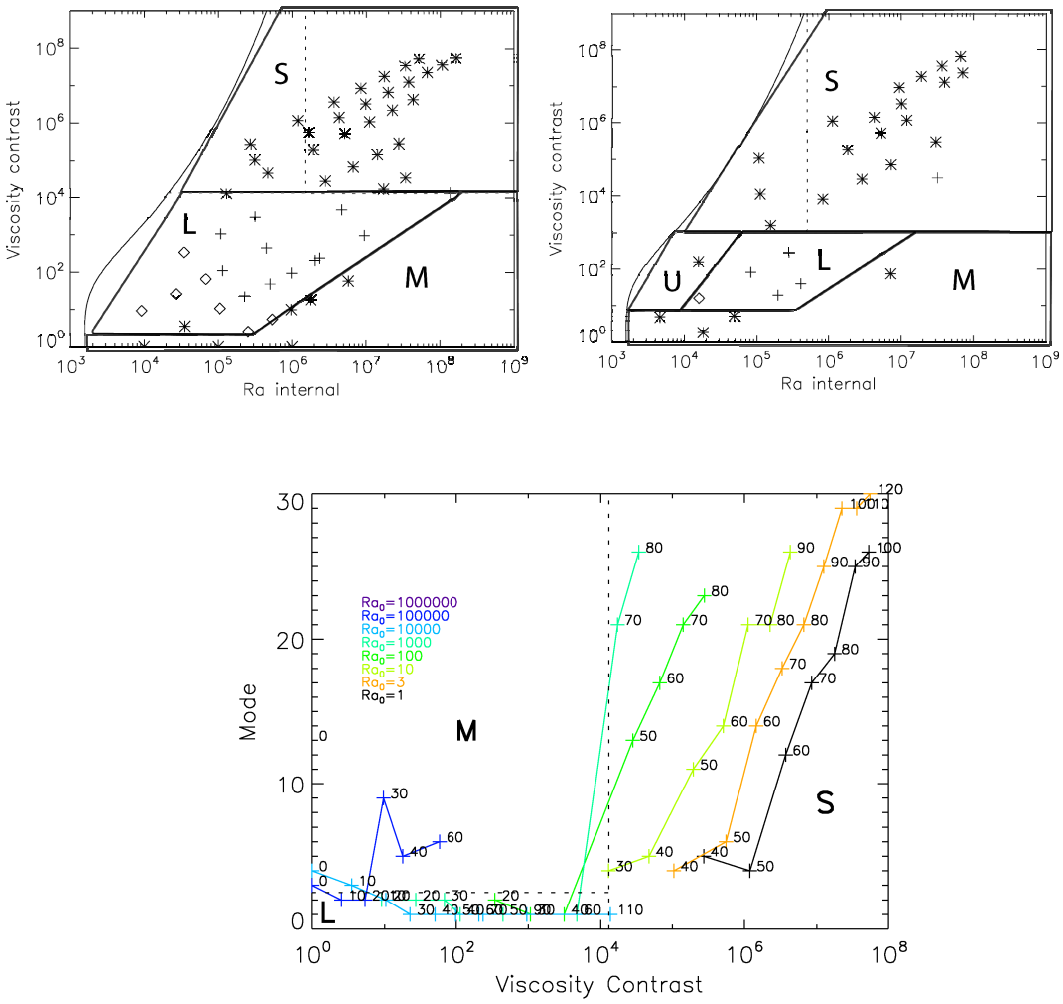

Figure 5.3. The upper two figures show the position of the different regimes in the $Ra_{H,i}$ and $\Delta\eta$ parameter space. M stands for mobile regime, L for low-degree regime, S for stagnant-lid regime and U for sluggish regime.The lower figure shows all TC in the $\Delta\eta$ and dominant mode parameter space, with γ as labels for each case and connected cases with similar $Ra_{H,0}$.

The Low-Degree Regime

In either TC or TPC scenarios, starting from isoviscous convection, an increase in the viscosity contrast leads to a drop in the dominant mode for $Ra_{H,0} < 1e5$ and increases rather abruptly while passing the stagnant-lid boundary. A significant difference to other publications in this parametrical range is the absence of the sluggish regime for TC and a narrow range of the sluggish regime for TPC. This regime should occur after Christensen (1984b) for a viscosity contrast between 1e2 and 1e4. It is further confirmed from other studies in 2D and 3D boxed simulations with internal heating and / or bottom heating (e.g., Carey and Mollendorf, 1980, Ogawa *et al.*, 1990, Hansen and Yuen, 1993, Hirayama and Takaki, 1993). This study is the first to simulate mantle convection with purely internal heating in the assumed parametrical range of the sluggish regime in a spherical shell. Instead of weakly moving upper material, complete low-

degree (less than degree three as dominant mode) convection could be observed. In the $Ra_{H,i}$ and $\Delta\eta$ parameter space, this region has the shape of a trapezoid and therefore depends on both parameters, as illustrated in figure 5.3 with a degree-marker over the observed parameter space.

Tackley (1993) observed long wavelengths caused by bottom heated convection in a 3D box and ascribed it to the influence of the boundary condition. He argued that with the more realistic free-slip boundary condition the flow would choose a preferably long wavelength in this scenario. The transition of the boundary condition from free-slip in the mobile / low-degree regime to the no-slip boundary condition of the stagnant-lid regime for the convecting interior is most probably the cause for the nonexistent low-degree cases in the stagnant-lid regime and is responsible for the minimal mode studied in section 5.7.

The Stagnant-Lid Regime

The transition into the stagnant-lid regime from the low-degree regime is rather sharp: the surface velocity drops and the ratio of lateral to radial viscosity contrast decreases suddenly, along with an increase in the dominant mode as shown in figure 5.4. The stagnant-lid regime is observed for a viscosity contrast larger than 1.3e4 within the convecting system for purely temperature-dependent viscosity cases. The relative error on this value is less than 5% because the transition is valid for all considered parameter values.

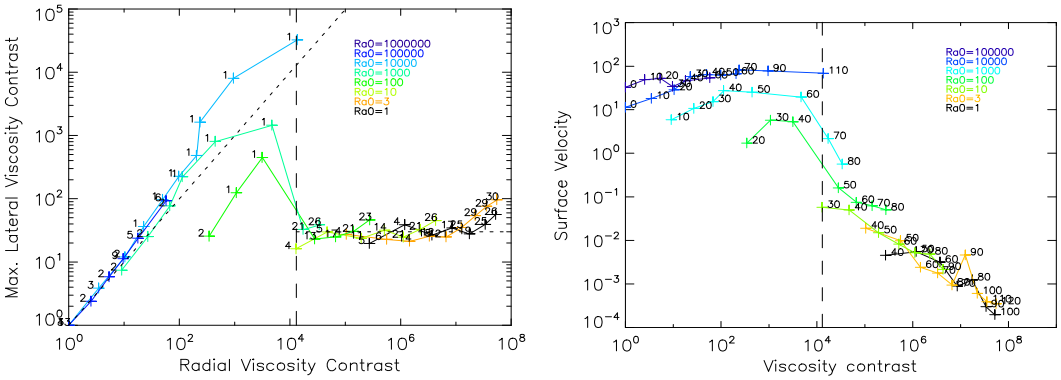

Figure 5.4. The left figure shows the relation between the lateral and radial viscosity contrast (commonly just referred to as viscosity contrast) for all purely temperature-dependent viscosity cases (TC). The numbers along the line show the dominant mode. On the right figure the logarithm of the average surface velocity is plotted against the viscosity contrast with numbers along the line that mark the γ value of the simulation. The lines connect a series of simulations for a specific $Ra_{H,0}$ and a varied γ. The figure illustrates the behavior of the lateral viscosity contrast and the average surface velocity at the transition into the stagnant-lid regime, which is marked with a vertical dashed line for all simulated cases with purely temperature-dependent viscosity. The average lateral viscosity contrast of the stagnant-lid cases is 30 (dotted horizontal line, left figure).

5.2.2 Temporal Regimes

To achieve convection for a given viscosity contrast, the Rayleigh number must be larger than a critical value. For Rayleigh numbers just above the critical value, convection sets in and reaches a steady-state in which the convection pattern stays stationary. With increasing Rayleigh number a turbulent time-dependent convection sets in where all measurable output parameter fluctuate over time (e.g., Krishnamurti, 1970, Busse, 1978, Hansen and Ebel, 1984, Hansen and Ebel, 1988, Hansen and Yuen, 1990, Hansen *et al.*, 1990, Travis *et al.*, 1990, Hansen *et al.*, 1992a, Hansen *et al.*, 1992b, Bottaro *et al.*, 1992, Hansen and Yuen, 1993, Tang and Tsang, 1997, Craik, 2000). If the output parameters are independent of the initial condition and fluctuate around their temporally averaged value, it is called the quasi-steady-state.

In contrast to the spatial regimes (rheology dependent, e.g., mobile and stagnant-lid regime), the time-dependent regimes depend mostly on the internal Rayleigh number as it determines the vigor of convection. Between the steady-state (not time-dependent) and the turbulent time-dependent regime, a cyclic regime with periodically reoccurring patterns exists.

In a narrow range of $Ra_{H,i}$, the pattern of convection undergoes a cyclic behavior (e.g., Zhong *et al.*, 2007). This behavior was visible in only 2 cases and show typical effects of mode-alteration at fixed intervals. Figure 5.6 displays the temporal spectral progression of the temperature and velocity field of one case, cycling between degree-one and two. Because of the limited amount of cases no definite boundaries for the cyclic regime could be established and all observed cycles do not have a period short enough to be considered in planetary evolution models.

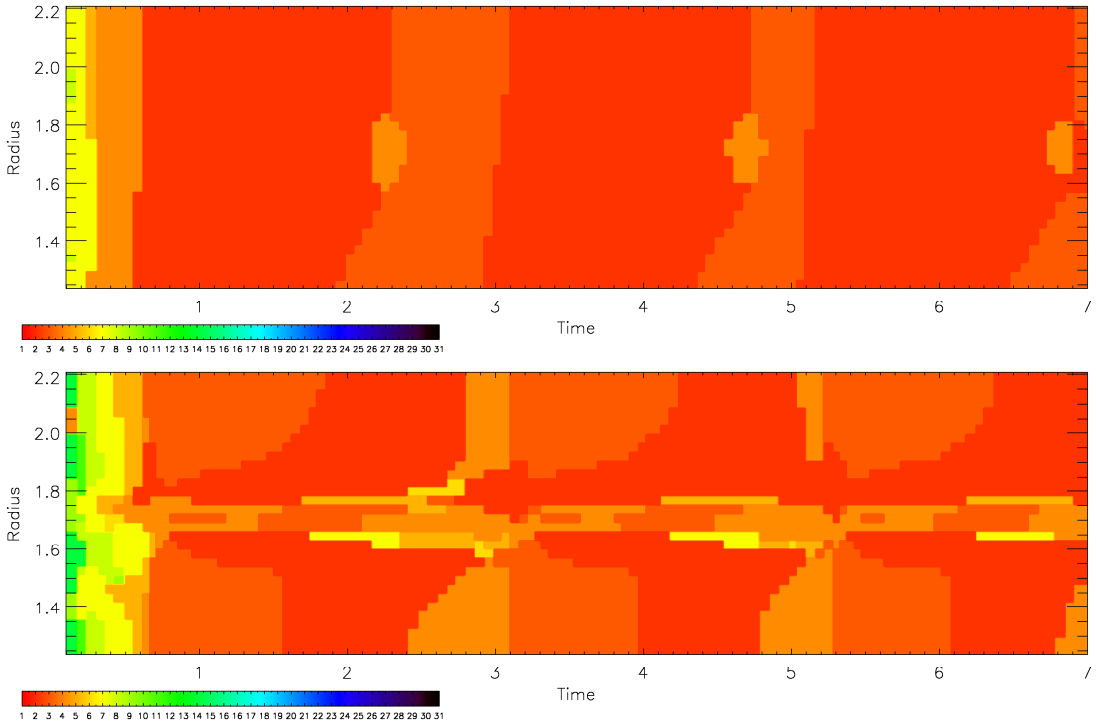

Figure 5.5. The cyclic behavior of the case $Ra_{H,0} = 1e3$ *and* $\gamma = 30$ *between a dominant degree one and two. The color scale indicates the mode at a certain radius and time for temperature (top) and velocity (bottom).*

To classify the time dependence of convection, a criterion is required that is sensible to temporal fluctuations of control variables, i.e. the maximal velocity v_{max}. The quasi-steady state part of a simulation was used to calculate the mean maximal velocity $\bar{v}_{max}$ and finally the M_0 indicator that determines the standard deviation σ of v_{max} relative to $\bar{v}_{max}$: $M_0 = \sigma(\frac{\bar{v}_{max}}{v_{max}})$. This is equivalent to the average percental fluctuation of v_{max}. Convection with a value of M_0 smaller than 1.5% is considered as steady state convection and a value greater than 1.5% is given for time-dependent convection. This value is chosen to avoid numerical errors. A sharp boundary for the transition to time-dependent convection could only be identified for stagnant-lid cases and is ~2e6 for TC and ~6e5 for TPC, similar to observations by Hansen *et al.* (1990) and as illustrated in figure 5.7. The boundary for non stagnant-lid cases is rather wide and between 1e5 and 2e6 for all cases.

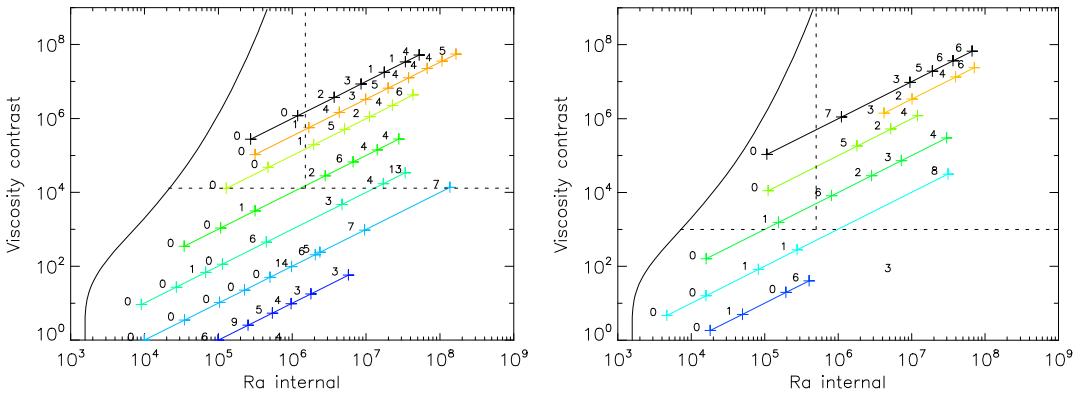

Figure 5.6. The M_0 indicator for the time dependence of convection, illustrated as rounded integers over all TC on the left and TPC on the right, where connected lines illustrate constant $Ra_{H,0}$, the horizontal dashed line the boundary to the stagnant-lid regime and the vertical line the boundary to time-dependent convection in the stagnant regime.

5.2.3 Influence of Pressure Dependence

For the pressure-dependent cases, a narrow sluggish regime can be observed and the low-degree (below degree three) range is rather narrow compared to the purely temperature-dependent cases as shown in figure 5.3, right. The pressure dependence reduces the effective viscosity at the bottom which also leads to a reduction of the local Rayleigh number at greater depths. In contrast to bottom heated convection the bottom free-slip boundary therefore changes towards a no-slip boundary that can also be interpreted as reducing the size of the effective convecting part. This on the other hand hinders low degrees from developing. The transition into the stagnant-lid starts at a viscosity contrast of about 1e3. Interesting to note, in contrast to bottom-heated convection where the viscosity contrast required to enter the stagnant-lid regime is higher for pressure dependence in comparison to purely temperature-dependent viscosity, it is reduced for purely internally heated convection. There are also hints that the transition into the stagnant-lid regime is not purely viscosity contrast dependent. One case shows a transition to degree one without a lid while maintaining high viscosity contrasts as figure 5.7 (cyan dotted line) displays.

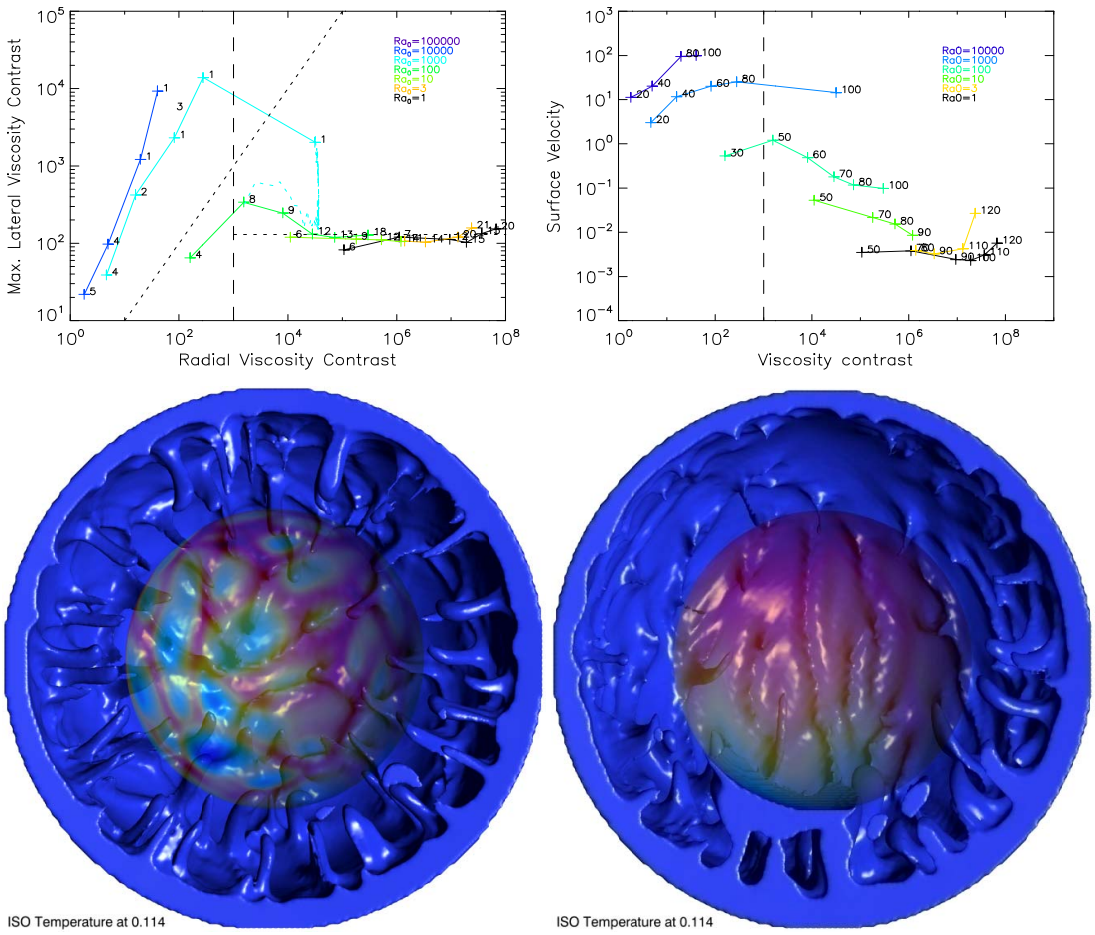

Figure 5.7. The left upper figure shows the relation between the lateral and radial viscosity contrast for cases with an additional pressure dependence of $\Delta\eta_P = 100$ (TPC). The numbers along the line show the dominant mode. On the right upper figure the logarithm of the average surface velocity is plotted against the viscosity contrast with numbers along the line that mark the γ value of the simulation. The lines connect a series of simulations for a specific $Ra_{H,0}$ and a varied γ. The vertical dashed line indicates the beginning of a transitional zone while the transition to the stagnant-lid regime might not only be dependent on the viscosity contrast. The average lateral viscosity contrast of the stagnant-lid cases is 130 (dotted horizontal line, left figure). The dotted cyan line marks the evolution of the simulation with $Ra_{H,0} = 1e3$ and γ=100, also displayed at the two lower pictures as iso-surface; the two snapshots are taken at $t = 0.35$(left) and $t = 0.6$ (right). The regime changed from a dominant degree 22 with a thin lid (5%) to a degree one with no lid.

Cyclic behavior between different regimes could not be observed, but as periods are preferably long, this lag of observation could be due to insufficient runtime of the simulations.

5.2.4 Lateral Viscosity Contrast

The lateral to radial viscosity ratio differs between the purely temperature-dependent cases and the pressure-dependent cases (figure 5.4 and 5.7). For non-stagnant-lid cases with purely temperature-dependent viscosity, this ratio is approximately direct proportional for asymptotically large $Ra_{H,0}$ ($\Delta\eta_{lat} \sim \Delta\eta$). Instead, a disproportionate increase of $\Delta\eta_{lat} \sim 3\Delta\eta^2$ occurs for pressure-dependent cases (figure 5.7).

For all stagnant-lid cases $\Delta\eta_{lat}$ stays approximately constant. For TC this value is at around 30 and for pressure ($\Delta\eta_P = 100$) and temperature dependency it raises to 130. This increase is therefore only dependent of the pressure dependence of the viscosity $\Delta\eta_P$. This assumption has been verified with three extra stagnant-lid cases with $\Delta\eta_P = 1e5$ (cases 86-88 in appendix A and C) that led to an average $\Delta\eta_{lat} = 3e3$. With a linear fit the following relationship can be established:

$$\Delta\eta_{lat} \approx \exp(2.95 + 0.43 \ln \Delta\eta_P) \tag{5.6}$$

5.3 Boundary Layer Definition

The thermal boundary layer (TBL) of a convecting system is the region where a transition between convective and conductive heat-flow can be observed. In purely internally heated cases with an insulated bottom boundary, only one TBL exists. Note that figure 5.8 and 5.9 in combination with the symbol index at the beginning of this chapter are important to understand the following sections.

To establish scaling laws for the TBL thickness δ_{rh}, a definition for the lower boundary of the TBL, δ_b, must be established. Two common methods of determining the depth of the lower boundary are found in literature. Deschamps and Sotin (2000) and Davaille and Jaupart (1993) used the method of the tangent through the inflexion point of the heat-flow. The depth at which this tangent crosses zero is used as the lower boundary layer δ_b since only convective heat-flow is considered from this point on. This depth corresponds to the depth at which $T(\delta_b) = T_i$. An alternative way as used in Grasset and Parmentier (1998) is to take the point where the advective heat-flow equals the conductive heat-flow, δ_0. Assuming δ_b defined as δ_0 would usually underestimate the boundary layer thickness and does not represent the rheological temperature scale ΔT_{rh} as illustrated in figure 5.8 and further discussed in the next section. The depth where the advective heat-flow equals the conductive heat-flow corresponds more to a depth of the center of the boundary layer. The layer thicknesses obtained with the first method correspond with an error of less than 2% to the values obtained by Parmentier *et al.* (1994). These studies used isoviscous 3D boxed simulations of internally heated convection and confirm again that convection beneath the stagnant-lid can be treated as isoviscous even though small lateral and radial viscosity contrasts exist (e.g., Grasset and Parmentier, 1998, Solomatov and Moresi, 2000b, Reese *et al.*, 2005). The stagnant-lid depth δ_l that reaches zero in case of an absent stagnant-lid acts as upper bound for the boundary layer so that $\delta_{rh} = \delta_b - \delta_l$. The lid thickness δ_l and its determination are further discussed in the following section. The reduced boundary layer thickness δ_{rh}^* plays an important role in the scaling laws and is centered around δ_0: $\delta_{rh}^* = 2(\delta_b - \delta_0)$. This is similar to the intersection of the tangent through the inflexion point of the conductive heat-flow fraction with one, minus the root of this tangent.

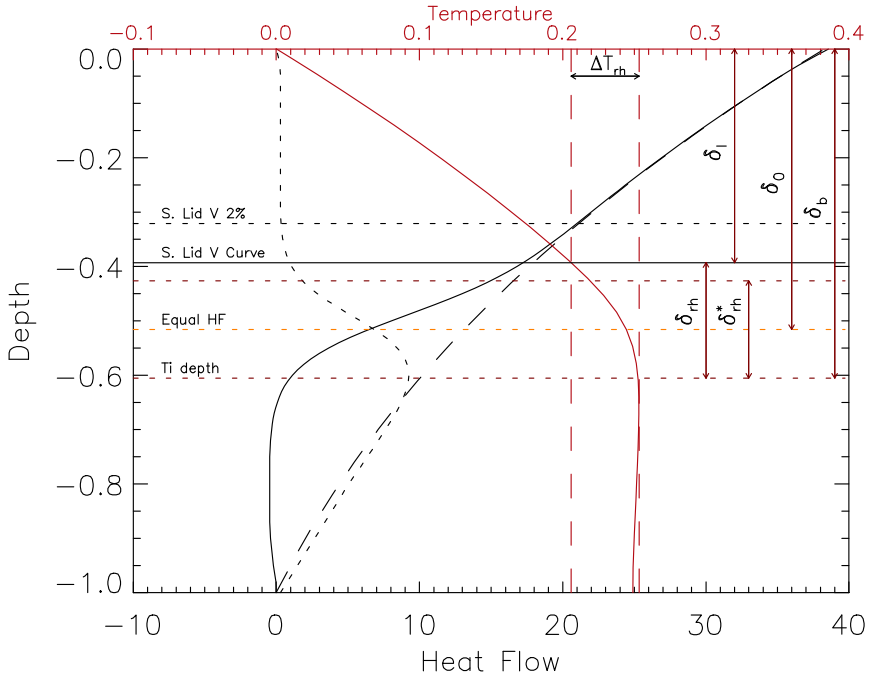

Figure 5.8. Typical temperature and heat-flow profiles, ($Ra_{H,0} = 1, \gamma = 60$, case 3 in appendix). The dashed line shows the theoretical conductive heat-flow while the dotted black line shows the advective heat-flow. The straight black and red lines are the observed heat-flow / temperature profiles. The upper two horizontal lines mark two different lid measures: V 2% marks the boundary where the horizontally averaged velocity reached more than 2% of $max(|\vec{v}|)$ and can therefore be seen as the boundary of a non eroded lid. The "V curve" marks the depth at which the tangent through the inflexion point of the velocity profile crosses zero, also marking the stagnant-lid depth as explained in the next section. The three dotted lines below represent the boundary layer based on the tangent through the inflexion point of the conductive heat-flow fraction, whereas the orange dotted line represents the "Equal Heat-flow", where the conductive heat-flow equals the convective heat-flow. The bottom dotted line marks the depth at which the tangent reaches zero and acts as lower thermal boundary layer that coincides with the depth of T_i.

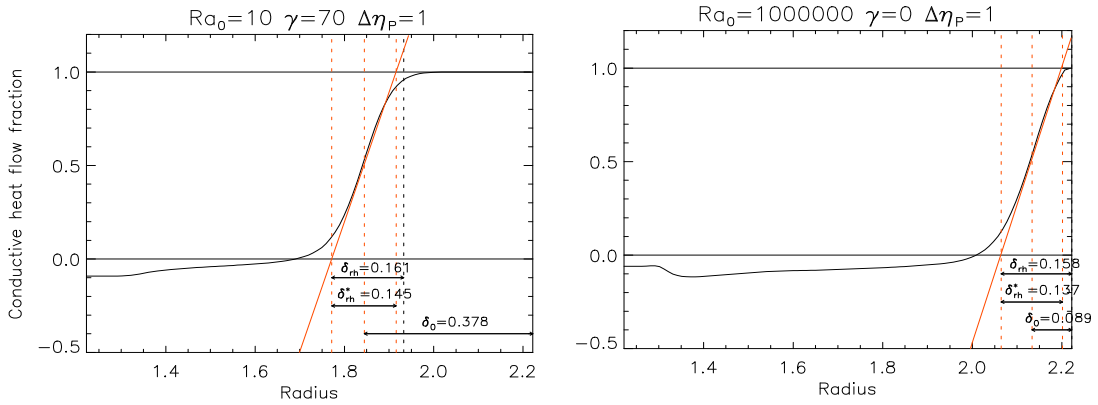

Figure 5.9. Parameters describing the boundary layer and how they are observed. It shows the ratio of theoretical conductive heat-flow to actual heat-flow. The inflexion point is determined by the steepest ascend, whereas the root of the tangent through the inflexion point marks the lower bound of the thermal boundary layer that coincides with the depth at which T reaches T_i. The upper bound has two possible definitions; either with the lid thickness observed through the velocity profile (black dotted line, δ_{rh}) where a_{rh} is approximately constant and the temperature of this depth can safely assumed to be equal to the theoretical conductive temperature at this depth, or the intersection of the tangent at one that, combined with the lower boundary, centers around δ_0 and is called the reduced boundary layer thickness δ^*_{rh}. As the right figure of an isoviscous case shows, this value never reaches zero. This method is further explained in section 5.6.3.

5.4 Lid Definition and the Rheological Constant

The radially averaged temperature profile of temperature-dependent viscosity convection starts at a certain viscosity contrast to approach the theoretical conductive temperature profile in the upper regions, i.e. convective motion ceases down to a certain depth that depends on the rheological gradient and the Rayleigh number. A stagnant-lid forms on top of a convecting layer. Within this lid, heat is only transported by conduction.

The boundary or thickness of this lid δ_l is not clearly defined. Some refer to a non-eroded stagnant-lid (Deschamps and Sotin, 2000), where advective forces are low enough to be guaranteed to leave the material within this region. This would have a physical equivalent definition of a threshold within the radially averaged velocity profile (not restricted to radial or lateral movement). The thickness of the lid is in this case equal to the depth where the velocity profile reaches the value of the expected error in the velocity, dependent on a percentage of the root-mean-square v_{rms} velocity. Even though this is the most plausible definition of a stagnant-lid as it really defines a 'stagnant' lid, it is also very weak because the velocity profile has a rather smooth logarithmic transition towards zero, so small variations in the threshold value have great impacts on the thickness of the lid. Two different values of this threshold percentage are tested (one and five percent cut-off) and illustrated together with other depth-averaged scalars in combination with the tangential-method (explained hereafter) in figure 5.10. The average and almost constant difference in determining the lid thickness with a one percent and a five percent cut-off is around 5% of the shell thickness, while the one-percent cut-off always produces thinner lids.

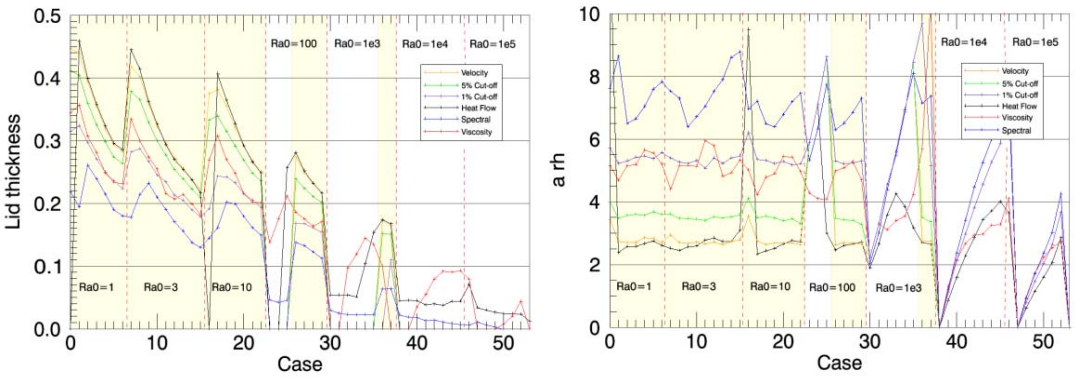

Figure 5.10. The lid thickness on the left side and the resulting a_{rh} values for all temperature-dependent cases with different measurement methods. The red vertical dashed lines mark a series of simulations with a similar Ra_0 and increasing γ. The yellow background marks cases with $M_1 < 0.6$, classifying them as stagnant-lid cases.

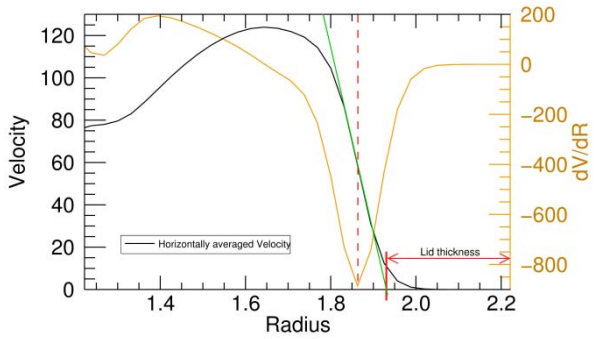

Figure 5.11. The method of the tangent through the inflexion point to determine the lid thickness, in this example with the velocity profile, marked as 'Velocity' in figure 5.9 and 'V curve' in figure 5.7.

A more promising and widely used definition is the root of the tangent through the inflexion point of the velocity profile e.g., Deschamps and Sotin (2000), as illustrated in figure 5.11. This method works well in most cases, but is not a consistent instrument of determining the lid thickness as it fails to work for weakly convecting systems that are not time-dependent as shown in figure 5.12. The velocity profiles of these weakly convecting systems include a second inflexion point close to the bottom that is in some cases larger than the upper and gives therefore false results. Another disadvantage of this method is the virtual presence of a lid on some degree-one cases. The same method over various other depth-averaged profiles has been tried and illustrated in figure 5.10, such as lateral viscosity contrast, spectral power and heat-flow. None of these methods led to a clear definition of the lid thickness.

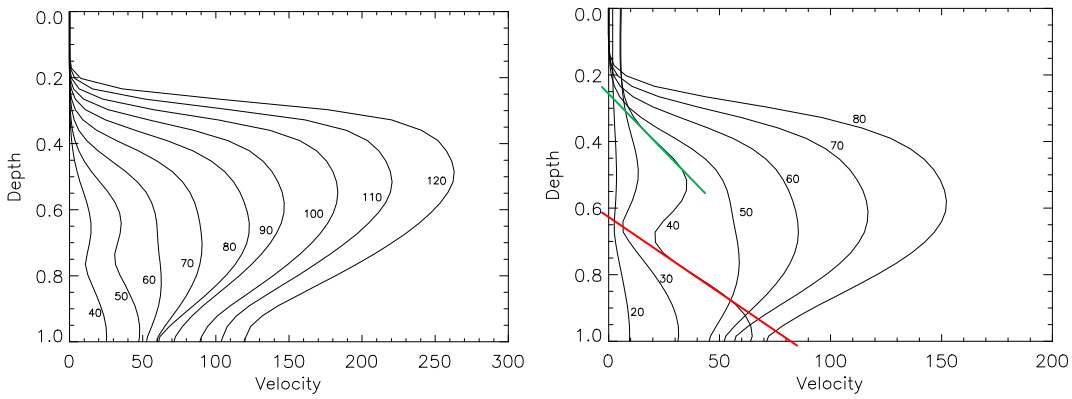

Figure 5.12. The velocity profiles of purely temperature-dependent cases with increasing γ marked on the profiles and a constant $Ra_{H,0}$ of 3 on the left side and 100 on the right. The steady-state cases with $\gamma = 40, 50$ on the left figure and $\gamma = 20, 30, 40$ on the right figure have a slope in the lower part steeper than in the upper, causing false results in determining the inflexion point.

Davaille and Jaupart (1993), Grasset and Parmentier (1998) and Reese *et al.* (1999a, 2005) found that at least for purely internally heated convection a fixed dependence of the rheological gradient to the temperature drop within the boundary layer exists (see section 5.6.2):

$$a_{rh} = \Delta T_{rh}\,\gamma \qquad \Delta T_{rh} = T_i - T_L \tag{5.7}$$

In this equation $T_L = T(\delta_l)$ is defined as the temperature at the base of the stagnant-lid and $T_i = T(\delta_b)$ the temperature of the well mixed interior. The temperature at the base of the stagnant-lid is therefore bound to the lid thickness δ_l. Assuming that a_{rh} should be as constant as possible, the different methods of determining the lid thickness could be benchmarked to check which method leads to the least standard deviation of a_{rh}. The various results for different methods are illustrated in figure 5.10 (right). The least standard deviation gave indeed the widely used method with the tangent through the inflexion point of the velocity profile. The results for a_{rh} are summarized in table 5.1.

a_{rh}/σ (number of cases)	Steady convection	Time-dependent convection
TC	3.14 / 0.33 (5)	2.88 / 0.04 (24)
TPC	6.46 / 2.44 (3)	3.71 / 0.16 (17)

Table 5.1. The results for a_{rh} with a lid defined as the root of the tangent through the inflexion point of the velocity profile, separated for different regimes.

5.5 Scaling Laws for the Boundary Layer

Boundary Layer Thickness Scaling with Nu and η_i

Although the center of the reduced boundary layer δ_0 is not useful to directly specify neither the upper (lid-depth) nor the lower boundary of the TBL (depth of T_i), it shows a strong correlation with the Nusselt number. This correlation is omnipresent for all cases in this study as figure 5.13 demonstrates and similar to the observation made by Solomatov (1995), which led to a scaling relation of $\delta_0 \sim Nu^{-1}$. A direct fit with a standard deviation of 4.3e-3 for all cases, including TPC, leads to the following equation:

$$\delta_0 = 0.53(Nu - 0.37)^{-1} \tag{5.8}$$

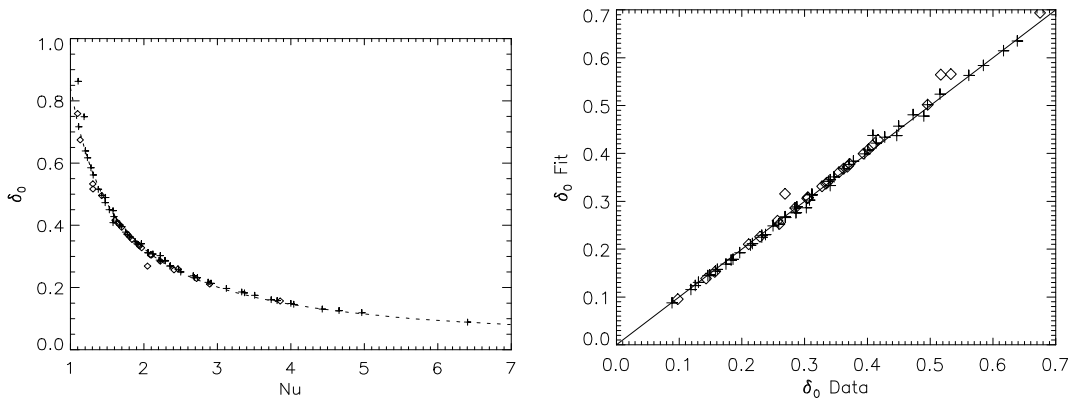

Figure 5.13. The depth of the center of the reduced thermal boundary layer δ_0, plotted are all 88 cases, whereas the crosses represent pure temperature-dependent viscosity cases and diamonds pressure and temperature-dependent cases. The dotted line on the left picture shows the fitting formula as described in the text and the resulting fit on the right.

It is possible to define an alternative upper boundary, not coinciding with the lid thickness, in a way that this new TBL centers around δ_0. A reduced boundary layer thickness can be defined as $\delta_{rh}^* = 2\delta_0 - \delta_b$. It is reduced in a way that it is always thinner than δ_{rh} and never reaches the surface, not even in isoviscous cases as further demonstrated in figure 5.14 as an extension to figure 5.9. This definition has the advantage of a correlation with the internal Rayleigh number $Ra_{H,i}$, but only after the transition into strongly time-dependent convection that occurs at $Ra_{H,i} \gtrsim 3e6$. Although it is not possible to constrain the lid thickness with that relation, it does benefit from the δ_0 correlation and constrains the lower boundary of the TBL (δ_b) very accurately. A best fit for values of δ_{rh}^* beyond that limit revealed

$$\frac{1}{2}\delta_{rh}^* = Ra_{H,i}^{-0.163} \tag{5.9}$$

To constrain the lid thickness δ_l from these relations, it must be possible to obtain the full boundary layer thickness with a similar relation. Solomatov (1995) constrains δ_{rh} from an exponentially decaying stress from the lid towards the surface that therefore strongly depends on the viscosity contrast:

$$\delta_{rh} \sim \frac{\delta_0}{\gamma T_i} = \frac{\delta_0}{\log \eta_i} \tag{5.10}$$

This definition considers δ_0 as the lid thickness. A fit of the models presented here leads to slightly different fitting parameters that are mainly due to a different geometry:

$$\delta_{rh} = 4\ \delta_0\ (\gamma\ T_i)^{-0.84} \sim \delta_0 \eta_i^{0.059} \tag{5.11}$$

As figure 5.15 demonstrates the good scaling results for the above equation, the advantage of the introduction of η_i in the previous equation makes it compatible with pressure-dependent cases as well. For the mobile regime, $\delta_{rh} \sim 2\ \delta_0 = Nu^{-1}$ as pre-

dicted by Solomatov (1995), which is illustrated in figure 5.16 and validates the measurement criteria of the parameters. This is also the base for the mobility criterion M_1 used in section 5.2.

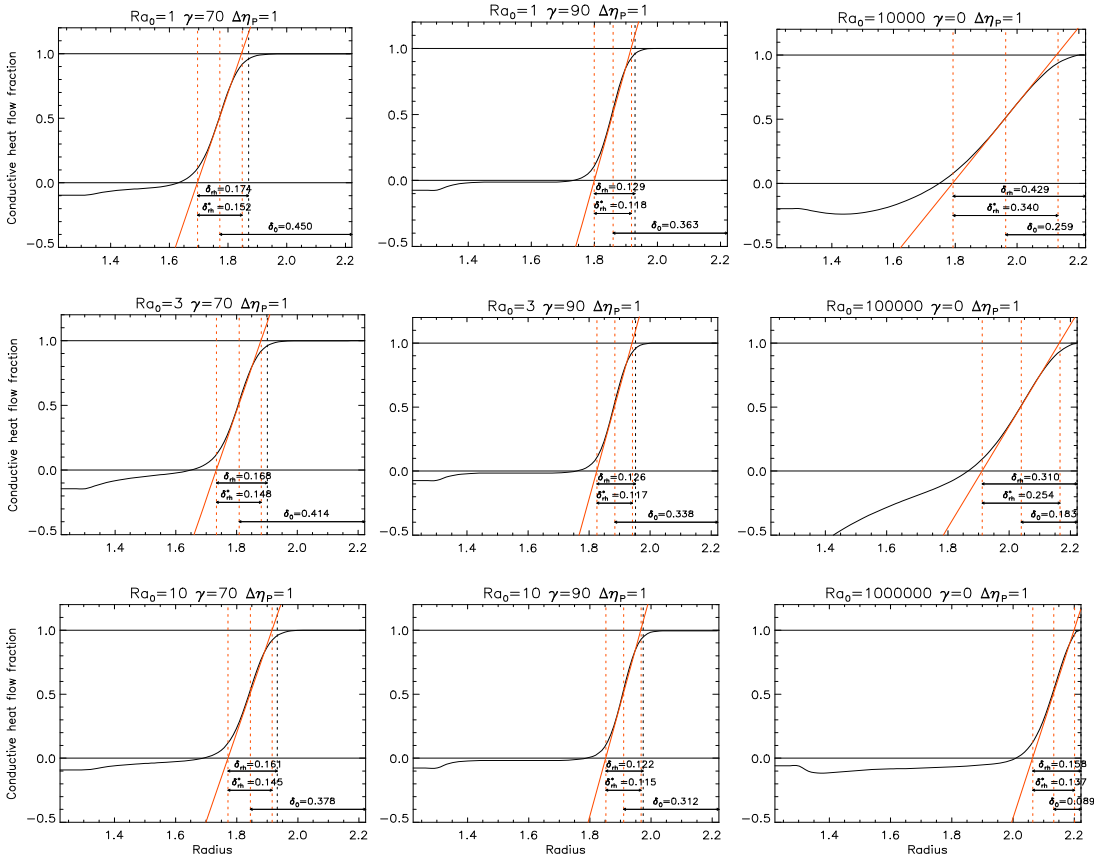

Figure 5.14. The parameters describing the boundary layer. It shows the ratio of theoretical conductive heat-flow to actual heat-flow. The inflexion point is determined by the steepest ascend, whereas the root of the tangent through the inflexion point marks the lower bound of the thermal boundary layer that coincides with the depth at which T reaches T_i. The upper bound has two possible definitions; either with the lid thickness observed through the velocity profile (black dotted line, δ_{rh}) where a_{rh} is approximately constant and the temperature of this depth can safely assumed to be equal to the theoretical conductive temperature at this depth, or the intersection of the tangent at one that, combined with the lower boundary, centers around δ_0 and is called the reduced boundary layer thickness δ^*_{rh}. As the right column of isoviscous cases show, this value never reaches zero.

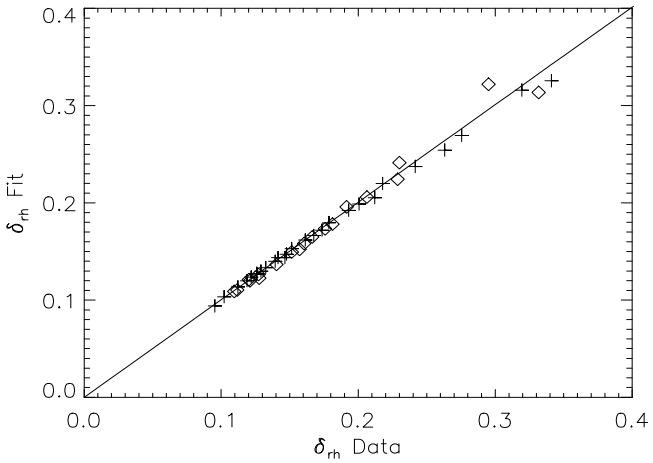

Figure 5.15. The fit for the boundary layer thickness from δ_0 and the interior viscosity η_i. Crosses represent stagnant-lid cases from TC and diamonds TPC.

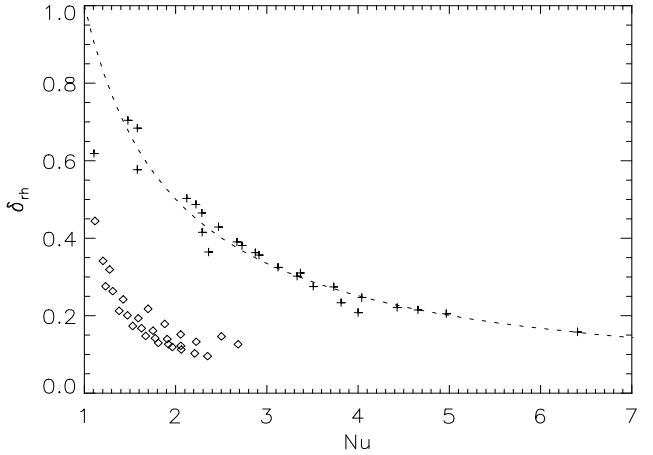

Figure 5.16. The boundary layer thickness of all TC, where crosses represent cases without a stagnant-lid and diamonds the stagnant-lid cases. The dashed line follows $\delta_{rh} = Nu^{-1}$.

Boundary Layer Thickness Scaling with Ra_δ

Another way of deriving δ_{rh} includes the Rayleigh number of the boundary layer (Ra_δ), defined as (Deschamps and Sotin, 2000)

$$Ra_\delta = Ra_{H,i}\,\delta_{rh}^5 \tag{5.12}$$

Linear stability analysis performed on isoviscous convection with free-slip boundaries predicts an Ra_δ independent of $Ra_{H,i}$. As figure 5.17 shows, the thermal boundary layer Rayleigh number is almost constant for purely temperature and strongly time-dependent convection. This is in contrast to Deschamps and Sotin (2000), who found a weak dependence on the internal Rayleigh number. A dependence on $Ra_{H,i}$ could only be observed for time-dependent TPC and in the opposite direction. The differences for the results of the current work to the results by Deschamps and Sotin (2000) are most likely due to the mode of heating and spherical geometry.

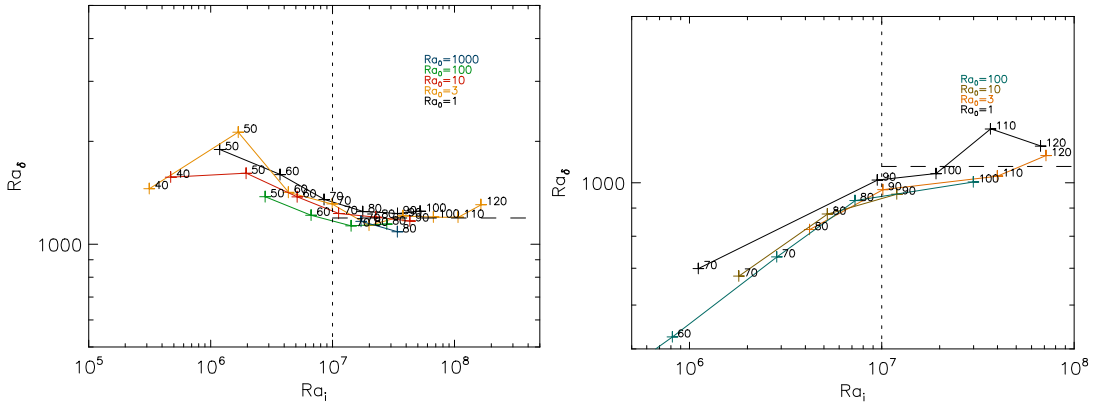

Figure 5.17. The relation of Ra_δ to $Ra_{H,i}$, left forTC and right for TPC. The horizontal line marks the average value to calculate δ, the vertical line the boundary to strongly temperature-dependent cases.

To constrain the value of Ra_δ, only cases with $Ra_{H,i} > 1e7$ were considered to ensure a strong time-dependent regime. For purely temperature-dependent viscosity cases, the mean value of $Ra_\delta = 1193$ with a standard deviation of $\sigma = 55$. This value in combination with equation (5.12) leads to a standard deviation of the boundary thickness of less than 57e-4 as illustrated in figure 5.18. Note that this value is close to the value predicted by Deschamps and Sotin (2000) for $Ra_i = 1e7$, who used the same method for determining the boundary thickness. However, Ra_δ in the present work does not significantly increase or decrease from this point any further as in their studies. Constraining the boundary layer thickness with a constant Ra_δ presents alternative fitting law to the previous method that directly fits a curve to the lid thickness. Instead, the following scaling for temperature-dependent cases has been derived:

$$\delta_{rh} = \left(\frac{Ra_\delta}{Ra_{H,i}}\right)^{\frac{1}{5}} = 4.12\, Ra_{H,i}^{-0.2} \tag{5.13}$$

While the two methods to constrain δ_{rh} are similar in quality for the time-dependent regime, the previous method leads better results for the steady state regime.

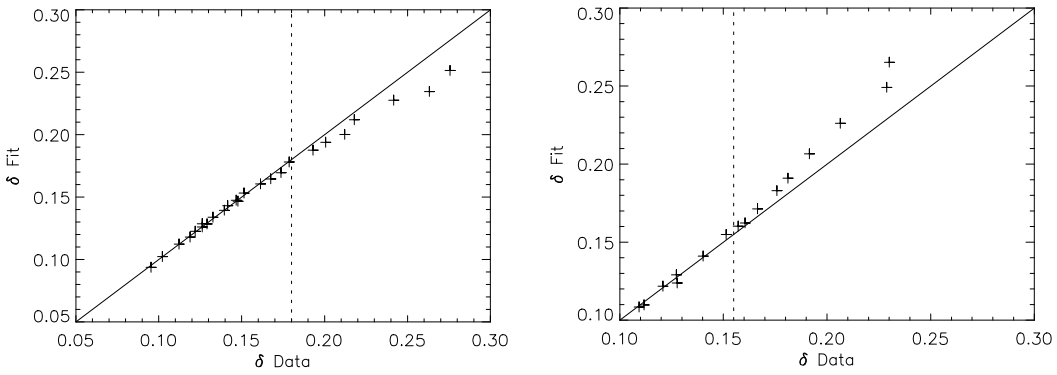

Figure 5.18. The scaling relation for the boundary layer thickness δ_{rh} according to a constant Ra_δ . The purely temperature cases on the left are evaluated with $Ra_\delta = 1193$ and the weakly pressure-dependent cases on the right with $Ra_\delta = 1070$. The vertical line marks the boundary to the time-dependent regime, with such cases situated on the left hand side.

For the cases with a weak pressure dependence the value of Ra_δ could not be adequately determined. As shown in figure 5.17 (right), the transition into strongly time-dependent convection is less pronounced and shows two different slopes before and after $Ra_i \sim 1e7$. This is equivalent to the much higher standard deviation observed from the previous direct fit with equation (5.11). Because the exponent from that fit is close to $1/6^{\text{th}}$ instead of $1/5^{\text{th}}$, it is possible that different bottom boundary effects from the pressure dependence reduce the depth of the active convecting layer and therefore change the Rayleigh number definition. The more important slope after $Ra_{H,i} = 1e7$ could not be determined because of insufficient cases in that range. Instead, a first-order assumption constrains Ra_δ to a constant value of ~1070, which is also close to the value observed by Deschamps and Sotin (2000). The resulting δ_{rh} fit is shown in figure 5.18. The possibility of a dependency of $Ra_{H,i}$ on Ra_δ cannot be excluded.

Stagnant-Lid Thickness Scaling

Both previous definitions of the boundary layer thickness share the lower boundary layer δ_b, thus the following relation for the lid thickness can be established:

$$\delta_l = \delta_0 + \frac{1}{2}\delta_{rh}^* - \delta_{rh} \tag{5.14}$$

Although three different fitting formulas are needed for this relation, equation 5.14 predicts the lid thickness for stagnant-lid cases within a mean error of 0.8% for TC. For TPC the standard deviation is higher and the mean error reaches 3% as illustrated in figure 5.19.

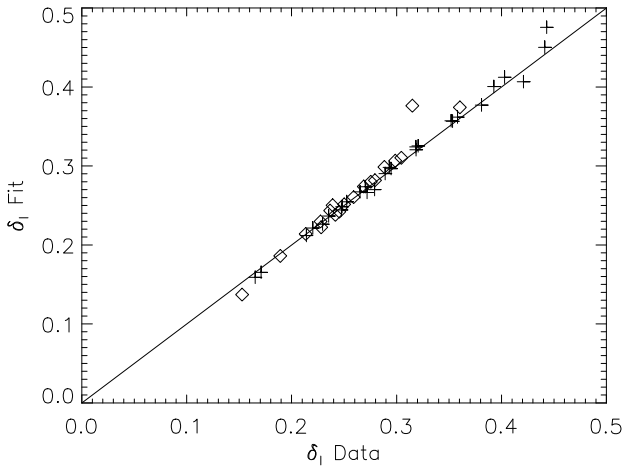

Figure 5.19. The resulting fit of the lid thickness from the boundary layer thickness scaling, crosses represent TC and diamonds TPC.

5.6 Scaling Laws for the Internal Temperature and Nusselt Number

The internal temperature is defined as the horizontally averaged temperature in the convecting interior. For purely internally heated convection, this temperature has a direct correlation with the Nusselt number and is defined as the maximum horizontally

averaged temperature within the convecting system. This temperature is a direct measure of the heat-flow (Reese *et al.*, 1999a) and is equal to defining the Nusselt number as the ratio of the theoretical maximal conductive temperature T_c to the actual maximal temperature T_i of the horizontally averaged depth profile.

$$Nu = \frac{\rho H r_t^2 \left(1 - \frac{3r_b^2}{r_t^2} + \frac{2r_b^3}{r_t^3}\right)}{6k(T_i - T_S)} = \frac{T_c}{T_i - T_S} \tag{5.15}$$

The importance of this temperature becomes evident from the definition of the internal Rayleigh number that is defined based on the viscosity of the internal temperature and plays an important role in many scaling laws.

One can find two different methods in the literature to determine the internal temperature for stagnant-lid convection. One described by Moresi and Solomatov (1995) and Solomatov (1995) follows a three-parameter fit. It is argued that this kind of fit fails for the stagnant-lid regime (e.g., Grasset and Parmentier, 1998, Reese *et al.*, 1999a, Reese *et al.*, 1999b, Reese *et al.*, 2005), which could not be agreed upon in this study with a complete independent inversion of all three parameters that was absent in the mentioned previous studies. This method will be further studied in the next section as “Method A”.

Another approach by Davaille and Jaupart (1993) and Grasset and Parmentier (1998) divides the whole mantle into two parts: the stagnant-lid and the convecting mantle below - with the assumption that beneath the stagnant-lid scaling laws similar to isoviscous convection can be applied. This method is further discussed in section “Method B”.

A third new approach is based on the complete reconstruction of the radial heat-flow profile. This method has the advantage of treating the system as one and does not require a definition for the lid thickness. This method will be discussed in section “Method C” and is first presented in this thesis.

5.6.1 Method A: Classic Power-Law Scaling

Boundary layer theory predicts a relation of the Nusselt number and the Rayleigh number for internally heated isoviscous convection in the form of $Nu \sim Ra^{1/4}$ (e.g., Schubert and Zebib, 1980, Schubert *et al.*, 2001). Parmentier et al. (1994) corrected the exponent for time-dependent three-dimensional convection to ~0.23. A smaller value of the exponent relative to the theoretical value of the boundary layer theory was observed for time-dependent bottom heated convection by Hansen *et al.* (1990, 1992b). Solomatov (1993, 1995) extended this theory to temperature-dependent viscosity. The Frank-Kamenetskii parameter $\theta = \gamma\, T_i = \log \eta_i$ was introduced to describe the Nu-Ra relationship with three free parameters in the form of

$$Nu = a\,\theta^{\alpha}\,Ra_{H,i}^{\beta} \tag{5.16}$$

Although Grasset and Parmentier (1998) and others argued that this relationship cannot be used for stagnant-lid convection, it is shown in the present study that a full inversion of all three parameters led to satisfying results, as the standard deviation in table 5.2 and figure 5.20 demonstrates. The high standard deviation for steady state convection is expected since in a full three-dimensional spherical shell environment an additional influence of the resulting or triggered mode through initial conditions cannot be neglected. This means that more than one possible steady state configuration of the same setup is possible depending on the initial conditions which has a direct influence on the Nusselt number as well. This is also equivalent with observations made in two-dimensional boxed models that show large variations in the lid thickness for steady state convection with Newtonian viscosity (e.g., Moresi and Solomatov, 1995, Solomatov and Moresi, 1997). In time-dependent convection the thickness becomes fairly uniform in all cases because the locations of the plumes are not fixed but vary randomly (e.g., Solomatov and Moresi, 2000b). Figure 5.20 demonstrates this behavior for all stagnant-lid cases and shows a drop of the mean variation in lid thickness around the transition to time-dependent convection.

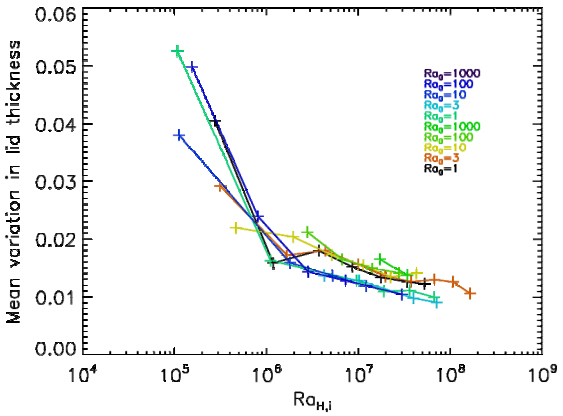

Figure 5.20. The mean variation of the non-dimensional lid thickness (for an overall shell thickness of one). The upper five surface Rayleigh numbers describe TPC, the lower five TC cases. The transition into time-dependent convection around 10^6 *is clearly visible, as well as generally reducing thickness variations for time-dependent TPC.*

	Steady convection	**Time-dependent convection**
TC	0.68 / -0.4 / 0.12 / 7.6e-3 (5)	0.72 / -0.74 / 0.175 / 1.7e-3 (24)
TPC	0.8 / -0.945 / 0.252 / 2e-4 (3)	2.08 / -0.73 / 0.12 / 3.1e-3 (17)

Table 5.2. The results for the $Nu = a(\gamma T_i)^{\alpha} Ra_{H,i}^{\beta}$ *fit, separated for the different regimes. The values are indicated by the following order:* a */*α */* β */* σ *(no. of cases)*

The results for a direct fit of all three parameters are summarized in table 5.2. Although the parameters are not consistent with the theoretical values of ¼ (Schubert *et al.*, 2001) for β and $\alpha = -(1+\beta)$, which is why this method is discarded by others,

they still produce agreeable results if they are inverted independently without assuming one parameter as fixed from theory. The reasons for the discrepancies to the theoretical values are mainly the mixed boundary conditions: while free-slip is imposed at the bottom, the formation of a stagnant-lid implies a more rigid boundary condition on the top of the convecting layer.

To derive the internal temperature from the two input variables Ra_0 and γ, the scaling law 5.16 is decomposed. Equation 5.16 can be rewritten with eq. 5.15 and 5.5 in the non-dimensionalized form ($T_S = 0$!) for purely TC to

$$\frac{T_C}{T_i} = a\,(\gamma\, T_i)^{\alpha}\,(Ra_0 \exp(\gamma\, T_i))^{\beta} \tag{5.17}$$

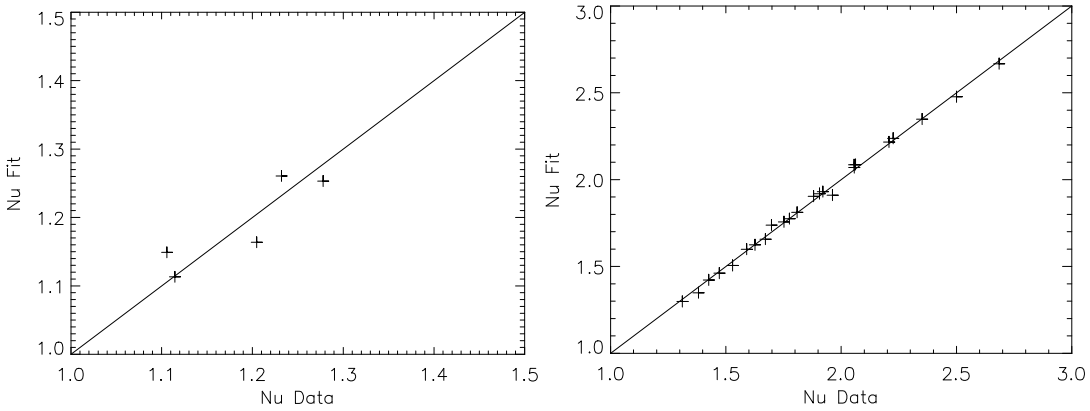

Figure 5.21. The result of the fitting equation 5.17 for TC cases, while steady state cases are on the left and time-dependent cases on the right.

For TPC this scaling turns out to be unclear because a decomposition of η_i lags the unknown depth, i.e. equation 5.5 cannot be used to resolve η_i:

$$\frac{T_C}{T_i} = a\left(\ln \eta_i^{-1}\right)^{\alpha}\left(Ra_0\, \eta_i^{-1}\right)^{\beta} \tag{5.18}$$

However, neglecting the depth dependence for the fit yields equally good results as assuming a fixed depth like Christensen (1984a). This has the consequence that the parameters again in table 5.2 vary from other results, whereas no theoretical base exists so far for depth dependent viscosity.

5.6.2 Method B: Scaling with the Rheological Constant

As assumed by Solomatov (1993, 1995) and later proofed by laboratory experiments for internally heated convection by Davaille and Jaupart (1993) and further confirmed by Grasset and Parmentier (1998) and Reese et al. (1999a, 2005) through numerical simulations, the temperature drop within the thermal boundary layer below a stagnant-lid can be described solely by the rheological gradient γ in a way that

$$\Delta T_{rh} = T_i - T_L = a_{rh}\gamma^{-1} \tag{5.19}$$

where a_{rh} is the rheological constant, T_i the temperature of the convecting interior and T_L the temperature at the bottom of the lid δ_L. After Grasset and Parmentier (1998), the convective system consists of two parts; the convecting interior including the boundary layer and a stiff upper part (the stagnant-lid) that is mainly controlled by conductive heat transport. Further it is assumed that the interior part can be treated like isoviscous convection with the well known scaling law in the form of

$$Nu = a\, Ra^{\beta} \tag{5.20}$$

Scaling relationships can be derived from the knowledge that the temperature in the stagnant-lid part follows the conductive profile. In Section 5.5, the lid thickness has been determined with the assumption that the rheological constant is as constant as possible, which is important for the depth separating these two systems. Due to the low lateral and radial viscosity variations below the stagnant-lid (section 5.2, figure 5.4 / 5.7 left), it is possible to rescale the interior convection and treat it with two parameters, which results in a re-defined Rayleigh number based on the interior viscosity η_i and the effective non-dimensionalized thickness of $1 - \delta_L$, where δ_L is the lid thickness:

$$Ra_1 = Ra_0\,(1 - \delta_L)^5\,\eta_i^{-1} \tag{5.21}$$

According to the isoviscous Rayleigh number definition, the temperature must be re-scaled (temperature is scaled with the thickness of the convecting layer) to an "isoviscous" temperature according to

$$T_1 = \frac{T_i - T_L}{(1 - \delta_L)^2} \tag{5.22}$$

The direct relation of the Nusselt number to the internal temperature T_i (equation 5.15) for purely internally heated convection allows modifying the equation (5.21) to

$$T_1 = a\, Ra_1^{\beta} \tag{5.23}$$

The resulting fit is summarized in table 5.3 and illustrated in figure 5.22 for different regime types. It is worth noting that the mobile regime of TC results in fitting constants very close (less than 3e-3 difference in β) to those observed by Parmentier *et al.* (1994), who studied isoviscous three-dimensional (boxed) internally heated convection. Another well corresponding match could be identified from Grasset and Parmentier's (1998) study, as shown in table 5.3. It is interesting to note that both studies used a no-slip top boundary condition from isoviscous models to obtain these values, whereas the present study rescales the convection beneath the stagnant-lid with the method described in section 5.4 to determine δ_l. This confirms the assumption that convection beneath the stagnant-lid can be treated as isoviscous (Davaille and Jaupart, 1993, Solomatov and Moresi, 1996, Grasset and Parmentier, 1998) and further that the boundary to the stagnant-lid is close to a no-slip boundary condition.

	Steady state convection	Time-dependent convection
TC	5.04 / -0.3 / 1.84e-2 (5)	2.34 / -0.231 / 1.6e-3 (24)
Grasset 98		2.38 / -0.227 / ?
Parmentier 94		? / -0.2338 / 1.9e-3 (4)
TPC	5.18 / -0.31 / 5e-2 (3)	1.02 / -0.178 / 3e-3 (17)

Table 5.3. The results for the $T_1 = aRa_1^{\beta}$ fit, separated for different regimes. The order of the indicated values is a / β / σ (number of cases). Grasset 98 refers to the values obtained by Grasset and Parmentier (1998), originating from a 2D (aspect ratio 2:1) boxed model and to Parmentier et al. (1994), who performed simulations within a 3D box (aspect ratio 4:4:1).

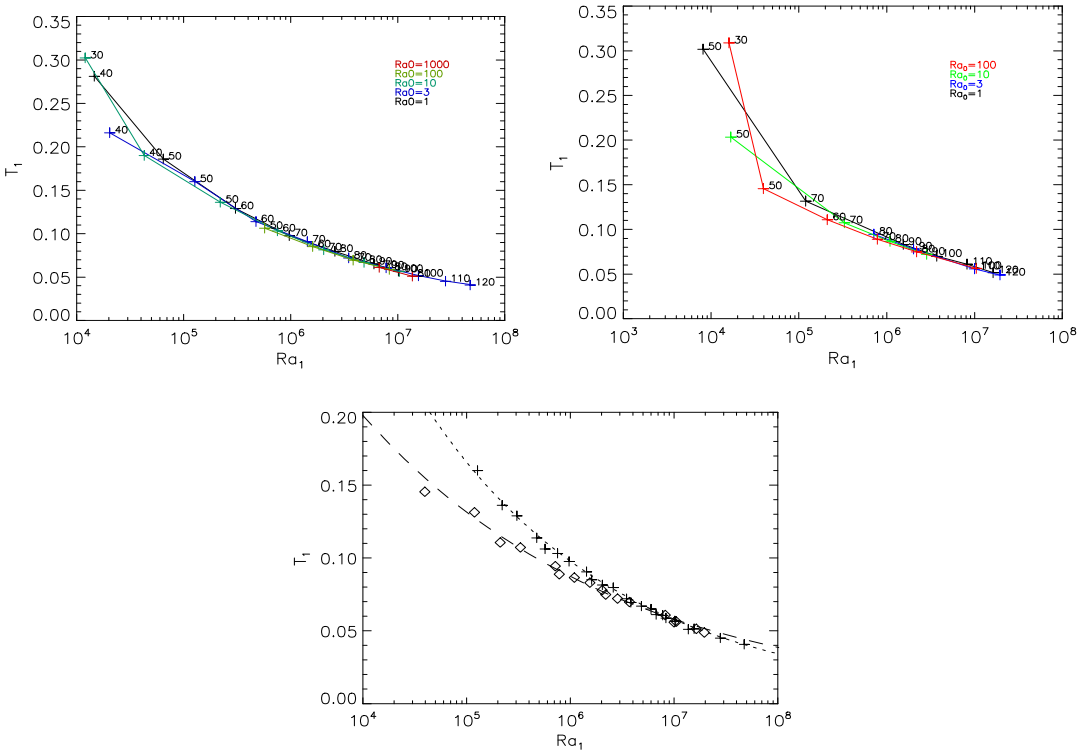

Figure 5.22. The correlation of the interior quasi isoviscous Rayleigh number to its interior temperature equivalent for stagnant-lid cases. The left and right top picture shows the rescaled values with lines that connect cases for a certain surface Rayleigh number. The values on the marks represent the according γ value. Clearly visible is the distinction between steady-state cases with lower Ra_1 and time-dependent cases in the upper two figures. The bottom picture shows the correlation function from the fit for all time-dependent cases whereas crosses represent TC and diamonds TPC.

The non-dimensionalized (scaled with $\rho H d^2/k$) temperature at the base of the lid can be found from the conductive temperature profile in the lid for internally heated convection and spherical geometry:

$$T(r) = \frac{1}{6}\left(-r^2 + r_i^3\left(\frac{-2}{r} + \frac{2}{r_o}\right) + r_o^2\right) \tag{5.24}$$

This equation leads also to the maximal conductive temperature $T_C = T(r_b)$ in the spherical shell, which is important for the Nusselt number (see section 4.1). Inverting

equation (5.24) yields the radius based on the conductive profile, and can be simplified for a radius ratio of 0.55 returning the non-dimensionalized depth between zero and one:

$$\mathrm{d(T)} = \frac{20}{9} - \frac{4(-5)^{\frac{1}{3}}(1777 - 1620T) + (1 - i\sqrt{3})\left(266200 + 18\sqrt{30}\sqrt{(-7 + 20T)(2257333 + 6480T(-397 + 135T))}\right)^{\frac{2}{3}}}{36\,5^{\frac{2}{3}}\left(266200 + 18\sqrt{30}\sqrt{(-7 + 20T)(2257333 + 6480T(-397 + 135T))}\right)^{\frac{1}{3}}} \tag{5.25}$$

In combination with $\delta_L = d(T_L)$ and equations (5.19, 5.20, 5.21), it is possible to derive the interior temperature with

$$\frac{-a_{rh}\gamma^{-1}}{(1 - \mathrm{d}(T_i - a_{rh}\gamma^{-1}))^2} = a\,(Ra_0\,(1 - \mathrm{d}(T_i - a_{rh}\gamma^{-1}))^5 \exp(\gamma\,T_i))^{\beta} \tag{5.26}$$

Besides using the parameters resulting from an observed a_{rh} from section 5.4 and the values from table 5.2 and 5.3, it is possible to invert all three free parameters from this equation directly. While it would not put a meaningful constraint on a_{rh} because of its weak dependence on a and β (Grasset and Parmentier, 1998, Solomatov and Moresi, 2000a, Reese *et al.*, 2005), it does strengthen the fitting procedure with the rather large amount of data points of this study. To provide a better understanding of the dependence of all three parameters, the a parameter was varied over a reasonable range while the remaining two parameters were fitted. The result is shown in 5.23 and it is interesting to see that indeed for a wide range the error does not change significantly. While a is in the range between ~1 and ~4.5, the resulting error has a negligible difference. This puts a_{rh} in a valid range between 0.5 and 7, and β in a range between -0.21 to -0.26, which is approximately in between the two theoretical values for internally heated convection with free-slip (-0.25) and no-slip (-0.2) boundaries (Schubert *et al.*, 1990). This is evident from the definition of a_{rh} itself; a lower value yields a more eroded stagnant-lid that gives the convection below an interface definition towards a no-slip upper boundary while higher values provide a more free-slip boundary through the shear effects of an increased radial viscosity contrast. Therefore it is possible to choose the erosion level with the choice of a_{rh} and a further lookup of best-fits of a and β. However, the lowest error was found for the time-dependent regime at $a = 3.57, a_{rh} = 5.64,\ \beta = -0.22$, which is marked by the vertical dashed line in figure 5.23 and figure 5.24.

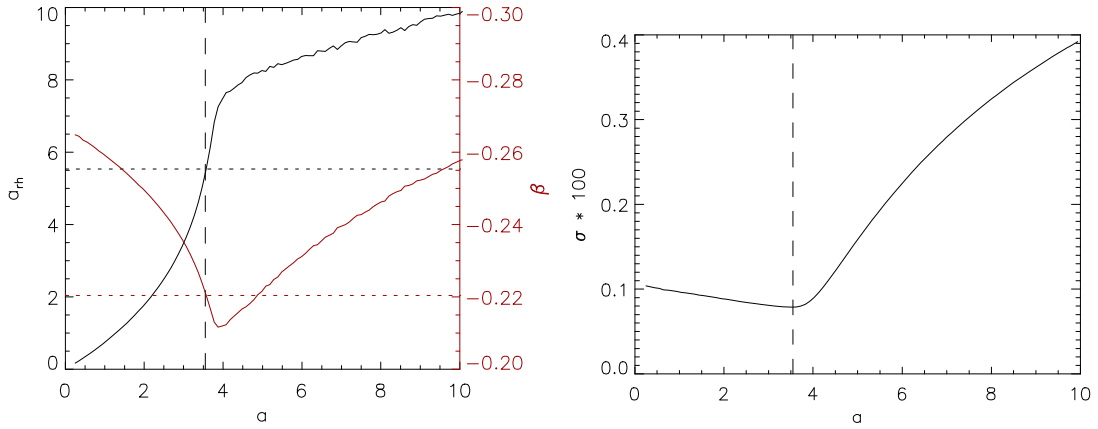

Figure 5.23. The best fit of equation 5.26 for all time-dependent TC with a fixed a on the left and the resulting standard deviation for the result on the right. The dashed vertical line marks the position of the lowest error with according horizontal lines on the left picture for the remaining two parameters.

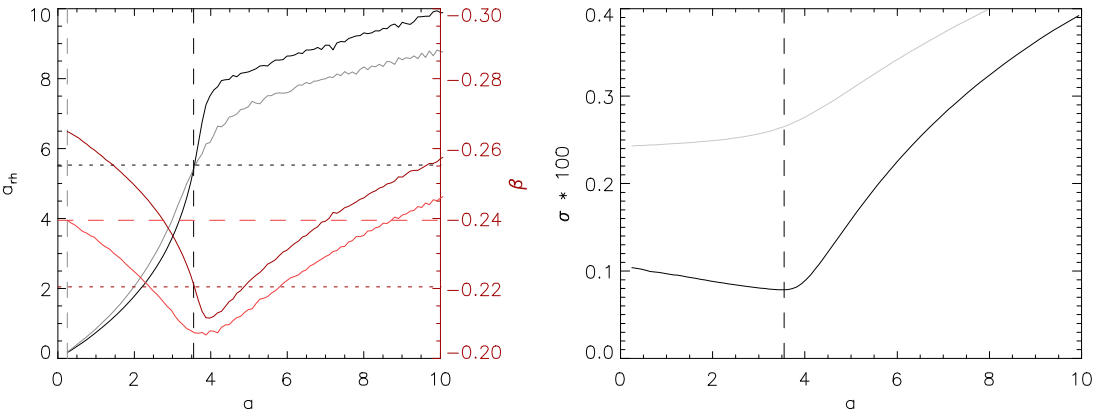

Figure 5.24. Similar to figure 5.23 but with overplotted fits for time-dependent TPC (grey and light red) and the resulting error.

The same method applied to time-dependent TPC leads to a significant higher error and suggests that a decomposition of stagnant-lid and a convecting interior is insufficient in case of additional influence of pressure-dependent viscosity. This is mainly due to the missing influence of pressure dependence in the interior viscosity term that yields from an unknown depth of η_i. Opposite to the results of TC, this depth does not coincide with the depth of T_i. Additional scaling laws for the depth of η_i are required to properly constrain the heat-flow with this mechanism. Figure 5.24 shows the applied method for TPC and demonstrates that the relation between a and a_{rh} stays approximately the same while β shows a generally lower value. This supports the boundary layer theory (Fowler, 1993, Dumoulin *et al.*, 1999) since the influence of pressure at greater depths results in a weak secondary boundary layer that can be seen as turning the bottom free-slip condition slowly into a no-slip condition for increased pressure dependence, thus reducing β.

5.6.3 Method C: Heat-flow Profile Inversion

The heat transport mechanisms of a Rayleigh-Bénard setup consist of conductive heat transport on an atomic level and transport through convective heat transport. While looking at the heat-flow profile together with the velocity profile, it is clear that the observed heat-flow q is a composition of an convective part q_a and a conductive part q_c, as illustrated in figures 5.8 and 5.9. To derive the heat flux profile q, the heat equation itself is reduced to one dimension by

$$q = -k\,\nabla T = -k\,\frac{\partial T}{\partial r} \tag{5.27}$$

If the heat transport is dominated by advection, the radial temperature derivate is close to zero, while conductively transported heat follows the theoretically known profile. This profile is coupled to the conductive temperature and yields indirectly the advective heat-flow profile:

$$q_a = q - q_c \tag{5.28}$$

While the theoretical conductive temperature or heat-flow profile is not depth dependent for bottom heated convection, it is a more complex function in a 3D spherical environment for purely internally heated convection, where the heat flux at the bottom equals zero and is constantly increasing towards the surface. For better comparison between the heating modes, it is also possible to calculate the profile of the conductive heat-flow fraction q_f (figure 5.9 / 5.14):

$$q_f = \frac{q}{q_c} \tag{5.29}$$

It therefore describes the percentage of conductive heat flux acting at a certain depth and is useful to define boundary layer properties as well as shown in figure 5.9. This fraction consists of only one transition between convective and conductive heat-flow for internally heated convection and can reach negative values as well, which are due to effects of the Boussinesq approximation (e.g., Hansen *et al.*, 1992a, 1993). Ignoring these effects has no influence on the internal temperature and assuming zero where the profile reaches negativity is more realistic as long as the Boussinesq approximation is able to describe the convection appropriately.

Knowing the progression of this transition, i.e. the position (or depth) and slope, allows a reconstruction of the radial heat-flow profile that in consequence leads to a reconstruction of the temperature profile. In turn, several key-variables of convection can be reconstructed from those profiles: the lid thickness, internal temperature, boundary layer thickness and depth. To reconstruct this transition, several basic step functions (sometimes called soft-step functions) such as the error function, Gompertz function, logistic function, incomplete and regularized gamma functions were equipped with up to four free parameters and fitted against a q_f profile of a stagnant-lid case.

Most of these step functions failed to reconstruct the transition appropriately except for one version of the regularized gamma function that is defined as

$$\mathrm{P}(a,x) = \frac{\gamma(a,x)}{\Gamma(a)}, \tag{5.30}$$

where $\gamma(x,a)$ is the lower incomplete gamma function defined as

$$\gamma(a,x) = \int_0^x t^{a-1}\, e^{-t}\, dt \tag{5.31}$$

and $\Gamma(a)$ represents the gamma function with

$$\Gamma(a) = \int_0^\infty t^{a-1}\, e^{-t}\, dt \tag{5.32}$$

The lower incomplete gamma function is related to the error function as

$$\operatorname{erf} z = \pi^{-\frac{1}{2}}\, \gamma\left(\frac{1}{2}, z^2\right) \tag{5.33}$$

The regularized gamma function has two possible configurations to create a one-dimensional step; either for a fixed a or a fixed x. Not only yielded the version for a fixed x a reasonable result, it is possible to describe the jump with only two free parameters with a remarkably high accuracy. To reconstruct the heat-flow profile, the following equation was used:

$$q(d) = q_c(d)\ \left(1 - \mathrm{P}\left(\zeta\, d^{\epsilon}, 1\right)^4\right) \tag{5.34}$$

In this **direct fit** to a given heat-flow fraction profile, ϵ and ζ are constant for a certain case and d is the non-dimensionalized depth. The power of four was in the original fit a free parameter as well but turned out to be a constant very close to four in all cases that might describe geometrical influences such as the radius ratio. The influence of the remaining two free parameters on the regularized gamma function is displayed in figure 5.25.

Although this method works for almost all cases (extremely weak convective systems fail because the advective heat transport is at no depth the dominant mechanism), the reconstruction is useless until it is possible to bind the two parameters to meaningful physical parameters that describe the convection. A fit for ζ and ϵ based on the surface Rayleigh number $Ra_{H,0}$ and the rheological gradient γ could be established for the stagnant-lid regime (**indirect fit**).

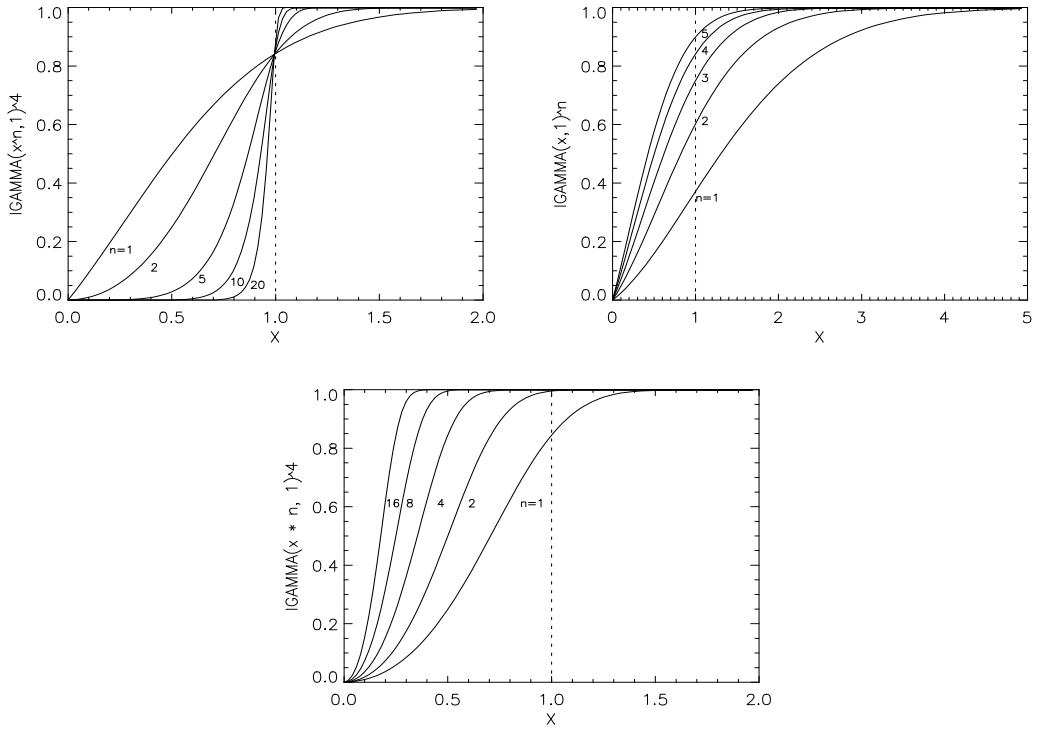

Figure 5.25. Influencing factors used in the fitting formula as free parameters of the regularized incomplete gamma function $P\ (x, a)$ (called IGAMMA in the plot) as they are used to reconstruct the heat-flow profile.

No unification of the mobile and stagnant-lid regime could be accomplished with the indirect fit, so a common three-parameter fit for the TC in stagnant-lid regime based on the surface Rayleigh number $Ra_{H,0}$ and the rheological gradient γ yields the following indirect fitting equations:

$$\epsilon = 0.0864\,\gamma + 0.277\ \ln Ra_0 - 2.54 \tag{5.35}$$

$$\zeta = 4.33\,\epsilon\,Ra_0^{-\frac{1}{6}} + 4.8 \tag{5.36}$$

The error for this fit is almost equal to method B (if the internal temperature is calculated from the reconstructed heat-flow profile) for TC but works generally better for TPC with these parameters:

$$\epsilon = 0.0811\,\gamma + 0.287\ \ln Ra_0 - 3.17 \tag{5.37}$$

$$\zeta = 3.43\,\epsilon\,Ra_0^{-0.14} + 4.72 \tag{5.38}$$

Because ϵ is included in the fitting equation for ζ, the resulting error of the ϵ fit is included in the ζ fit as well. Alternative better fitting formulas may therefore exist with possibly less free parameters. The results of this fit are illustrated in figure 5.26, while figure 5.28 shows an application of selected cases to this kind of reconstruction. The final results to compute the internal temperature with this method is demonstrated in figure 5.27 for the direct and indirect fitting method.

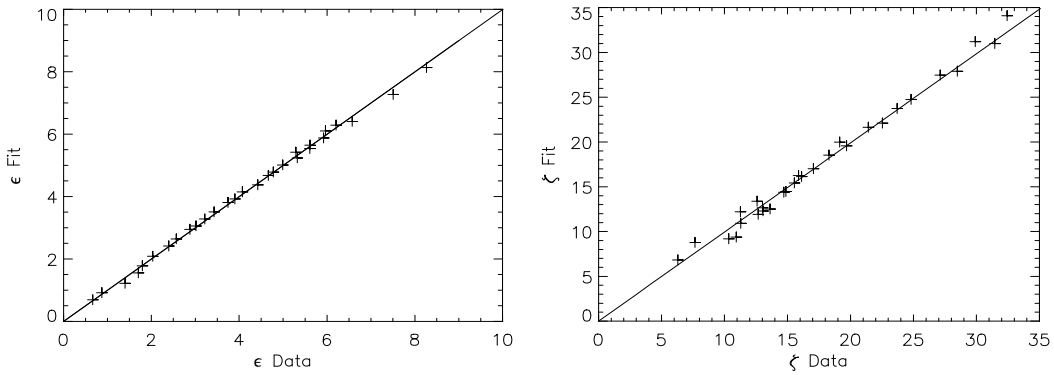

Figure 5.26. The resulting ϵ and ζ fit that followed a direct fit to each individual profile according to the equations in the text.

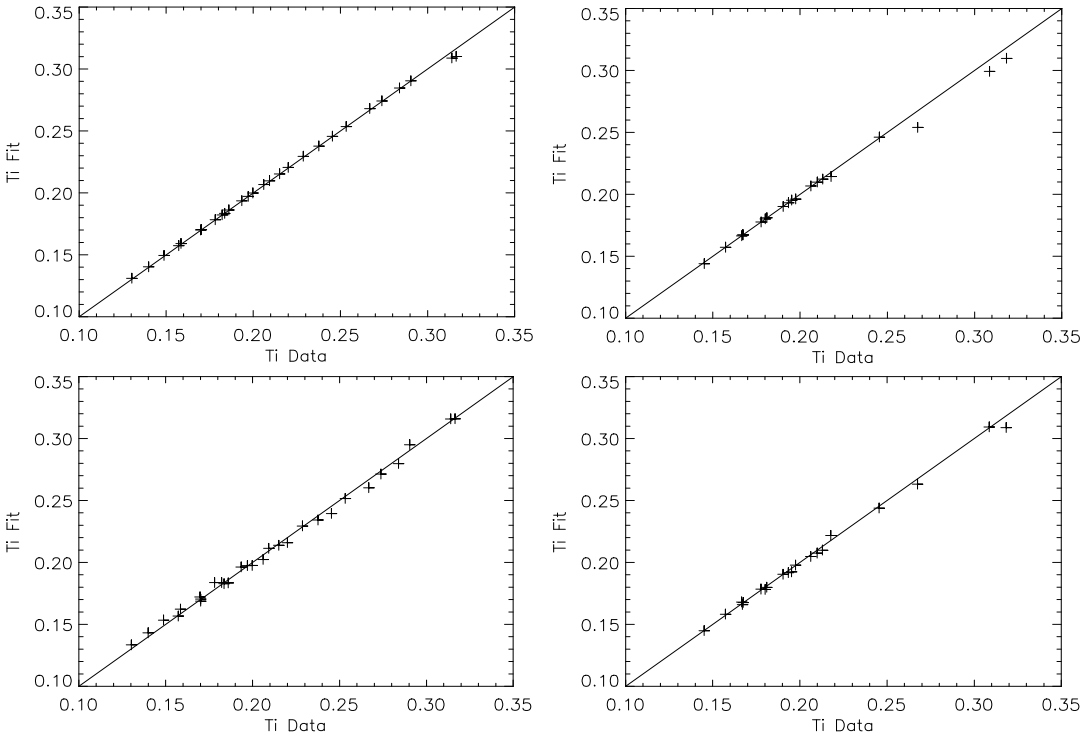

Figure 5.27. The result of the reconstruction quality for the internal temperature with the direct fit on the top and the indirect fit on the bottom, whereas TC are on the left side and TPC on the right.

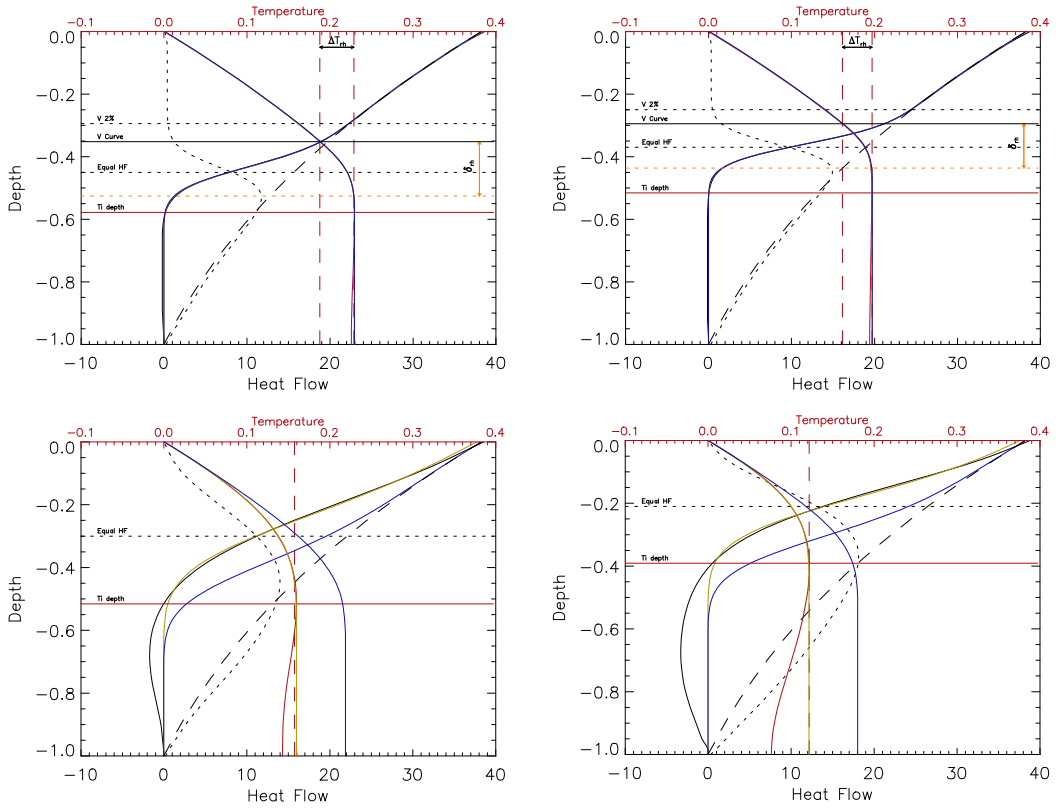

Figure 5.28. Selected results of a reconstruction of the heat-flow- and temperature profile based on the regularized incomplete gamma function. The dark yellow line shows the result of a direct two-parameter fit and the blue lines show the indirect fit using $Ra_{H,0}$ and γ to reconstruct the mentioned two free parameters. The upper two cases are in the stagnant-lid regime and are numbered 3 and 11 in the appendix. The lower two cases are low-degree cases 32 and 41. Even though the indirect fit fails completely here, the direct method still produces correct results.

5.7 Spectral Analysis

Internally heated convection of a Boussinesq fluid with infinite Prandtl number, in combination with strongly temperature-dependent viscosity creates short wavelength structures below the stagnant-lid and therefore shows effects similar to bottom heated convection (e.g., Tackley, 1996b, Ratcliff *et al.*, 1997, Trompert and Hansen, 1998a). The present parameter study reveals a strong correlation of the internal Rayleigh number to the dominant mode that also exists with pressure-dependent viscosity, although with a different correlation.

According to the method described in section 3.7, the temperature and velocity field of all cases are spectrally analyzed. Their dominant mode reveals a strong correlation to the internal Rayleigh number in the stagnant-lid regime. This correlation was expected in literature to exist for bottom and internally heated convection (e.g., Ratcliff *et al.*, 1996a, Reese *et al.*, 2005, Stemmer *et al.*, 2006, Zhong *et al.*, 2008), as convection turns into smaller scales below the stagnant-lid. This behavior is studied in detail in the present parameter study.

A strong correlation between the internal Rayleigh number and the dominant mode has been identified but could be significantly improved by utilizing the weighted mode ω. Although the fitting parameters do not notably change in contrast to the dominant mode, the error is significantly reduced. For the steady state cases, a minimal possible mode ω_{min} can be identified that stays constant until the transition to the time-dependent regime occurs. This minimal mode has a relatively large error because multiple possible degrees may exist for the same $Ra_{H,i}$ in the steady-state part (e.g., Ratcliff *et al.*, 1995, Ratcliff *et al.*, 1996b, Ratcliff *et al.*, 1997, Zhong *et al.*, 2008). An error of plus-minus two degrees is expected for the fitting formula to account for the stability uncertainty and additional temporal mode-cycling possibilities. Note that the minimal mode further depends on the assumed radius ratio.

The transition into the time-dependent regime is accompanied by a step towards higher modes and further increases linearly as displayed in figure 5.29. The following fitting formula can describe the transition into the time-dependent regime with a step function, which is chosen to be the regularized gamma function P as described in section 5.6.3.:

$$\omega = \mathrm{P}\left(Ra_{S-T}, Ra_{H,i}\right) m \left(\ln\left(Ra_{H,i}\right) - \ln(Ra_{S-T}) + \frac{\omega_{step}}{m}\right) + \omega_{min} \tag{5.39}$$

In the above equation Ra_{S-T} is the internal Rayleigh number at which the transition to the time-dependent regime occurs, m is the slope in the time-dependent part and ω_{step} is the observed rapid increase at $Ra_{H,i} = Ra_{S-T}$. The results for the stagnant-lid regime are shown in figure 5.29. A similar behavior for the mobile regime could not be observed, as demonstrated in figure 5.31. The fitting parameters are summarized in table 5.4. Only a too limited amount of data exist for the steady-state pressure-dependent cases, which results in a high uncertainty in the step size ω_{step} and transitional Rayleigh number Ra_{S-T}. However, all cases in that range fit well with the parameters for TC. As a reasonable first-order approximation, it is assumed that the fitting parameters for TPC are similar to those parameters from the TC fit. A lower slope m for TPC yields generally lower modes in the time-dependent regime, as predicted by Bunge *et al.* (1996), but no influence on the minimal observable mode below the stagnant-lid ω_{min} can be identified.

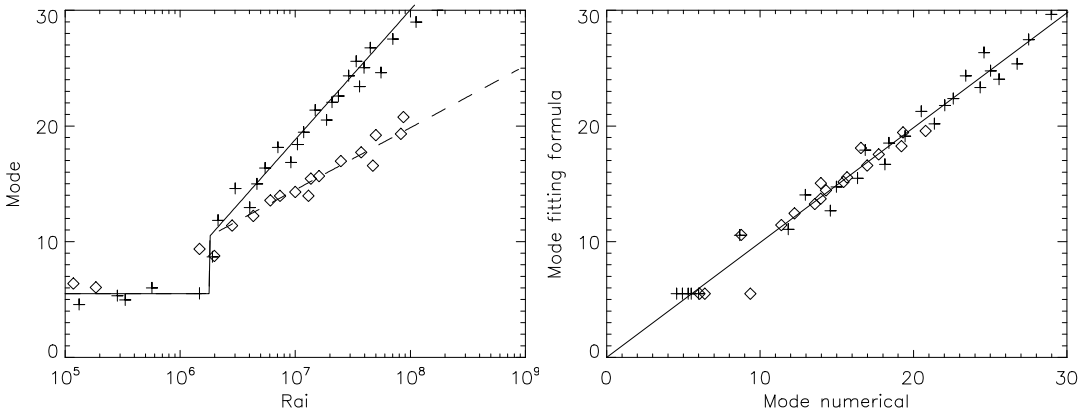

Figure 5.29. The correlation of the internal Rayleigh number to the weighted degree and the associated fitting lines, crosses represent TC and diamonds TPC stagnant-lid cases.

As a consequence of the mode increase after the transition to the time-dependent regime, the observed temporal standard deviation of the velocity must show a significant increase for $\omega > \omega_{min} + \omega_{step}$, as demonstrated in figure 5.30. The standard deviation of the temporal volume-averaged velocity is an indicator for the time-dependency of a convective system, so a higher value means more turbulent convection (down- and upwellings do not stay spatially fixed, e.g., Hansen et al. (1992b)). This leads to the conclusion that beyond $\omega \gtrsim 10$, convection is time-dependent in the stagnant-lid regime.

	Ra_{S-T}	ω_{step}	m	ω_{min}	χ^2
TC	2.07e6	5	5.12	5.5	0.055
TPC	2.07e6	5	2.23	5.5	0.047

Table 5.4. The result of a complete inversion of stagnant-lid cases for equation 5.39. Grayed values indicate copies from TC due to insufficient data.

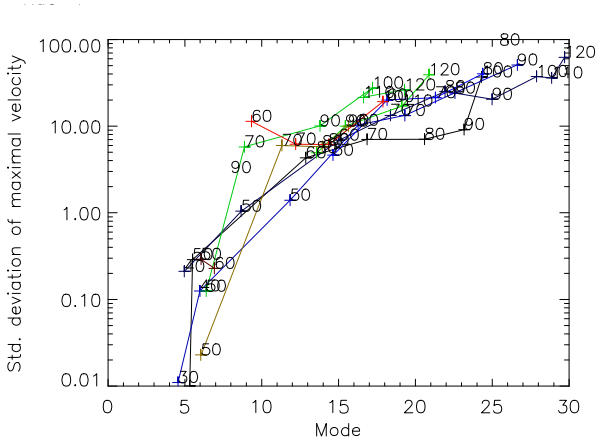

Figure 5.30. The correlation of degrees to the standard deviation of the maximal velocity. The latter indicates time-dependent behavior in the stagnant-lid regime. Lines connect similar surface Rayleigh numbers and the values on the marks indicate the rheological parameter γ.

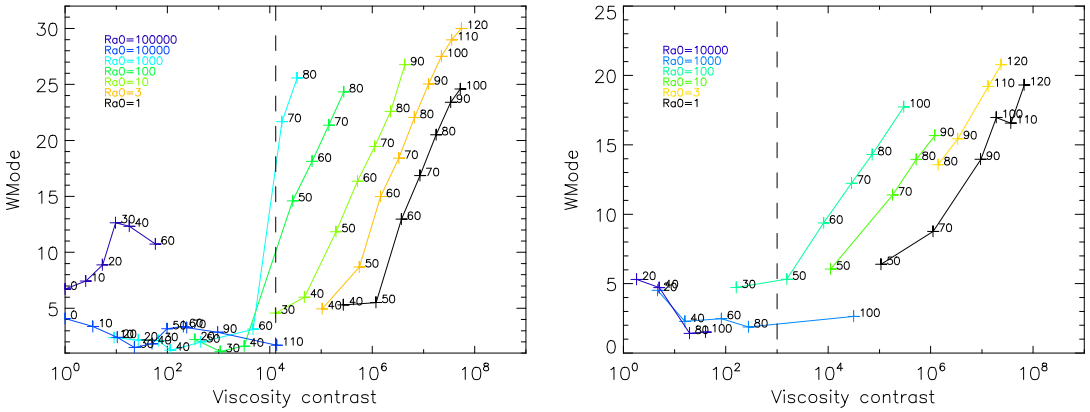

Figure 5.31. The weighted mode ω over the viscosity contrast for all TC on the left figure and TPC on the right. The dashed vertical line marks the transition to the stagnant-lid regime.

6 Conclusions

This work introduces a new method to simulate mantle convection in a spherical shell with fully spatially varying viscosities. The intention of this numerical model is to run simulations with closer-to-reality parameters and therefore to study the thermal evolution of planetary mantles in great detail. The formulation of the governing equations are based on the finite-volume method with the advantage of utilizing fully irregular grids in three and two dimensions, efficiently parallelized for up to 396 CPUs. While being capable of using common grids such as projected icosahedra and the cubed sphere grid, an irregular grid which has the advantage of laterally varying resolutions, the spiral grid, was investigated. In essence any set of nodal positions can, after a Voronoi tessellation that forms the necessary cells for the FV formulation, be used as a basis for the discretization. The model is based on the Cartesian reference frame and utilizes a co-located variable arrangement that holds all unknowns at the defined nodal positions. To ensure a divergence free velocity field, the SIMPLE method (see section 3.3) was employed to ensure mass continuity with a correction of pressure. The discretization method is of second-order and time integration is treated fully implicitly. A fully implicit treatment has the advantage of solving steady-state solutions with large time-steps while also solving strongly time-dependent problems with small time-steps. The discretization of the stress tensor is capable of handling viscosity variations of up to 8 orders of magnitude from cell-to-cell and up to 45 orders of magnitude system wide. The model was validated by a comparison with analytically known solutions as well as published results. A comparison with a commercial product also yielded satisfying results. Variables of primary interest for the benchmarks were global quantities, i.e. the Nusselt number, the volume averaged temperature and velocity as well as local quantities such as maxima / minima of mid-shell temperature and velocity. A convergence test with successively refined grids proved the convergence of global quantities towards an extrapolated solution. Quantitative measures of three-dimensional spherical mantle convection are sporadic but the simulations presented here only vary a few percent with published results and contribute to further benchmarks.

As an application to mantle convection, the model was applied to a parameter study of 88 cases to obtain scaling laws for purely internally heated convection in a spherical shell. The aspect ratio was fixed to 0.55, similar to the value of the Earth. The rheology law is based on a linearized Arrhenius law, commonly known as the Frank-Kamenetskii approximation. Three regimes of convection that were explored with bottom-heated convection in previous studies could also be identified with purely internally heated convection. A fourth regime, the low-degree-regime that occurs instead of the sluggish regime could also be identified. This new regime results in long wave-

lengths (below degree three) in the same parametric range as the sluggish regime for bottom heated convection. The surface is completely mobile and the transition to the stagnant-lid regime is rather abrupt. Present and newly developed indicators for the different regimes were validated to distinguish between them as this is the first parametric study that follows the transition of the regimes with purely internally heated convection in a spherical shell.

Numerical simulations in three-dimensions using Cartesian box geometries with large aspect ratios (e.g., Tackley, 1996b, Ratcliff *et al.*, 1997, Trompert and Hansen, 1996) and spherical shell geometries (e.g., Ratcliff *et al.*, 1996b, Ratcliff *et al.*, 1996a) show the formation of a highly viscous layer close to the surface with stress-free boundary conditions when the viscosity contrast due to temperature reaches a value between $10^4 - 10^5$. This layering mechanism was observed and studied in section 5.2. In contrast to the numerous small scale plumes surrounded by sheet-like downwellings observed with bottom heated convection (e.g., Ratcliff *et al.*, 1996a, 1996b), purely internally heated convection forms opposite structures: plume like downwellings below the stagnant-lid, similar to raindrops forming on a condensed plate combined with sheet like upwellings (e.g., Parmentier *et al.*, 1994, Reese *et al.*, 2005).

The thermal boundary layer was analyzed with established and new methods to obtain scaling laws for the heat-flow and the thickness of the stagnant-lid that occurs as the viscosity contrast becomes higher than five orders of magnitude. The viscosity of the cold upper material becomes large and the material becomes stiff and immobile. A 'stagnant-lid' forms where heat is only transported by conduction. This stagnant-lid is especially interesting for planetary evolutions as its thickness can reveal properties of the planetary crust and the overall heat budget. The boundary layer that is below this lid or directly below the surface for mobile regimes reveals the temperature of the convecting interior and the strength of convection, usually expressed as the Nusselt number. Scaling laws help to quickly calculate these quantities to avoid time consuming computations of three-dimensional simulations.

With the number of cases in the stagnant-lid regime, it was possible to obtain a full inversion of the classical three-parameter fit in the form of $Nu = a\,\theta^{\alpha}\,Ra_{H,i}^{\beta}$ (Solomatov, 1995). In previous studies the exponent β was fixed to $1/3^{\text{rd}}$ obtained from boundary layer theory of isoviscous, bottom heated free-slip convection. Grasset and Parmentier (1998) and Reese (2005) argued that the three parameter fit does not hold for strongly temperature-dependent viscosity in purely internally heated convection models. However, they could not perform a full inversion because of an insufficient number of cases. In the present study, a full inversion yielded satisfying results but with β close to $1/5^{\text{th}}$. This offset from the theoretical value of $1/4^{\text{th}}$ for steady-state, free-slip and purely internally heated convection is reasonable considering that the boundary conditions for the velocity strongly influence this value: although free-slip

boundary conditions are assumed at the surface and bottom, the flow below the stagnant-lid 'experiences' a mixed boundary condition between free-slip and no-slip. Furthermore, the free-slip condition at the lower boundary is altered in the presence of pressure dependence because the viscosity increases with depth. In a first approximation the viscosity increase changes the free-slip condition at the bottom towards a no-slip boundary condition. As the consequence of the changing boundary conditions for the mantle flow, a value of β from theory for either free-slip or no-slip is not necessarily valid in this scaling law.

An alternative way to parameterize the heat transport of a mantle flow with temperature-dependent viscosity was first suggested by Solomatov (1993, 1995), later confirmed by Davaille and Jaupart (1993) with laboratory experiments for internally heated convection and by Grasset and Parmentier (1998) and Reese et al. (1999a, 2005) through numerical simulations. The authors argue that the temperature drop within the thermal boundary layer below the stagnant-lid can be described by the rheological gradient γ in the way that $\Delta T_{rh} = T_i - T_L = a_{rh}\gamma^{-1}$ where a_{rh} is the rheological constant, T_i the temperature of the convecting interior and T_L the temperature at the bottom of the lid δ_L. The whole system is divided into two layers: a purely conducting layer, i.e. the stagnant-lid, and an almost isoviscous convecting layer below. In the present study, both regimes, i.e. the steady-state and time-dependent temporal regimes, have been examined for the convecting interior. . As only the isovisous mantle is considered, the scaling law is reduced to $Nu = a\, Ra^{\beta}$ and yielded expected results with β close to $1/3^{rd}$ for steady-state cases and close to $1/5^{th}$ for time-dependent cases. Although Grasset and Parmentier (1998) and Parmentier et. al. (1994) used isoviscous convection models to constrain the a and β parameter for this fit, the rescaling method with a measured lid thickness used in this study resulted in similar parameters (section 5.6.2). Since both of the compared studies use a top-no-slip model and result in similar parameters, the convection beneath the stagnant-lid is presumably isoviscous convection with a no-slip top boundary condition. Furthermore, the difference between their 2D and 3D boxed simulations and the present 3D spherical study suggests that for time-dependent **isoviscous** convection the geometry plays a minor role. This is different for the rheology constant a_{rh} that determines in combination with the rheological gradient γ the temperature drop across the thermal boundary layer: a difference of 23% was observed to the results of Grasset and Parmentier (1998) ($a_{rh} = 2.23$ compared to 2.88 in this study), causing an error in lid-thickness determination and internal temperature of about 10%.

However, in a complete inversion of the rather complex equations (see section 5.6.2) all three free parameters, namely the rheological constant a_{rh}, the factor a and the exponent β have been determined. This inversion reveals not only one solution but a larger parameter space for all three variables. With other words, for a specific rheological constant a_{rh} the other two free parameters can be chosen with almost no differ-

ence in the resulting error. A relation between the paramters has been recognized already in earlier studies (Grasset and Parmentier, 1998, Solomatov and Moresi, 2000a, Reese *et al.*, 2005) but these authors finally assume a value of beta derived from theoretical and isoviscous studies and then determine a and arh. A variation in the parameters may be relevant assuming different levels of erosion of the stagnant-lid, i.e., the larger a_{rh}, the thinner is the lid and vice versa. This delamination mechanism could be useful in combination with the initiation of continental rifting based on a thinning lithosphere (Spohn and Schubert, 1982).

Apart from updated scaling laws, a new method was developed to reconstruct the complete heat-flow profile, and therefore temperature, as a radial function with parameterized incomplete gamma functions. The heat-flow profile can be expressed as a fraction between the conductive and the convective heat flux. Within the convecting interior, this fraction is almost zero because convection is the dominant heat transport mechanism, while close to the surface this value becomes one as conduction is the main heat transport mechanism. This depth profile shows a relatively sharp transition from zero to one for purely internally heated convection where the convective heat-flow is changed into conductive. This transition zone is equivalent to the thermal boundary layer. With the known theoretical heat-flow profile of pure conduction, it is possible to reconstruct the complete temperature profile by knowing the exact properties of this transition. It is further possible to obtain important parameters like the temperature of the convecting interior and the lid thickness. Several step functions were tested and the incomplete gamma function yielded an excellent fit for this transition zone with only two parameters, capable of retrieving the heat-flow profile for all regimes. Unfortunately these two parameters have no physical meaning, so an attempt was made to constrain scaling laws from the Rayleigh number and the rheological gradient γ. A successful three parameter fit could be established for the stagnant-lid regime, yielding excellent results for the interior temperature, making this new method the preferred choice for scaling analysis of the temperature / heat-flow profile. The obtained parameters are only valid for internally heated convection; however, further studies could reveal an application to several other heating modes as well.

Apart from the scaling laws for the internal temperature, heat-flow and the stagnant-lid thickness also the pattern of mantle convection has been parameterized. The convection pattern or the degree of the convection structure is a helpful parameter to constrain convection models of the terrestrial planets as the degree of convection structure is one important observable. This can be obtained by seismic tomography models and also indirectly from the structures at the planet's surface. Interestingly, for Earth, Mars and the Moon a low-degree convection pattern is suggested. For the Earth this has been found by seismic tomography models (Masters *et al.*, 1996, Grand *et al.*, 1997). Moreover, the formation of supercontinents on the Earth hints at the fact that an even lower degree flow structure than observed today may have once existed in the

past (e.g., Gurnis, 1988, Zhong *et al.*, 2007). For both Mars and the Moon even a degree-one mantle flow structure (consisting of one upwelling and one downwelling) may have existed on these bodies resulting in the observed hemispherical crustal dichotomy and the Tharsis rise on Mars (e.g., Wise *et al.*, 1979, Harder and Christensen, 1996) and the hemispherical distribution of Mare basalts on the Moon (Zhong *et al.*, 2000a). Degree-one convection is an interesting field of study as it has the longest possible wavelength of the flow and implies many geological consequences.

Within the stagnant-lid regime for terrestrial planets, a relation between the internal Rayleigh number and a structural indicator, the weighted mode, was identified. The weighted or dominant mode increases linearly with the internal Rayleigh number. The weighted mode is an indicator close to the dominant degree on which one is able to determine e.g. the average area that a plume covers on the surface. The correlation was identified for the time-dependent stagnant-lid regime; whereas for steady-state degree five seems to be the lowest possible mode beneath the stagnant-lid (Figure 5.29 in section 3.7.1 illustrates the presence of that lower limit for stagnant-lid convection). The limit is not affected by the presence of pressure dependence. Note that, however, this lower limit is bound to the employed radius ratio of 0.55 and is likely to be lower with a smaller core and can easily be influenced by different rheology laws (see below).

It is interesting to note that, in comparison to isoviscous convection, the same internal Rayleigh number produces in the presence of a stagnant-lid flow structures with lower wavelengths. This is valid for all heating modes (e.g., Reese *et al.*, 2005, Stemmer *et al.*, 2006, Zhong *et al.*, 2008). These convection patterns with high-degree modes are apparently inconsistent with planetary observations. The dynamical effects of a stratified viscosity profile on the pattern of mantle convection without lateral viscosity variations have been studied by the two-dimensional (2-D) or 3-D Cartesian (e.g., Hansen *et al.*, 1993, Tackley, 1996b) and by the spherical shell models (e.g., Zhang and Yuen, 1996, Bunge and Richards, 1996, Bunge *et al.*, 1997, Zhong *et al.*, 2000b). Bunge et al. (1996, 1997) and Harder (2000) have shown that a modest increase in the mantle viscosity with depth has a remarkable effect on the convection pattern, resulting in a long-wavelength structure up to degree-one flow. However, another important factor for the mantle viscosity, i.e., the strong dependence on temperature, was absent in their models. In contrast to the observations by Bunge et al. (1996, 1997) and Harder (2000), the influence of pressure dependence in this parameter study did not lead to longer wavelengths flow patterns (see section 5.7) and the range of degree-one occurrences seems to be unchanged. On the other hand, the behavior in the time-dependent stagnant-lid regime with additional pressure dependency does indeed lead to lower modes than its counterpart with only temperature-dependent viscosity for the same internal Rayleigh number (see previous section). The depth dependence as an additional factor among more complex scenarios is reported to reduce, although not significantly, the mode as well (e.g., Tackley, 1996a, Zhong and Zuber, 2001).

An essential question is whether observed low degree mantle flow results from the material properties of the mantle (i.e., phase transitions, chemical heterogeneity, and rheology) or whether it is caused by the complicated elasto-plastic rheology of the lithosphere. The presence of rigid plates or continents has been observed to also organize mantle flow into larger wavelengths (Davies, 1989, Gurnis and Zhong, 1991, Zhong and Gurnis, 1995). Degree-one convection is possible for planetary bodies with a relatively small core as well, as demonstrated by Zhong *et al.* (2000a) for the Moon and Grott et al. (2007) for Enceladus. Other terrestrial bodies with a larger core require different mechanisms. An increase of the flow wavelength for parameters relevant to Earth could be identified by incorporating phase changes into the numerical simulation (Tackley, 1996b). Phase changes in the Martian mantle may produce degree-one flow as well (Harder and Christensen, 1996, Breuer *et al.*, 1998, Harder, 2000).

Although the identified low-degree regime is rather unrealistic in terms of activation energy, it is a valid first-order approximation of mantle convection below a virtual thin lid or convection beneath a strong radial viscosity gradient that is necessary to establish the top free-slip boundary condition. McNamara and Zhong (2005a) focused on the effects of temperature-dependent rheology and internal heating whether convection develops a degree-one flow pattern. The parametric range of this study was used to find clues on what mechanisms are required to achieve a low-degree or degree-one flow structure. As McNamara and Zhong (2005a) reported ranges of activation parameters that lead to viscosity contrasts of 10^3 and 10^4, degree-one flow occurs only for cases in which internal heating is applied. This can be confirmed for purely internally heated convection, as figure 5.3 illustrates. The range of effective Rayleigh numbers to produce a degree-one flow pattern is limited, and completely restricted to the low-degree regime.

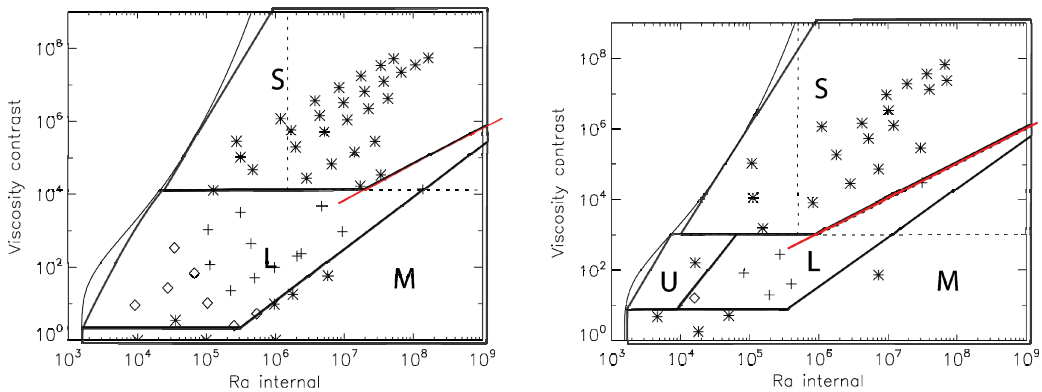

Figure 6.1. An alternative regime classification in the $Ra_{H,i}$ and $\Delta\eta$ parameter space, similar to figure 5.3, where S stands for stagnant-lid regime, L low-degree regime, U sluggish regime and M for the mobile regime. The red line marks the boundary where the surface Rayleigh number would exceed the critical Rayleigh number for isoviscous convection with free-slip boundaries.

Since the degree-one cases only occur in the low-degree regime, it is obvious that the boundary conditions, especially on the surface, play an important role in supporting low-degree convection. A free-slip boundary condition on top greatly facilitates low-degree convection and, as visible in figure 5.3, intermediate viscosity contrasts as most of them are close to the boundary to the stagnant-lid regime. However, it could not be excluded that the low-degree regime is restricted to intermediate viscosity contrasts (close to the boundary to the stagnant-lid). An alternative boundary to the stagnant-lid regime is possible if the surface Rayleigh number exceeds the critical Rayleigh number (Figure 6.1). Since this parameter space requires high viscosity contrasts and Rayleigh numbers, this possibility was not yet studied in earlier works. Hence, the appearance of low-degree convection would not be restricted to a certain viscosity contrast, as convection can benefit from the top free-slip boundary condition once the viscosity and the Rayleigh number allow mobility. Surface mobility is also given in the case of plate tectonics. Thus, the low degree observed for the Earth is likely to be associated with plate tectonics (e.g., Davies, 1988, Bunge *et al.*, 1998, Lithgow-Bertelloni and Richards, 1998).

Outlook

The present thesis provides new insights into the fluid-dynamical investigation of mantle convection and scaling laws. Apart from updated and newly derived scaling methods, the numerical scheme presented in chapter 3 is capable of handling realistic viscosity contrasts of up to 45 orders of magnitude. This allows for a study of the influence of Arrhenius viscosity instead of having to use the linearized Frank-Kamenetskii approximation. Future parameter studies using realistic activation energies and surface temperatures in combination with the Arrhenius viscosity law and realistic Rayleigh numbers would greatly improve our understanding of mantle convection in general and the accuracy of the previously applied Frank-Kamenetskii approximation in particular.

Concerning the parameter study presented in chapter 5, further parametrical exploration is necessary to constrain scaling laws for different modes of heating. While the present study focuses on the effects of purely internally heated convection, it is also important to look at mixed modes of heating, i.e., bottom heating in combination with internal heating should be investigated. In particular, scaling laws to constrain heat-flow and stagnant-lid properties should be derived. The new technique to reconstruct the entire heat-flow profile presented in section 5.6.3 is likely to be applicable in a more general way to different modes of heating and may be very useful concerning theoretical studies of fluid flow.

Bibliography

Agouzal, A., Baranger, J., Maitre, J.F. & Oudin, F., 1995. Connection between finite volume and mixed finite element methods for a diffusion problem with nonconstant coefficients. Application to a convection diffusion problem, *East-West Journal of Numerical Mathematics,* 3**,** 237-254.

Ahlers, G. & Xu, X., 2001. Prandtl-number dependence of heat transport in turbulent Rayleigh-Bénard convection, *Phys. Rev. Lett.,* 86**,** 3320-3323.

Alliez, P., De Verdihre, E.C., Devillers, O. & Isenburg, M., 2005. Centroidal Voronoi diagrams for isotropic surface remeshing, *Graphical Models,* 67**,** 204-231.

Babcock, R.W., 1930. Thermal convection, *Physical Review,* 35**,** 1008-1013.

Balay, S., Buschelman, K., Eijkhout, V., Gropp, W.D., D.Kaushik, Knepley, M.G., McInnes, L.C. & B.F. Smith, H.Z., 2004. PETSc users manual. *in ANL-95/11 - Revision 2.1.5*ANL, Argonne National Laboratory.

Baranger, J., Maitre, J.F. & Oudin, F., 1996. Connection between finite volume and mixed finite element methods, *Mathematical Modelling and Numerical Analysis,* 30**,** 445-465.

Barber, C.B., Dobkin, D.P. & Huhdanpaa, H., 1996. The Quickhull Algorithm for Convex Hulls, *ACM Transactions on Mathematical Software,* 22**,** 469-483.

Baumgardner, J.R., 1985. Three-dimensional treatment of convective flow in the earth's mantle, *Journal of Statistical Physics,* 39**,** 501-511.

Belashchenko, D., Kravchunovskaya, N. & Ostrovski, O., 2008. Properties of iron under Earth's core conditions: Molecular dynamics simulation with an embedded-atom method potential, *Inorganic Materials,* 44**,** 248-257.

Bénard, H., 1900. Les tourbillons cellulairs dans une nappe liquide, *Revue générale des Sciences pures et appliquées,* 11**,** 1261-1271.

Bercovici, D., Schubert, G. & Glatzmaier, G.A., 1989. Three-dimensional spherical models of convection in the earth's mantle, *Science,* 244**,** 950-955.

Bottaro, A., Metzener, P. & Matalon, M., 1992. Onset and two-dimensional patterns of convection with strongly temperature-dependent viscosity, *Physics of Fluids A,* 4**,** 655-663.

Braun, J. & Sambridge, M., 1995. A numerical method for solving partial differential equations on highly irregular evolving grids, *Nature,* 376**,** 655-660.

Breuer, D., Spohn, T. & Wu?llner, U., 1993. Mantle differentiation and the crustal dichotomy of Mars, *Planetary and Space Science,* 41**,** 269-283.

Breuer, D., Yuen, D.A., Spohn, T. & Zhang, S., 1998. Three dimensional models of Martian mantle convection with phase transitions, *Geophysical Research Letters,* 25**,** 229-232.

Breuer, M., Wessling, S., Schmalzl, J. & Hansen, U., 2004. Effect of inertia in Rayleigh-Bénard convection, *Phys. Rev. E,* 69**,** 026302.

Bunge, H.P. & Richards, M.A., 1996. The origin of large scale structure in mantle convection: Effects of plate motions and viscosity stratification, *Geophysical Research Letters,* 23**,** 2987-2990.

Bunge, H.P., Richards, M.A. & Baumgardner, J.R., 1996. Effect of depth-dependent viscosity on the planform of mantle convection, *Nature,* 379**,** 436-438.

Bunge, H.P., Richards, M.A. & Baumgardner, J.R., 1997. A sensitivity study of three-dimensional spherical mantle convection at 108 Rayleigh number: Effects of depth-dependent viscosity, heating mode, and an endothermic phase change, *Journal of Geophysical Research B: Solid Earth,* 102**,** 11991-12007.

Bunge, H.P., Richards, M.A., Lithgow-Bertelloni, C., Baumgardner, J.R., Grand, S.P. & Romanowicz, B.A., 1998. Time scales and heterogeneous structure in geodynamic earth models, *Science,* 280**,** 91-95.

Buske, M., 2006. Dreidimensionale thermische Evolutionsmodelle für das Innere von Mars und Merkur, Copernicus GmbH, Katlenburg-Lindau.

Busse, F.H., 1975. Patterns of convection in spherical shells, *J. Fluid Mech.,* 72**,** 67-85.

Busse, F.H., 1978. Non-linear properties of thermal convection, *Reports on Progress in Physics,* 41**,** 1929-1967.

Buttkus, B., 2000. *Spectral analysis and filter theory in applied geophysics,* edn, Vol., pp. Pages, Springer, Berlin; New York.

Caretto, L.S., Gosman, A.D., Patankar, S.V. & Spalding, D.B., 1972. *Two calculation procedures for steady, three-dimensional flows with recirculation,* edn, Vol., pp. Pages, Proc. Third Int. Conf. Numer. Methods Fluid Dyn., Paris.

Carey, V.P. & Mollendorf, J.C., 1980. VARIABLE VISCOSITY EFFECTS IN SEVERAL NATURAL CONVECTION FLOWS, *International Journal of Heat and Mass Transfer,* 23**,** 95-109.

Carlson, B.C., 2002. Three improvements in reduction and computation of elliptic integrals, *Journal of Research of the National Institute of Standards and Technology,* 107**,** 413-418.

Chandrasekhar, S., 1961. *Hydrodynamic and Hydromagnetic stability,* edn, Vol., pp. Pages, Dover, New York.

Choblet, G., 2005. Modelling thermal convection with large viscosity gradients in one block of the 'cubed sphere', *Journal of Computational Physics,* 205**,** 269-291.

Christensen, U., 1983. Convection in a variable-viscosity fluid: Newtonian versus power- law rheology, *Earth & Planetary Science Letters,* 64**,** 153-162.

Christensen, U., 1984a. Convection with pressure- and temperature-dependent non-Newtonian rheology, *Geophysical Journal-Royal Astronomical Society,* 77**,** 343-384.

Christensen, U. & Harder, H., 1991. 3-D convection with variable viscosity, *Geophysical Journal International,* 104**,** 213-226.

Christensen, U.R., 1984b. Heat transport by variable viscosity convection and implications for the Earth's thermal evolution, *Physics of the Earth & Planetary Interiors,* 35**,** 264-282.

Courbebaisse, G., 2008. A comparison between the software COMSOL(C) and a lattice Boltzmann code when simulating behaviour of viscous material. *in European COST P19 project, CONFERENCE on Multiscale Modelling of Materials*, Brno, Academy of Sciences - Masaryk University, Czech Republic.

Craik, A.D.D., 2000. Transitions between roll patterns in thermal convection, *Fluid Dynamics Research,* 26**,** 305-323.

Crank, J. & Nicolson, P., 1947. A Practical Method for the Numerical Evaluation of Solutions of Partial Differential Equations of the Heat Conduction Type, *Proc. Combridge Phil. Soc.***,** 43-50.

Davaille, A. & Jaupart, C., 1993. Transient high Rayleigh number thermal convection with large viscosity variations, *Journal of Fluid Mechanics,* 253**,** 141-166.

Davies, G.F., 1980. Thermal histories of convective earth models and constraints on radiogenic heat production in the earth, *Journal of Geophysical Research,* 85**,** 2517-2530.

Davies, G.F., 1988. Role of the lithosphere in mantle convection, *Journal of Geophysical Research,* 93.

Davies, G.F., 1989. Mantle convection model with a dynamic plate: topography, heat-flow and gravity anomalies, *Geophysical Journal International,* 98**,** 461-464.

Deschamps, F. & Sotin, C., 2000. Inversion of two-dimensional numerical convection experiments for a fluid with a strongly temperature-dependent viscosity, *Geophysical Journal International,* 143**,** 204-218.

Du, Q., Faber, V. & Gunzburger, M., 1999. Centroidal Voronoi tessellations: Applications and algorithms, *SIAM Review,* 41**,** 637-676.

Du, Q. & Gunzburger, M., 2002. Grid generation and optimization based on centroidal Voronoi tessellations, *Applied Mathematics and Computation (New York),* 133**,** 591-607.

Dumoulin, C., Doin, M.P. & Fleitout, L., 1999. Heat transport in stagnant-lid convection with temperature- and pressure-dependent Newtonian or non-Newtonian rheology, *Journal of Geophysical Research B: Solid Earth,* 104**,** 12759-12777.

Ferziger, J.H. & Perić, M., 1999. *Computational Methods for Fluid Dynamics,* edn, Vol., pp. Pages, Springer Berlin, second edition, Berlin.

Fish, J., Qu, Y. & Suvorov, A., 1999. Towards Robust Two-level Methods for Indefinite Systems, *International journal for numerical methods in engineering.,* 45**,** 1433.

Fletcher, C.A.J., 1991. *Computational techniques for fluid dynamics,* 2 edn, Vol. 2, pp. Pages, Springer, Berlin.

Fowler, A.C., 1993. Boundary layer theory and subduction, *Journal of Geophysical Research,* 98.

Frank-Kamenetskii, D.A., 1969. *Diffusion and heat transfer in chemical kinetics,* edn, Vol., pp. Pages, Plenum Press, New York.

Furbish, D.J., 1997. Fluid physics in geology: An introduction to fluid motions on Earth surface and within its crust.

Futterer, B., Gellert, M., von Larcher, T. & Egbers, C., 2008. Thermal convection in rotating spherical shells: An experimental and numerical approach within GeoFlow, *Acta Astronautica,* 62**,** 300-307.

Giannandrea, E. & Christensen, U., 1993. Variable viscosity convection experiments with a stress-free upper boundary and implications for the heat transport in the Earth's mantle, *Physics of the Earth and Planetary Interiors,* 78**,** 139-152.

Glatzmaier, G.A., 1988. Numerical simulations of mantle convection: Time-dependent, three-dimensional, compressible, spherical shell, *Geophys. Astro. Fluid,* 43**,** 223-264.

Glatzmaier, G.A., 1993. Highly supercritical thermal convection in a rotating spherical shell: centrifugal vs. radial gravity, *Geophysical and Astrophysical Fluid Dynamics,* 70**,** 113-136.

Grand, S.P., Van Der Hilst, R.D. & Widiyantoro, S., 1997. Global seismic tomography: A snapshot of convection in the earth, *GSA Today,* 7.

Grasset, O. & Parmentier, E.M., 1998. Thermal convection in a volumetrically heated, infinite Prandtl number fluid with strongly temperature-dependent viscosity: Implications for planetary thermal evolution, *Journal of Geophysical Research B: Solid Earth,* 103**,** 18171-18181.

Grossmann, S. & Lohse, D., 2000. Scaling in thermal convection: A unifying theory, *Journal of Fluid Mechanics,* 407**,** 27-56.

Grott, M., Sohl, F. & Hussmann, H., 2007. Degree-one convection and the origin of Enceladus' dichotomy, *Icarus,* 191**,** 203-210.

Gurnis, M., 1988. Large-scale mantle convection and the aggregation and dispersal of supercontinents, *Nature,* 332**,** 695-699.

Gurnis, M. & Zhong, S., 1991. Generation of long wavelength heterogeneity in the mantle by the dynamic interaction between plates and convection, *Geophysical Research Letters,* 18**,** 581-584.

Hansen, U. & Ebel, A., 1984. Numerical and dynamical stability of convection cells in the Rayleigh number range 103-8.105, *Annales Geophysicae,* 2**,** 291-302.

Hansen, U. & Ebel, A., 1988. Time-dependent thermal convection - a possible explanation for a multiscale flow in the Earth's mantle, *Geophysical Journal,* 94**,** 181-191.

Hansen, U. & Yuen, D.A., 1990. Heat transport in strongly chaotic thermal convection. *in American Society of Mechanical Engineers, Heat Transfer Division, (Publication) HTD*, pp. 43-46.

Hansen, U. & Yuen, D.A., 1993. High Rayleigh number regime of temperature-dependent viscosity convection and the Earth's early thermal history, *Geophysical Research Letters,* 20**,** 2191-2194.

Hansen, U., Yuen, D.A. & Kroening, S.E., 1990. Transition to hard turbulence in thermal convection at infinite Prandtl number, *Physics of Fluids A,* 2**,** 2157-2163.

Hansen, U., Yuen, D.A. & Kroening, S.E., 1992a. Mass and heat transport in strongly time-dependent thermal convectinon at infinite Prandtl number, *Geophys. Astro. Fluid,* 63**,** 67-89.

Hansen, U., Yuen, D.A., Kroening, S.E. & Larsen, T.B., 1993. Dynamical consequences of depth-dependent thermal expansivity and viscosity on mantle circulations and thermal structure, *Physics of the Earth and Planetary Interiors,* 77**,** 205-223.

Hansen, U., Yuen, D.A. & Malevsky, A.V., 1992b. Comparison of steady-state and strongly chaotic thermal convection at high Rayleigh number, *Physical Review A,* 46**,** 4742-4754.

Harder, H., 1998. Phase transitions and the three-dimensional planform of thermal convection in the Martian mantle, *Journal of Geophysical Research E: Planets,* 103**,** 16775-16797.

Harder, H., 2000. Mantle convection and the dynamic geoid of Mars, *Geophysical Research Letters,* 27**,** 301-304.

Harder, H. & Christensen, U.R., 1996. A one-plume model of martian mantle convection, *Nature,* 380**,** 507-509.

Harder, H. & Hansen, U., 2005. A finite-volume solution method for thermal convection and dynamo problems in spherical shells, *Geophysical Journal International,* 161**,** 522-532.

Hauck, S.A. & Phillips, R.J., 2002. Thermal and crustal evolution of Mars, *Journal of Geophysical Research E: Planets,* 107**,** 6-1.

Hirayama, O. & Takaki, R., 1993. Thermal convection of a fluid with temperature-dependent viscosity, *Fluid Dynamics Research,* 12**,** 35-47.

Honda, S., 1996. Local Rayleigh and Nusselt numbers for cartesian convection with temperature-dependent viscosity, *Geophysical Research Letters,* 23**,** 2445-2448.

Ismail-Zadeh, A., Korotkii, A., Schubert, G. & Tsepelev, I., 2007. Quasi-reversibility method for data assimilation in models of mantle dynamics, *Geophysical Journal International,* 170**,** 1381-1398.

Iwase, Y., 1996. three-dimensional infinite prandtl number convection in a spherical shell with temperature-dependent viscosity, *Journal of Geomagnetism and Geoelectricity,* 48**,** 1499-1514.

Jarvis, G.T., 1993. Effects of curvature on two-dimensional models of mantle convection: cylindrical polar coordinates, *Journal of Geophysical Research,* 98**,** 4477-4485.

Jarvis, G.T., 1994. The unifying role of aspect ratio in cylindrical models of mantle convection with varying degrees of curvature, *Geophysical Journal International,* 117**,** 419-426.

Jarvis, G.T., Glatzmaier, G.A. & Vangelov, V.I., 1995. Effects of curvature, aspect ratio and plan form in two- and three- dimensional spherical models of thermal convection, *Geophysical & Astrophysical Fluid Dynamics,* 79**,** 147-171.

Ju, L., Du, Q. & Gunzburger, M., 2002. Probabilistic methods for centroidal Voronoi tessellations and their parallel implementations, *Parallel Computing,* 28**,** 1477-1500.

Kageyama, A. & Sato, T., 2004. 'Yin-Yang grid': An overset grid in spherical geometry, *Geochem. Geophys. Geosyst.,* 5**,** doi:10.1029/2004GC000734.

Karato, S., 1981. Rheology of the lower mantle, *Physics of the Earth and Planetary Interiors,* 24**,** 1-14.

Karato, S.I. & Wu, P., 1993. Rheology of the upper mantle: A synthesis, *Science,* 260**,** 771-778.

Kertz, W., 1973. *Potentialtheorie in der Geophysik,* edn, Vol., pp. Pages, Institut fÃ*f*Â¼r Geophysik u. Meteorologie der TU Braunschweig, Braunschweig.

Krishnamurti, R., 1970. On the transition to turbulent convection, Part 2: The transition to time-dependent flow, *J. Fluid Mech.,* 42**,** 309-320.

Lanczos, C., 1950. An Iteration Method for the Solution of the Eigenvalue Problem of Linear Differential and Integral Operators, *Journal of Research of the National Bureau of Standards,* 45**,** 255-282.

Lanczos, C., 1952. Solution of Systems of Linear Equations by Minimized Iterations, *Journal of the National Bureau of Standards,* 49**,** 33-53.

Lithgow-Bertelloni, C. & Richards, M.A., 1998. The dynamics of cenozoic and mesozoic plate motions, *Reviews of Geophysics,* 36**,** 27-78.

Lloyd, S., 1982. LEAST SQUARES QUANTIZATION IN PCM, *IEEE Transactions on Information Theory,* IT-28**,** 129-137.

Machetel, P., Rabinowicz, M. & Bernardet, P., 1986. Three-dimensional convection in spherical shells, *Geophys. Astro. Fluid,* 37**,** 57-84.

MacQueen, J., 1967. Some methods of classification and analysis of multivariate observations, *Proceedings of the 5th Berkeley Symposium on Math. Stat. and Prob. U*.

Masters, G., Johnson, S., Laske, G. & Bolton, H., 1996. A shear-velocity model of the mantle, *Philosophical Transactions of the Royal Society A: Mathematical, Physical and Engineering Sciences,* 354**,** 1385-1411.

McKenzie, D. & Richter, F.M., 1981. Parameterized thermal convection in a layered region and the thermal history of the earth, *Journal of Geophysical Research,* 86**,** 11667-11680.

McNamara, A.K. & Zhong, S., 2005a. Degree-one mantle convection: Dependence on internal heating and temperature-dependent rheology, *Geophysical Research Letters,* 32**,** 1-5.

McNamara, A.K. & Zhong, S., 2005b. Thermochemical structures beneath Africa and the Pacific Ocean, *Nature,* 437**,** 1136-1139.

Meister, A., 2005. *Numerik linearer Gleichungssysteme : eine EinfÃfÂ¼hrung in moderne Verfahren,* edn, Vol., pp. Pages, Vieweg, Wiesbaden.

Moresi, L.N. & Solomatov, V.S., 1995. Numerical investigation of 2D convection with extremely large viscosity variations, *Physics of Fluids,* 7**,** 2154-2162.

Morris, S. & Canright, D., 1984. A boundary-layer analysis of Bénard convection in a fluid of strongly temperature-dependent viscosity, *Physics of the Earth and Planetary Interiors,* 36**,** 355-373.

Nataf, H.C. & Richter, F.M., 1982. Convection experiments in fluids with highly temperature- dependent viscosity and the thermal evolution of the planets, *Physics of the Earth & Planetary Interiors,* 29**,** 320-329.

Normand, C., Pomeau, Y. & Velarde, M.G., 1977. Convection instability: A physicist's approach, *Rev. Mod. Phys.,* 49**,** 581-624.

Ogawa, M., 1995. Studies of mantle convection in Japan, *Journal of Physics of the Earth,* 43**,** 505-513.

Ogawa, M., Schubert, G. & Zebib, A., 1990. Numerical simulations of 3-D thermal convection of a strongly temperature-dependent viscosity fluid. *in American Society of Mechanical Engineers, Heat Transfer Division, (Publication) HTD*, pp. 1-5.

Ogawa, M., Schubert, G. & Zebib, A., 1991. Numerical simulations of three-dimensional thermal convection in a fluid with strongly temperature-dependent viscosity, *Journal of Fluid Mechanics,* 233**,** 299-328.

Okabe, A., Boots, B., Sugihara, K. & Chiu, S.K., 2000. *Spatial Tessellations: Concepts and Applications of Voronoi Diagrams,* edn, Vol., pp. Pages, Wiley.

Parmentier, E.M., 1978. STUDY OF THERMAL CONVECTION IN NON-NEWTONIAN FLUIDS, *Journal of Fluid Mechanics,* 84**,** 1-11.

Parmentier, E.M., Sotin, C. & Travis, B.J., 1994. Turbulent 3-D thermal convection in an infinite Prandtl number, volumetrically heated fluid: implications for mantle dynamics, *Geophysical Journal International,* 116**,** 241-251.

Patankar, S.V., 1980. *Numerical heat transfer and fluid flow,* edn, Vol., pp. Pages, McGraw-Hill, New York.

Peltier, W.R. & Jarvis, G.T., 1982. Whole mantle convection and the thermal evolution of the Earth, *Physics of the Earth & Planetary Interiors,* 29**,** 281-304.

Perić, M., Kessler, R. & Scheuerer, G., 1988. Comparison of finite-volume numerical methods with staggered and colocated grids, *Computers and Fluids,* 16**,** 389-403.

Ratcliff, J.T., Schubert, G. & Zebib, A., 1995. Three-dimensional variable viscosity convection of an infinite Prandtl number Boussinesq fluid in a spherical shell, *Geophysical Research Letters,* 22**,** 2227-2230.

Ratcliff, J.T., Schubert, G. & Zebib, A., 1996a. Effects of temperature-dependent viscosity on thermal convection in a spherical shell, *Physica D: Nonlinear Phenomena,* 97**,** 242-252.

Ratcliff, J.T., Schubert, G. & Zebib, A., 1996b. Steady tetrahedral and cubic patterns of spherical shell convection with temperature-dependent viscosity, *Journal of Geophysical Research B: Solid Earth,* 101**,** 25473-25484.

Ratcliff, J.T., Tackley, P.J., Schubert, G. & Zebib, A., 1997. Transitions in thermal convection with strongly variable viscosity, *Physics of the Earth and Planetary Interiors,* 102**,** 201-212.

Rayleigh, L., 1916. On convective currents in a horizontal layer of fluid when the higher temperature is on the under side, *Phil. Mag.,* 32**,** 529-546.

Reese, C.C., Solomatov, V.S. & Baumgardner, J.R., 2005. Scaling laws for time-dependent stagnant-lid convection in a spherical shell, *Physics of the Earth and Planetary Interiors,* 149**,** 361-370.

Reese, C.C., Solomatov, V.S., Baumgardner, J.R. & Yang, W.S., 1999a. Stagnant-lid convection in a spherical shell, *Physics of the Earth and Planetary Interiors,* 116**,** 1-7.

Reese, C.C., Solomatov, V.S. & Moresi, L.N., 1999b. Non-Newtonian Stagnant-lid Convection and Magmatic Resur facing on Venus, *Icarus,* 139**,** 67-80.

Richter, F.M., 1978. EXPERIMENTS ON THE STABILITY OF CONVECTION ROLLS IN FLUIDS WHOSE VISCOSITY DEPENDS ON TEMPERATURE, *J Fluid Mech,* 89**,** 553-560.

Richter, F.M., Daly, S.F. & Nataf, H.C., 1982. A parameterized model for the evolution of isotopic heterogeneities in a convecting system, *Earth and Planetary Science Letters,* 60**,** 178-194.

Roberts, J.H. & Zhong, S., 2006. Degree-1 convection in the Martian mantle and the origin of the hemispheric dichotomy, *Journal of Geophysical Research E: Planets,* 111.

Saad, Y., 1996. *Iterative methods for sparse linear systems,* edn, Vol., pp. Pages, PWS Pub. Co., Boston.

Sambridge, M., Braun, J. & McQueen, H., 1995. Geophysical parametrization and interpolation of irregular data using natural neighbours, *Geophysical Journal International,* 122**,** 837-857.

Schroeder, D.V., 2000. *An introduction to thermal physics,* edn, Vol., pp. Pages, Addison-Wesley, San Francisco, California.

Schubert, G., 1979. Subsolidus convection in the mantles of terrestrial planets, *Annual review of earth and planetary sciences, Vol. 7***,** 289-342.

Schubert, G., 1992. Numerical models of mantle convection, *Annual Review of Fluid Mechanics,* 24**,** 359-394.

Schubert, G., Bercovici, D. & Glatzmaier, G.A., 1990. Mantle dynamics in Mars and Venus: influence of an immobile lithosphere on three-dimensional mantle convection, *Journal of Geophysical Research,* 95.

Schubert, G. & Spohn, T., 1981. Two-layer mantle convection and the depletion of radioactive elements in the lower mantle, *Geophysical Research Letters,* 8**,** 951-954.

Schubert, G. & Spohn, T., 1990. Thermal history of Mars and the sulfur content of its core, *Journal of Geophysical Research,* 95.

Schubert, G., Stevenson, D. & Cassen, P., 1980. Whole planet cooling and the radiogenic heat source contents of the earth and moon, *Journal of Geophysical Research,* 85**,** 2531-2538.

Schubert, G., Turcotte, D.L. & Olson, P., 2001. *Mantle convection in the Earth and planets,* edn, Vol., pp. Pages, Cambridge Univ. Press.

Schubert, G. & Zebib, A., 1980. Thermal convection of an internally heated infinite Prandtl number fluid in a spherical shell, *Geophys. Astro. Fluid,* 15**,** 65-90.

Sharpe, H.N. & Peltier, W.R., 1979. A thermal history model for the Earth with parameterized convection, *Geophysical Journal, Royal Astronomical Society,* 59**,** 171-203.

Shepard, D., 1968. Two-dimensional interpolation function for irregularly-spaced data. *in Proceedings of the 23rd National Conference*, pp. 517–524.

Sleijpen, G.L.G. & van der Vorst, H.A., 1995. Maintaining convergence properties of BiCGstab methods in finite precision arithmetic, *Numerical Algorithms,* 10**,** 203-223.

Sleijpen, G.L.G., van der Vorst, H.A. & Fokkema, D.R., 1994. BiCGstab(l) and other hybrid Bi-CG methods, *Numerical Algorithms,* 7**,** 75-109.

Sohl, F. & Spohn, T., 1997. The interior structure of Mars: Implications from SNC meteorites, *Journal of Geophysical Research E: Planets,* 102**,** 1613-1635.

Solomatov, V.S., 1993. Parameterization of temperature- and stress-dependent viscosity convection and the thermal evolution of Venus, *Flow and creep in the solar system: observations, modeling and theory***,** 131-145.

Solomatov, V.S., 1995. Scaling of temperature- and stress-dependent viscosity convection, *Physics of Fluids,* 7**,** 266-274.

Solomatov, V.S. & Moresi, L.-N., 1996. Stagnant-lid convection on Venus, *Journal of Geophysical Research E: Planets,* 101**,** 4737-4753.

Solomatov, V.S. & Moresi, L.-N., 2000a. Scaling of time-dependent stagnant-lid convection: Application to small-scale convection on the Earth and other terrestrial planets, *J. Geophys. Res.,* 105**,** 21795-21818.

Solomatov, V.S. & Moresi, L.N., 1997. Three regimes of mantle convection with non-Newtonian viscosity and stagnant-lid convection on the terrestrial planets, *Geophysical Research Letters,* 24**,** 1907-1910.

Solomatov, V.S. & Moresi, L.N., 2000b. Scaling of time-dependent stagnant-lid convection: Application to small-scale convection on Earth and other terrestrial planets, *Journal of Geophysical Research B: Solid Earth,* 105**,** 21795-21817.

Sotin, C. & Labrosse, S., 1999. Three-dimensional thermal convection in an iso-viscous, infinite Prandtl number fluid heated from within and from below: Applications to the transfer of heat through planetary mantles, *Physics of the Earth and Planetary Interiors,* 112**,** 171-190.

Spiegel, E.A. & Veronis, G., 1960. On the Boussinesq approximation for a compressible fluid, *Astrophys. J.,* 131**,** 442-447.

Spohn, T. & Schubert, G., 1982. Convective thinning of the lithosphere: a mechanism for the initiation of continental rifting, *Journal of Geophysical Research,* 87**,** 4669-4681.

Spohn, T., Sohl, F. & Breuer, D., 1997. Mars, *Astronomy and Astrophysics Review,* 8**,** 181-236.

Stein, C., Schmalzl, J. & Hansen, U., 2004. The effect of rheological parameters on plate behaviourin a self-consistent model of mantle convection, *Physics of the Earth and Planetary Interiors,* 142**,** 225-255.

Stemmer, K., Harder, H. & Hansen, U., 2006. A new method to simulate convection with strongly temperature- and pressure-dependent viscosity in a spherical shell:

Applications to the Earth's mantle, *Physics of the Earth and Planetary Interiors,* 157**,** 223-249.

Sunday, D., 2002. Fast polygon area and Newell normal computation, *Journal of Graphics Tools,* 7**,** 9-13.

Tabata, M. & Suzuki, A., 2000. Stabilized finite element method for the Rayleigh-Bénard equations with infinite Prandtl number in a spherical shell, *Computer Methods in Applied Mechanics and Engineering,* 190**,** 387-402.

Tabata, M. & Suzuki, A., 2001. Mathematical modeling and numerical simulation of Earth's mantle convection, *Series in Mathematics 2001,* 6**,** 221-231.

Tackley, P.J., 1993. Effects of strongly temperature-dependent viscosity on time-dependent, three-dimensional models of mantle convection, *Geophysical Research Letters,* 20**,** 2187-2190.

Tackley, P.J., 1996a. Effects of strongly variable viscosity on three-dimensional compressible convection in planetary mantles, *Journal of Geophysical Research B: Solid Earth,* 101**,** 3311-3332.

Tackley, P.J., 1996b. On the ability of phase transitions and viscosity layering to induce long wavelength heterogeneity in the mantle, *Geophysical Research Letters,* 23**,** 1985-1988.

Tackley, P.J., 1998. Self-consistent generation of tectonic plates in three-dimensional mantle convection, *Earth and Planetary Science Letters,* 157**,** 9-22.

Tackley, P.J., 2000a. Mantle convection and plate tectonics: Toward an integrated physical and chemical theory, *Science,* 288**,** 2002-2007.

Tackley, P.J., 2000b. Self-consistent generation of tectonic plates in time-dependent, three-dimensional mantle convection simulations, 2. Strain weakening and asthenosphere, *Geochem. Geophys. Geosyst.,* 1(8)**,** doi:10.1029/2000GC000043.

Tackley, P.J., Stevenson, D.J., Glatzmaier, G.A. & Schuber, G., 1993. Effects of an endothermic phase transition at 670 km depth in a spherical model of convection in the Earth's mantle, *Nature,* 361**,** 699-704.

Tang, L.Q. & Tsang, T.T.H., 1997. Temporal, spatial and thermal features of 3-D Rayleigh-Be?nard convection by a least-squares finite element method, *Computer Methods in Applied Mechanics and Engineering,* 140**,** 201-219.

Thomson, J.J., 1904. On the Structure of the Atom: an Investigation of the Stability and Periods of Oscillation of a number of Corpuscles arranged at equal intervals around the Circumference of a Circle; with Application of the Results to the Theory of Atomic Structure, *Philosophical Magazine Series 6,* 7**,** 237-265.

Tozer, D.C., 1972. The present thermal state of the terrestrial planets, *Phys. Earth Planet. In.,* 6**,** 182-197.

Travis, B., Olson, P. & Schubert, G., 1990. Transition from two-dimensional to three-dimensional planforms in infinite-Prandtl-number thermal convection, *Journal of Fluid Mechanics,* 216**,** 71-91.

Travnikov, V., Brasch, W. & Egbers, C., 2000. The natural convection in a spherical shell, *ZAMM Zeitschrift fur Angewandte Mathematik und Mechanik,* 80.

Tritton, D.J., 1988. *Physical Fluid Dynamics,* edn, Vol., pp. Pages, Oxford Univ. Press.

Trompert, R. & Hansen, U., 1998a. Mantle convection simulations with rheologies that generate plate-like behaviour, *Nature,* 395**,** 686-689.

Trompert, R.A. & Hansen, U., 1996. The application of a finite volume multigrid method to three-dimensional flow problems in a highly viscous fluid with a variable viscosity, *Geophysical and Astrophysical Fluid Dynamics,* 83**,** 261-291.

Trompert, R.A. & Hansen, U., 1998b. On the Rayleigh number dependence of convection with a strongly temperature-dependent viscosity, *Physics of Fluids,* 10**,** 351-360.

Turcotte, D.L., 1979. Convection, *Reviews of Geophysics and Space Physics,* 17**,** 1090-1098.

Turcotte, D.L. & Schubert, G., 1982. *Geodynamics: Applications of continuum physics to geological problems,* edn, Vol., pp. Pages, John Wiley, New York.

Vacquier, V., 1998. A theory of the origin of the Earth's internal heat, *Tectonophysics,* 291**,** 1-7.

Wales, D.J. & Ulker, S., 2006. Structure and dynamics of spherical crystals characterized for the Thomson problem, *Physical Review B - Condensed Matter and Materials Physics,* 74.

Wang, M.M.T. & Sheu, T.W.H., 1997. An element-by-element BICGSTAB iterative method for three-dimensional steady Navier-Stokes equations, *Journal of Computational and Applied Mathematics,* 79**,** 147-165.

Weertman, J., 1970. The creep strength of the Earth's mantle, *Rev Geophys Space Phys,* 8**,** 145-168.

Weinstein, S.A., 1995. The effect of a deep mantle endothermic phase change on the structure of thermal convection in silicate planets, *Journal of Geophysical Research,* 100.

Wise, D.U., Golombek, M.P. & McGill, G.E., 1979. Tharsis province of Mars: Geologic sequence, geometry, and a deformation mechanism, *Icarus,* 38**,** 456-472.

Yoshida, M., 2004. Possible effects of lateral viscosity variations induced by plate-tectonic mechanism on geoid inferred from numerical models of mantle convection, *Physics of the Earth and Planetary Interiors,* 147**,** 67-85.

Yoshida, M., Iwase, Y. & Honda, S., 1999. Generation of plumes under a localized high viscosity lid in 3-D spherical shell convection, *Geophysical Research Letters,* 26**,** 947-950.

Yoshida, M. & Kageyama, A., 2004. Application of the Yin-Yang grid to a thermal convection of a Boussinesq fluid with infinite Prandtl number in a three-dimensional spherical shell, *Geophysical Research Letters,* 31.

Yoshida, M. & Kageyama, A., 2006. Low-degree mantle convection with strongly temperature- and depth-dependent viscosity in a three-dimensional spherical shell, *Journal of Geophysical Research B: Solid Earth,* 111.

Yoshida, M. & Ogawa, M., 2004. The role of hot uprising plumes in the initiation of plate-like regime of three-dimensional mantle convection, *Geophysical Research Letters,* 31.

Zebib, A., 1993. Linear and weakly nonlinear variable viscosity convection in spherical shells, *Theoretical and Computational Fluid Dynamics,* 4**,** 241-253.

Zebib, A., Schubert, G., Dein, J.L., Paliwal, R.C. & Busse, F.H., 1983. Character and stability of axisymmetric thermal convection in spheres and spherical shells, *Geophysical & Astrophysical Fluid Dynamics,* 23**,** 1-42.

Zebib, A., Schubert, G. & Straus, J.M., 1980. INFINITE PRANDTL NUMBER THERMAL CONVECTION IN A SPHERICAL SHELL, *Journal of Fluid Mechanics,* 97**,** 257-277.

Zhang, S. & Yuen, D.A., 1996. Various influences on plumes and dynamics in time-dependent, compressible mantle convection in 3-D spherical shell, *Physics of the Earth and Planetary Interiors,* 94**,** 241-267.

Zhong, S., 2001. Role of ocean-continent contrast and continental keels on plate motion, net rotation of lithosphere, and the geoid, *Journal of Geophysical Research B: Solid Earth,* 106**,** 703-712.

Zhong, S. & Gurnis, M., 1995. Mantle convection with plates and mobile, faulted plate margins, *Science,* 267**,** 838-843.

Zhong, S., Parmentier, E.M. & Zuber, M.T., 2000a. A dynamic origin for the global asymmetry of lunar mare basalts, *Earth and Planetary Science Letters,* 177**,** 131-140.

Zhong, S., Zhang, N., Li, Z.X. & Roberts, J.H., 2007. Supercontinent cycles, true polar wander, and very long-wavelength mantle convection, *Earth and Planetary Science Letters,* 261**,** 551-564.

Zhong, S. & Zuber, M.T., 2001. Degree-1 mantle convection and the crustal dichotomy on Mars, *Earth and Planetary Science Letters,* 189**,** 75-84.

Zhong, S., Zuber, M.T., Moresi, L. & Gurnis, M., 2000b. Role of temperature-dependent viscosity and surface plates in spherical shell models of mantle convection, *Journal of Geophysical Research B: Solid Earth,* 105**,** 11063-11082.

Zhong, S.J., McNamara, A., Tan, E., Moresi, L. & Gurnis, M., 2008. A benchmark study on mantle convection in a 3-D spherical shell using CitcomS, *Geochemistry Geophysics Geosystems,* 9.

Zhu, T. & Feng, R., 2005. The patterns of high-degree thermal free convection and its features in a spherical shell, *Acta Seismologica Sinica,* 27**,** 11-24.

Acknowledgements

The thoughtful support, guidance, and encouragement of my late friend and colleague **Dr. Kai Stemmer** made this thesis possible. I am lucky to have met him.

Foremost, I would like to thank my supervisor, **Prof. Dr. Doris Breuer**, who encouraged me in every possible way and shared with me a lot of her expertise and research insight. I also like to express my gratitude to my colleagues of the **planetary physics group** at the DLR, whose thoughtful advice often served to give me a sense of direction during my PhD studies.

It is difficult to overstate my appreciation to **Prof. Dr. Tilman Spohn**, who supported and introduced me to the world of research and gave me the opportunity to work on this fascinating topic. I would also like to thank **Prof. Dr. Ulrich Hansen** for rewarding discussions about subtle qualities of fluid dynamics and kind support as a co-reviewer of this thesis.

I am tempted to individually thank all of my friends who, from my childhood until graduate school, have joined me in discovering what life is about and how to make the best of it. However, because the list might be too long and by fear of leaving someone out, I will simply say thank you very much to you all.

I cannot finish without saying how grateful I am with my family since all have given me a loving environment where to develop. Lastly, and most importantly, I wish to thank my parents, Gertraud and Dieter, who supported and encouraged me to do my best in all matters of life.